# ToF - The Time-of-Flight Device for H1

John Heatherington

Department of Physics
Queen Mary and Westfield College

*A thesis submitted in accordance with the regulations*
*for the Degree of Doctor of philosophy*
*in the University of London*
January 1995

**Abstract**

Event triggering for the H1 detector on the HERA electron-proton ring is dominated by background associated with the proton beam. A 99% reduction in trigger rate is achieved by time resolution of background from physics using ToF - a scintillator detector positioned in the incoming proton direction. Studies on the efficiency of the veto have been carried out to improve background rejection.

# Acknowledgements

I would like to thank the following people for their help and encouragement:

My family: Mum, dad, and my brother, Pete.

My girlfriend Gerry for all her support.

My fellow students at QMW, who helped with paw, TeX, physics, everything really ! Mike Akrawy, Gary Barker, Phil Biddulph (Brown Bottle), Andy Cooper, Adil Hasan, David Kant, James King, Thanos Mavroidis (idiot !), Paul Singh, Mosin Raza, (so-called) Eram Rizvi, Simon Robbins, and Andrew Yeaman.

The H1 physics staff at QMW: Graham Thompson, my supervisor, who put up with my inane ramblings for far too long! Eric Eisenhandler, Peter Kalmus, Murrough Landon and Wladimir von Schlippe, who all helped me in ways too numerous to mention.

The Technical staff at QMW: Derek Newman-Coburn and Terry Pritchard for all their help.

The QMW people at DESY: Gerry Lopez and Dave Robinson (BMW Dave).

The DESY Frank'n'Frei mob: Tan (the Man) Ahmed, Alistair Dann, Tanya Ebert, Alan Goodall, Chris Hilton, Roland Martin, Steve McMahon, Gareth Noyes and Valerie Jamieson( Noyes? Good Luck you two),Andrew Sirous, Paul Sutton, and Lindsay Wormesley.

The DESY 'useful people know': John Coughlan, Eckhard Elsen, Eric Evrard, Konrad Flamm, Scott Kolya, Christian Leverenz, Albert De Roeck, Peter Steffen, and Ueli Straumann. Also R. Maracek for use of his FToF data for comparison.

My friends in London (and also elsewhere): Chris Brushneen, Colm Durkin, Darren, Little Jon, POB, Spock, Mark (Riker), Vanessa Thubron, Gareth, Colin, Rik, Bryan.

My friends in Brum: Andy, Nick, Phil, Tester, Zomb.



*To my parents*

# Contents

# List of Figures

# List of Tables

# Chapter 1

# Physics at Hera

## 1.1 The Standard Model

The standard model describes the universe in terms of particles and their interaction via forces. There are four known forces: Electromagnetic, strong nuclear, weak nuclear and gravitation. The standard model is a combination of the standard electroweak model (describing electromagnetic and weak nuclear interactions) and QCD (describing strong nuclear interactions). The full standard model is exactly that - a model - and requires 19 independent parameters which must be found by experiment, but it does succeed in describing well the interactions of matter and anti-matter.

The standard model does not describe gravity, or the means by which mass is gained by particles. These are ongoing searches, but beyond the scope of this thesis.

Throughout this thesis, the following units and terms are used.

$\hbar$ (Planck's constant/2 $\pi$) = $c$ (the velocity of light) = 1.

Units of mass are thus given in GeV (actually GeV/$c^2$) unless otherwise stated in the text.

### 1.1.1 Particles and forces

Matter may be described as being composed of particles, which interact with one another via the exchange of energy (forces), the strength of which is determined by fields (e.g. electromagnetic) which are generated by the particles themselves. The exchange of energy between fundamental particles (spin-1/2 fermions) occurs via the exchange of intermediate vector bosons (with spin= 1). Each force has one or more of these gauge bosons which mediate and determine the range of the force (see

Table 1.1).

The fundamental fermions are split into two groups: leptons, which are affected by a mixture of electromagnetic and weak forces, and quarks which are primarily affected by the strong force, but which can also interact electromagnetically and weakly. Although only one generation of fermions is necessary for the particles making up the observable universe (such as protons and neutrons), each of the groups of fermions have three generations, each more massive than the last (See table 1.1) [1]. Each fermion has an anti-particle partner with identical mass but opposite quantum numbers.

Leptons form stable particles on their own and conserve lepton number within their generation. Quarks form stable states only in combination with other quarks (or anti-quarks), conserve only the total baryon number (1/3 per quark of whatever flavour) and their flavour can be changed via the weak interaction.

| Particle (Lepton) | Charge | Generation | Lepton number | Mass |
|---|---|---|---|---|
| Electron $e$ | -1 | 1 | $L_e = 1$ | 0.511 MeV |
| Muon $\mu$ | -1 | 2 | $L_\mu = 1$ | 105.6 MeV |
| Tau $\tau$ | -1 | 3 | $L_\tau = 1$ | 1784 MeV |
| $e$ neutrino $\nu_e$ | 0 | 1 | $L_e = 1$ | 0 ($<\sim 17eV$) |
| $\mu$ neutrino $\nu_\mu$ | 0 | 2 | $L_\mu = 1$ | 0 ($<\sim .27MeV$) |
| $\tau$ neutrino $\nu_\tau$ | 0 | 3 | $L_\tau = 1$ | 0 ($<\sim 35MeV$) |
| Particle (quark) | Charge | Generation | Baryon number | Mass |
| Up $u$ | $+2/3$ | 1 | 1/3 | 2-8 MeV |
| Down $d$ | $-1/3$ | 1 | 1/3 | 5-15 MeV |
| Charm $c$ | $+2/3$ | 2 | 1/3 | 1.3-1.7 GeV |
| Strange $s$ | $-1/3$ | 2 | 1/3 | 100-300 MeV |
| Top $t$ | $+2/3$ | 3 | 1/3 | $\sim$ 170 GeV* |
| Bottom $b$ | $-1/3$ | 3 | 1/3 | 4.7-5.3 GeV |
| Gauge Boson | Charge | | Mediates | Mass |
| Photon | 0 | | Electromagnetic | 0 |
| $Z_0$ | 0 | | Weak | 91.2 GeV |
| Gluon | 0 | | Strong | 0 |
| $W^+/W^-$ | $+1/-1$ | | Weak | 80.2 GeV |

Table 1.1: *Properties of fundamental particles*

* A claim to have found the top quark has been published [2].

Particles interact via propagators which transfer 4-momentum (and colour charge in the case of the strong interaction) between the interacting particles. These propagators are themselves virtual particles which can be said to exist for a short time, given by the Heisenberg uncertainty principle, which is inversely proportional to their mass (and therefore energy via $E^2=m^2+p^2$ ):

$$\Delta E \times \Delta t \approx 1 \tag{1.1}$$

Each force has its own propagator(s) and coupling constant, with the electromagnetic and weak interactions connected via the mixing of the photon and $Z^0$ propagators. The massive mediator of the weak force can exist for only a short time ($\sim 10^{-23}$ s) and therefore cannot travel far, thus the interaction appears weak although the coupling constant has the same value as that for the electromagnetic interaction. The massless gluons are themselves subject to the strong (colour) force. This force increases with increasing distance until the energy is sufficient to create a $q\overline{q}$ pair. The force therefore has a short range despite the massless propagator.

### 1.1.2 QED Quantum Electro-Dynamics

Calculations of electroweak interactions can be made by treating interactions as a small perturbation in the free-particle potential. As long as the coupling constant, $\alpha$, is much smaller than one, these calculations are feasible. For electromagnetic and weak interactions, $\alpha$ is small and the perturbative method forms the basis of QED. Calculations of the strong force (QCD calculations) are more problematic as $\alpha_s$ increases with decreasing interaction energy. Around 1 GeV, $\alpha_s$ is too large for perturbative methods to calculate cross-sections.

For QED the coupling constant is related to the charge by:

$$\alpha = \frac{e^2}{4\pi\epsilon_0} \approx \frac{1}{137} \tag{1.2}$$

The matrix elements which make up calculations have been codified into Feynman diagrams (such as Figure 1.1), and calculations of transition amplitudes and cross-sections can be made by adding the contributions from all such diagrams together and squaring the result. However, in principle, an infinite number of diagrams are available for each process, as particles may radiate energy before or after the main interaction (radiative effects) and diagrams involving the emission and subsequent recombination of particles (loops) may have infinite energy terms. These infinite terms are present in the perturbative expansion and no calculation is possible.

A method of removing these problems, called renormalisation, relies on the fact that the charge in equation 1.1.2 is not the same as the charge measured in the laboratory. The 'bare' charge used in the calculation depends on the energy scale of the interaction. Infinities in the amplitude calculation are removed by reparameterising the bare charge in terms of the charge at a particular energy transfer, suitable to the process studied.

The infinite energy terms in various diagrams cancel each other out leaving a finite value which must be recalculated for each energy transfer. The coupling constants are then different for each energy transfer studied. This is the origin of the 'running coupling constant' of QED.

For all practical energies the QED coupling constant remains approximately the same ($\alpha = 1/137$). The QCD coupling constant ($\alpha_s$) covers a much larger range (See section 1.1.5).

Figure 1.1 shows the first order diagram for electron-muon scattering.

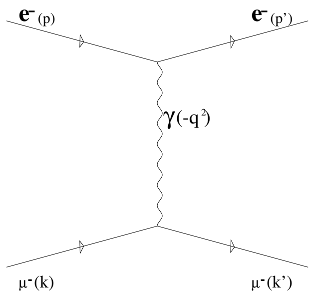


Figure 1.1: *Feynman diagram for electron-muon scattering.*



The kinematical variables used to describe such interactions are

$p$ incoming electron momentum

$p'$ outgoing electron momentum

$k$ incoming muon (proton) momentum

$k'$ outgoing muon (proton) momentum

$q^2 = (p-p')^2 = -Q^2$ square of four momentum transfer

$Q^2_{max} = s$ Maximum momentum transfer

$\nu = q.k/m_p$ energy of current $J$ in p rest system

$\nu_{max} = s/(2m_p)$ maximum energy transfer

$y = (q.k)/(p.k) = \nu/\nu_{max}$ fraction of maximum possible energy transfer

$x = Q^2/(2q.k) = Q^2/(2m_p\nu) = Q^2/(ys)$ Bjorken scaling variable

### 1.1.3 Electroweak model

Electromagnetic and weak interactions can be described using a single interaction which is described by quantum electrodynamics (QED). Cross-sections for interactions can be calculated using QED and perturbation theory, because the coupling strength of the interaction ($\alpha_{em}$ is <<1).

Calculations are made by considering the motion of one particle in the potential created by the other particle, using a small perturbation in the potential. The amplitude (and hence cross-section) of any scattering can be calculated by finding the transition current $J_\mu$ of each particle (See Equation 1.1.3) with the momentum difference of the incoming and outgoing wavefunctions equal to the momentum transfer of the scatter.

$$J_\mu^{fi} = -e\overline{u}_f\gamma_\mu u_i e^{i(p_f-p_i).x} \tag{1.3}$$

$u$ is the electron wavefunction $\Psi = u(\mathbf{p})e^{-ip.x}$.

$\gamma_\mu$ is the four×four (dirac) spin matrix coupling the initial and final states.

The form of the electron-muon scattering cross-section is :

$$\frac{d\sigma}{d\Omega} = \frac{\alpha^2}{4E^2\sin^4\frac{\theta}{2}}\frac{E'}{E}\left[\cos^2\frac{\theta}{2} - \frac{q^2}{2M^2}\sin^2\frac{\theta}{2}\right] \tag{1.4}$$

$\alpha$ is the (electromagnetic) coupling constant.

$E$ is the energy of the incoming electron.

$E'$ is the energy of the scattered electron.

$\theta$ is the scattering angle of the electron in the rest frame of the muon.

$M$ is the mass of the target (muon in this case).

This cross-section formula holds for the scattering of any pair of spin-half particles which scatter elastically and where one is much more massive than the other.

### 1.1.4 The quark model

The proton and neutron are not fundamental particles. They are composed of smaller constituents called quarks. All hadrons are formed of quarks which are in turn held together by gluons in $q\overline{q}$ (meson) and $qqq$ (baryonic) (relatively) long-lived states ($10^{-12}$ s to $10^{30+}$ yrs).

The actual composition of hadrons is complex, but can be thought of as having three components:

- The valence quarks .These are the $q\overline{q}$ or $qqq$ which define the quantum numbers of the hadron.
- Sea quarks. These are $q\overline{q}$ pairs being created for the short time allowed by Equation 1.1.1 and then annihilated, with the possibility of many such pairs being in existence at the moment of interaction. These hold a fraction of the hadron's momentum and interact just as the valence quarks can.
- Gluons. These mediate the strong interactions holding the nucleus together. They also hold a fraction of the hadron's momentum.

The sum of these three components hold the total energy and momentum of the proton. The variable $x$ is often used to denote the fraction of a proton's momentum that the struck parton has.

The variable $x$ is actually the Bjorken scaling variable, defined by:

$$x = Q^2/(2q.p) = Q^2/(2m_p\nu) \tag{1.5}$$



### 1.1.5 QCD

The strong interaction binds the quarks in the nucleus together, and requires an extra quantum number (colour, which can take one of three values, each with its anti-colour) to allow for such states as the spin-symmetric wavefunction of identical quarks (uuu, $J_3$ =3/2), which exist in nature. Quantum Chromodynamics (QCD) describes the interactions of quarks and gluons, the mediator of the strong interaction. Gluons themselves undergo the strong interaction and therefore couple directly to other gluons (in QED, photons are uncharged and do not couple electromagnetically to other photons, in first order).

It is thought that quarks obey SU(3) colour symmetry and that the (relatively) stable hadrons are composite colourless states; mesons form the $3 \otimes \overline{3}$ colourless states, baryons are $3 \otimes 3 \otimes 3$ colourless states.

Gluons belong to an SU(3) octet, with each of the eight types of gluon carrying one colour and one anti colour. A ninth SU(3) singlet state gluon is suggested by the theory, but this would be a colourless entity and does not mediate the strong interaction.

Hadrons are colourless entities. Unlike QED, QCD interactions exhibit 'asymptotic freedom'. The strength of interaction tends to zero as the separation tends to zero and this is exacerbated by the self-coupling of gluons, as each coloured particle is surrounded by gluons of its own colour, leading to an increased interaction strength at longer distances.

The strength of the interaction at long range leads to another result known as 'infra-red slavery', where the coupling strength at low-$Q^2$ ($<\sim$ 1 GeV) becomes too large for perturbative expansions of the scattering amplitude to be calculable. The running coupling constant covers a range from $\sim$ 0.1 at high ($>$ (100 GeV)$^2$) $Q^2$ to $\sim$1 at (1 GeV)$^2$).

The cross-section for those events which *are* calculable has a similar form to the QED cross-section. As the proton is not a point-like particle, but a diffuse object made up of smaller constituents, the muon current is replaced by the general function [3]:

$$J_\alpha = e\overline{u}(p')\left[f_1(q^2)\gamma^\mu + \frac{\kappa}{2M}f_2(q^2)i\sigma^{\mu\nu}q_\nu + f_3(Q^2)q_\alpha\right]u(p) \tag{1.6}$$

where $\kappa$ is the anomalous magnetic moment, $\gamma^\mu$ is the dirac spinor associated with the muon, $\sigma^{\mu\nu}$ is a second rank tensor associated with the proton.

The (elastic) form factors ($f_1, f_2$ and $f_3$) describe the pointlike charge, magnetic moment and parity violating terms in the interaction. The parity violating term is non-vanishing only in weak neutral current interactions near the $Z^0$ mass and so not included in the electromagnetic scattering under discussion.

These factors can be expressed in the more experimentally accessible electric and magnetic form factors [3]:

$$G_E(Q^2) = f_1(Q^2) + \frac{\kappa q^2}{4M^2} f_2(Q^2) \tag{1.7}$$

$$G_M(Q^2) = f_1(Q^2)\kappa f_2(Q^2) \tag{1.8}$$

giving a cross section:

$$\frac{d\sigma}{d\Omega} = \frac{\alpha^2}{4E^2 \sin^4\frac{\theta}{2}} \frac{E'}{E}\left[\frac{G_E^2 + \tau G_M^2}{1+\tau}\cos^2\frac{\theta}{2} - 2\tau G_M^2 \sin^2\frac{\theta}{2}\right] \tag{1.9}$$

Here $\tau = \mathrm{Q}^2/4\mathrm{M}^2$.

For inelastic scattering, the form factors become functions of $\nu$ as $x$ can vary ($Q^2$ is no longer equal to $2M\nu$). The cross-section becomes [3]:

$$\frac{d\sigma}{d\Omega} = \frac{\alpha^2}{4E^2 \sin^4\frac{\theta}{2}} \frac{E'}{E}\left[W_2(\nu, Q^2)\cos^2\frac{\theta}{2} + 2W_1(\nu, Q^2)\sin^2\frac{\theta}{2}\right] \tag{1.10}$$

### structure functions

At low $Q^2$ ($<\sim$ 5 GeV$^2$), the probe does not 'see' the fine detail of the proton, but merely acts as if the proton were a diffuse mass. Higher energy probes can interact with individual partons, as if the parton was a free point particle unaffected by the other constituents of the proton (see Section 1.2.1).

The partons are the quarks and gluons of QCD and the distribution of the momenta of quarks and gluons within the proton affects the scattering amplitude of ep interactions.

The structure functions $W_1$ and $W_2$ can be written as:



$$W_2 = \delta\left(\nu - \frac{Q^2}{2m}\right) \tag{1.11}$$

$$W_1 = \frac{1}{2}\frac{Q^2}{2m^2} W_2 \tag{1.12}$$

where $m$ is the mass of the parton undergoing scatter. For a quark with momentum fraction $x = Q^2/2M\nu$ (m=$x$M ie the fraction of the proton mass which the parton has) the structure functions become [3]:

$$F_1(x) = MW_1(\nu, Q^2) \tag{1.13}$$

$$F_2(x) = \nu W_2(\nu, Q^2) \tag{1.14}$$

For the spin 1/2 quarks, $F_2 = 2xF_1$ [4].

### Scaling and scaling violations

The structure functions for point-like constituents of the proton should scale with $x$. The presence of gluonic interactions means that the parton densities (and therefore the structure functions via equation1.1.5) also evolve in $Q^2$.

The parton densities $u_i$ define the probability of finding a parton with momentum fraction $x$ at a particular $Q^2$ and is related to the structure function $F_2$ by:

$$F_2 = \sum_{i=1}^{n} e_i^2 u_i(x, Q^2) \tag{1.15}$$

The summation is over all quark *flavours* and $e_i$ is the charge of the flavour in question.

The gluons do not enter into this structure function as they are uncharged, and do not interact with the incoming photon. Experimental results have determined that the quarks hold $\sim$ 54% of the proton's momentum.

The evolution in $Q^2$ occurs because a high energy virtual photon may interact with a quark of momentum $x$, which originally came from a parent quark (momentum $y$) which radiated a gluon (See figure 1.2). By calculating the probability of a quark with momentum $y$ giving off a gluon to become a quark with momentum

$x$, and integrating over all momenta such that $y > x$, the evolution in $Q^2$ of the structure functions can be calculated.

Such a calculation is made from a given a fixed reference scale ($Q_0^2$) for any $Q^2 > Q_0^2$ using the DGLAP (also known as the Altarelli-Parisi evolution equation[5]) equation. An alternative approach, using the BKFL equation [6], covers low $x$ behaviour where the Altarelli-Parisi equation fails, and uses a perturbative expansion in terms of $\ln(1/x)$.

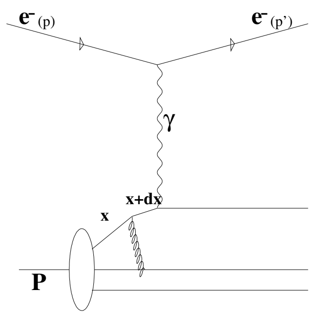


Figure 1.2: *Interaction of a photon and a quark. The quark may radiate a gluon and have a different momentum fraction.*



## 1.2 Physics processes studied at HERA

Figure 1.3 shows a typical process, electron-quark scattering. The kinematics of the process are described by the momenta of the various particles. The incoming (outgoing) electron has momentum $p$ ($p'$). The struck quark has initial momentum $k$, a fraction $x$ of the proton's momentum, and final momentum $k'$. The following terms are used to describe the interaction, neglecting the electron mass.

p = (0,0,-$E_e$, $E_e$) four momentum of incoming electron

k = (0,0,$E_p$, $E_p$) four momentum of incoming parton

p$'$ = ($E_e'\sin\theta_e'$,0,$E_e'\cos\theta_e'$, $E_e'$) four momentum of scattered electron

q$^2$ = (p-p$'$)$^2$ = -2$E_e E_e'$(1-cos$\theta_e'$)= -$Q^2$ square of four momentum transfer

s = (p+k)$^2$ = $4E_eE_p$ square of total e.m. energy

$W^2 = (p+q)^2 = m_p^2 - Q^2 + 2m_p\nu = m_p^2 + Q^2(1/x - 1)$ Mass squared of total hadronic system produced

$\Delta = \hbar/Q$ Smallest object size that can be resolved in the proton

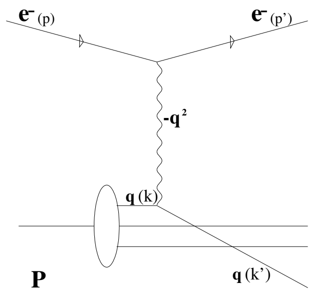


Figure 1.3: *Feynman diagram for electron-quark scattering.*

The two major processes studied are deep inelastic scattering (DIS) and photoproduction (also referred to as $\gamma$p). The definitions overlap somewhat (as described below).

### 1.2.1 Deep Inelastic Scattering

In Deep inelastic scattering interactions, the electron couples electroweakly to a parton within the proton. For interactions with a $Q^2 \gg 1$ GeV$^2$ (the proton mass) the electron-proton cross-section can be calculated as if the proton were made up of smaller point-like partons, with only the struck parton interacting. The rest of the proton takes no part in the interaction. The cross section depends on the distribution of momenta and energy of the struck quark, given by the structure functions described in section 1.1.5

The neutral current (NC) and charged current (CC) events (See Figure 1.4) can be separated using the final state lepton (electron and neutrino respectively).

For the lowest order processes, the Bjorken scaling variable $x$ gives the fraction of the proton's momentum carried by the parton. However, when higher order diagrams are included, this relationship is not exact and the incoming parton has a momentum fraction $> x$.

The cross-sections for neutral and charged-current electron-proton scattering are [7]:

neutral current

$$\frac{\mathrm{d}^2\sigma}{\mathrm{d}x\mathrm{d}Q^2} = \frac{4\pi\alpha^2}{sx^2y^2}\left[(1-y)F_2^{nc} - (y^2x)F_1^{nc} \pm \left(y - \frac{y^2}{2}\right)xF_3^{nc}\right] \tag{1.16}$$

charged current

$$\frac{\mathrm{d}^2\sigma}{\mathrm{d}x\mathrm{d}Q^2} = \frac{G_f^2 M_W^4}{\pi x\left(M_W^2+Q^2\right)^2}\left[y^2xF_1^{cc} + (1-y)F_2^{cc} \pm \left(y - \frac{y^2}{2}\right)xF_3^{cc}\right] \tag{1.17}$$

The functions $F_n$ are functions of $x$ and $Q^2$ and different for charged and neutral current interactions.



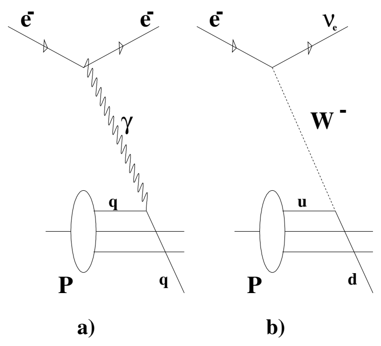


Figure 1.4: *DIS interactions. a) Neutral current b) Charged current.*

### 1.2.2 Photoproduction

Photoproduction is the interaction of an almost-real virtual photon, emitted by an electron, with a proton. At HERA it forms part of neutral current scattering, ep $\rightarrow$ eX, but with $Q^2 \approx 0$. Many of the photoproduction processes have their DIS counterparts, with similar Feynman diagrams. Those with a low-$Q^2$ are considered photoproduction, those with a high $Q^2$ are considered DIS.

As the photon may couple to quarks, the photon may interact with the proton directly or as a hadron itself. Direct processes are those in which the photon couples directly to a parton. These include photon-gluon fusion and QCD compton scattering as well as the quark parton model (QPM) simple single (1+1 - 1 current jet + 1 remnant jet) jet interaction where the photon strikes a quark in the proton and knocks it out forming a jet.

The hadronic interaction may be divided into three general groupings:

- VDM model process. The quantum number equivalence of the photon and the $\rho, \omega, \phi$... neutral mesons allow the photon to interact as a vector meson. This encompasses both soft and hard processes (see Figure 1.5).

- Direct processes. The photon couples directly to a quark or gluon from the proton. These hard processes include photon-gluon fusion and compton scattering of the photon off a quark (Figure 1.6). Some of these processes are thought of as also being DIS.

- Resolved process. The photon emits a quark which then interacts with quarks or gluons from the proton, leaving a remnant jet in the direction of the incident photon (Figure 1.7). These hard processes include some which can also be considered as hard VDM-type interactions and could also be described as being DIS interactions.

The characteristics of high energy photons means that a photon structure function, $F^{\gamma}$, is necessary to describe the parton structure of the photon. $F^{\gamma}$ is also necessary in DIS interactions where the photon substructure can be measured.

The hard processes (both direct and resolved) are characterised by quark or gluon jets with high $P^t$.

### 1.2.3 Exotic interactions

Exotic particles are those which are not required in the standard model, and may indeed not fit with the model at all. Such particles include Leptoquarks, excited leptons and leptogluons. Leptoquarks, made up of a quark and lepton in a bound state, are one such type of exotic particle. These particles, if they exist, should be produced in $s$-channel e-q fusion at HERA unlike the pair production required for such particles at other ($\overline{p}p$ or $e^+e^-$) experiments.

HERA, with its new kinematical range, allows searches for such particles or allows improved (lower) limits on their masses to be calculated.

These limits are currently [8] $\sim>$150 GeV for $F = 2$ (Fermion number = 2 i.e. particle-particle) $\sim>$100 GeV for $F = 0$ (particle-antiparticle).



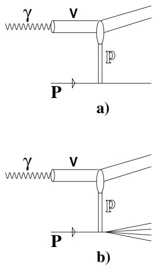


Figure 1.5: *Photoproduction interactions : VDM a) diffractive scattering b) non diffractive scattering.*

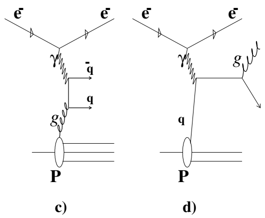


Figure 1.6: *Photoproduction interactions : Direct c) Boson gluon fusion d) QCD Compton scattering.*

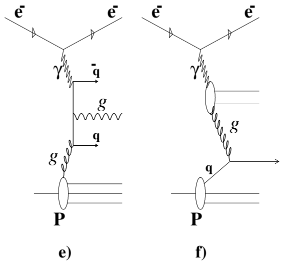


Figure 1.7: *Photoproduction interactions : Resolved e) Boson gluon fusion with gluonic jet d) Hard scatter with VDM characteristics.*

## 1.3 ep Physics before HERA

The fixed target experiments available before HERA (SLAC,BCDMS,E665 and NMC) each covered a certain kinematical region (See Figure 1.8). HERA allows a new kinematical region to be explored–low $x$ and low $Q^2$.

The pre-HERA kinematical region does not overlap with the HERA region in which physics data is studied, although similar regions of $Q^2$ can be studied at different W$^2$. The pre-HERA region can in principle be reached by HERA events, using very inelastic low-energy scattered electrons. Such events would be contaminated with mis-identified hadrons, however, making this study impractical. If the beam energies were lowered, an overlap with the pre-HERA region becomes practical.

Alternatively, by moving the interaction point to a more positive $z$ (ie in the forward direction), the electron angle cut (required to ensure the electron passed through sufficient calorimeter material) could be moved to a higher angle, and lower $x$ regions could be explored.



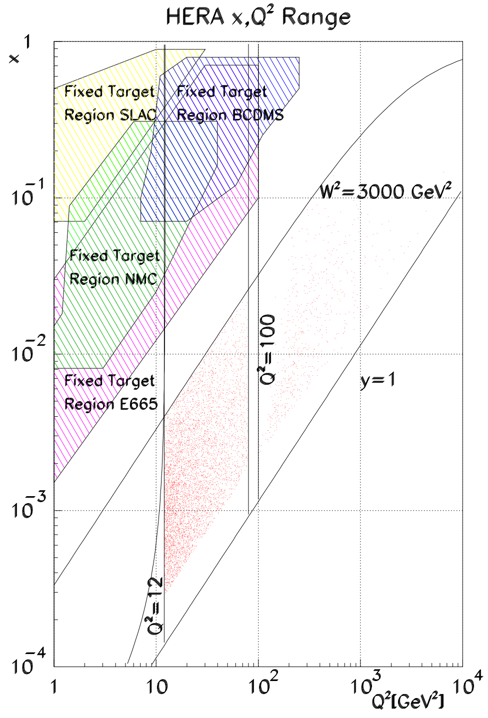


Figure 1.8: *Kinematical region accessible by HERA compared to previous experiments. The data points are selected low and high $Q^2$ physics events.*

## 1.4 Physics at HERA

### 1.4.1 The new kinematical region

Figure 1.9 shows the distribution of H1 data in the $x, Q^2$ region. Also shown are important kinematical features (lines of constant scattered electron angle for instance).

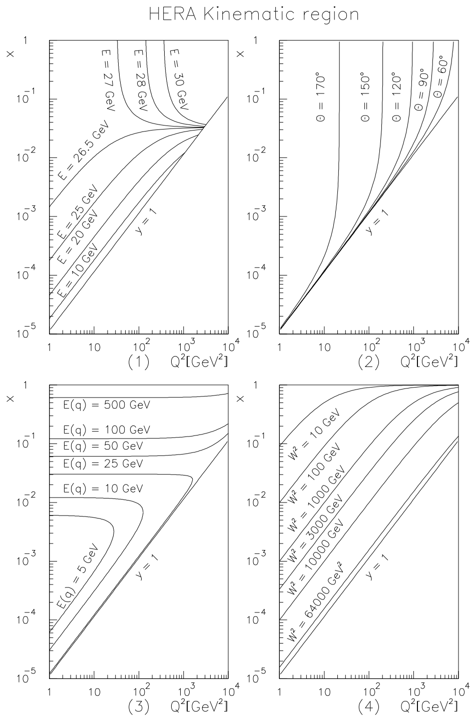


Figure 1.9: *Kinematical $Q^2$, $x$ region at HERA. The four plots represent lines of constant: (1) Scattered electron energy. (2) Scattered electron angle. (3) Struck quark energy. (4) Square of total hadronic system energy.*



Table 1.2 shows the comparison between the kinematical region accessible to previous experiments and that found at HERA.

| Kinematic variable | Pre HERA value | HERA value |
|---|---|---|
| s (GeV$^2$) | $10^3$ | $10^5$ |
| maximum practicable $Q^2$ | 400 | 40000 |
| $\Delta$ (cm$^{-1}$) | $1 \times 10^{-15}$ | $1 \times 10^{-16}$ |
| $\nu_{max}$ (GeV) | 500 | 52000 |
| Minimum $x$ at $Q^2 = 10$ GeV$^2$ | $1{\times}10^{-2}$ | $1{\times}10^{-4}$ |

Table 1.2: *Comparison of Kinematic regions accessible to HERA and previous experiments*

### 1.4.2 Structure functions

At HERA, a new low $x$ region for electron-proton physics is accessible. This is interesting as the $x$ evolution of $F_2(x, Q^2)$ at fixed $Q^2$ gives information on the internal structure of the proton, allowing the current theory to be tested.

For kinematical regions in which $\alpha_s$ is small (eg $Q^2 > 10$ GeV$^2$), as $x \to 0$ the numbers of gluons and sea quarks will dominate and increase as [9]:

$$x^{1+\lambda}, \lambda \approx \alpha_s[12ln(2)]/\pi \approx 1/2 \tag{1.18}$$

As $x$ becomes very small, the number of partons, each with a fixed size ($\sim 1/Q$) becomes large enough that the partons overlap, leading to a saturation of the structure function. The critical $x$ ($x_{crit}$) at which saturation is reached ($10^{-5}$ for 10 Gev$^2$) are unobtainable at HERA energies [10].

However, the possible existence of 'hot spots', where low-$x$ partons cluster around the valence quarks, give a higher $x_{crit}$($10^{-3}$ at 10 GeV$^2$) which is just obtainable at HERA energies.

Figure 1.10 shows the F$_2$ structure function as measured at H1 [11]. The data shows that there is an increase in probability of finding low $x$ partons within the proton at each Q$^2$. F$_2$ is studied as for F$_1$ can be described in terms of F$_2$ (See Equation 1.13).

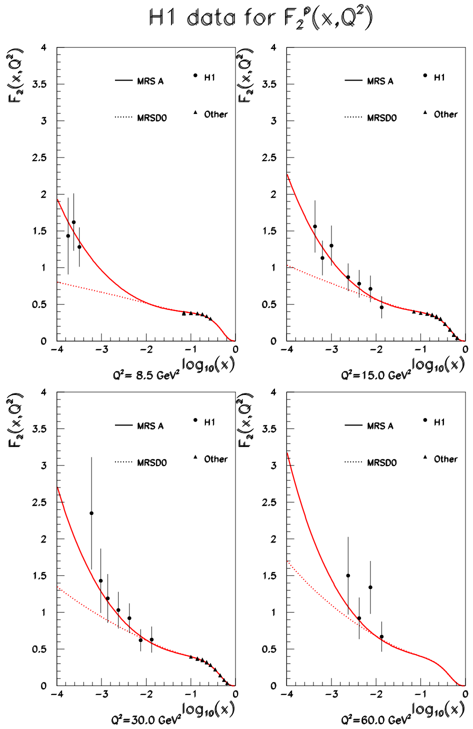


Figure 1.10: *H1 data for structure function $F_2$, at four different $Q^2$ values. Curves are fits to the data using current theoretical models.*



**Kinematical peak**

The cross section for electron-hadron interactions includes a $1/Q^4$ term which causes low-$Q^2$ interactions to be favoured over those with higher $Q^2$.

Given:

$$Q_e^2 = xy_e s \tag{1.19}$$

and

$$y_e = 1 - \frac{E_{e'}}{E_e}(1 - cos^2\frac{\theta}{2}) \tag{1.20}$$

This means that for a given $x$, for the 4-momentum transfer to be low $E_{e'}/E_e$ must be as close to one as possible and the energy of the scattered electron is therefore close to the beam energy. Figure 1.9 (upper left) shows the region of phase space available. The vast majority lies between $25 < E_e' < 28$ GeV.

This creates a peak in the scattered electron energy centred on the the beam energy.

### 1.4.3 Photoproduction

The total photoproduction cross-section for H1 (21 nb$^{-1}$) for 1993 was [12]:

$$\sigma(\gamma\ p) = 156 \pm 2(\text{stat}) \pm 18(\text{syst})\mu b \tag{1.21}$$

The centre of mass energy ($W$) for this cross-section is ~200 GeV, and comparison with other data [13] suggests a Regge-like interaction. Fits to previous data using combinations of partial cross-sections from soft and hard processes are generally poor, and depend critically on the photon structure function and the limit of integration for hard processes.

An interesting set of events known as rapidity-gap (Rap-Gap) events have also been observed. These events have less hadronic activity in the forward direction near the beam pipe than would be expected from colour induced fragmentation of proton remnants. The energy at large pseudorapidity, $\eta = \ln\,\tan(\theta/2)$, of the hadronic tracks nearest the beampipe is lower than expected.

Rap-Gap events are presumed to occur from exchange of colourless objects (like a gluon-gluon particle or a pion).

### 1.4.4 Typical events

Figures 1.11 and 1.12 show typical background and physics candidate events in H1. Figure 1.11 shows a background event, with a great deal of activity in the tracker, but the tracks point to a vertex somewhere inside BEMC.

Figure 1.12 shows a typical DIS candidate event, with tracks pointing to a definite vertex in the centre of the tracking chambers.

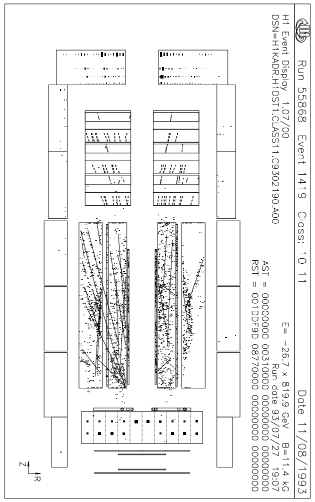


Figure 1.11: *A typical background event at H1.*



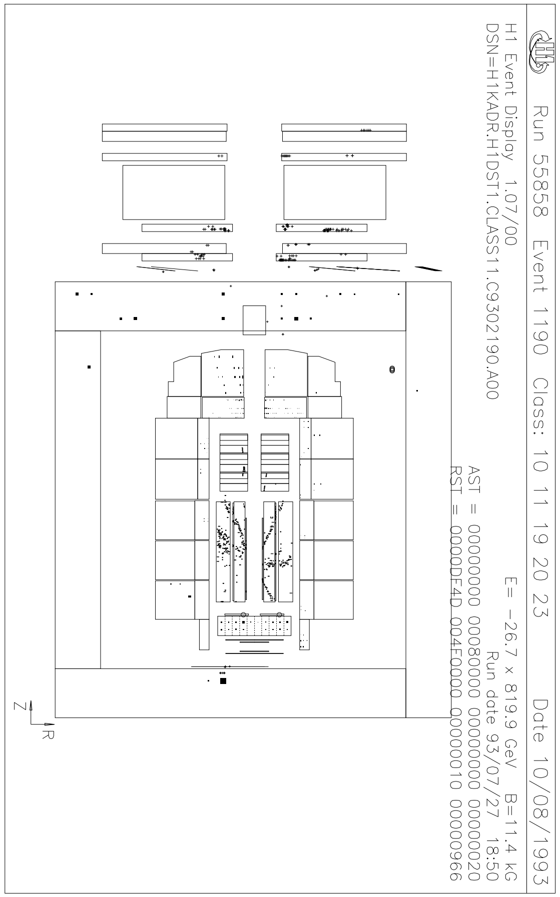


Figure 1.12: *A typical physics candidate event in H1.*

# Chapter 2

# The H1 detector

## 2.1 Introduction

Particle physics uses many acronyms and terms with specific meanings. Within this thesis, where necessary, each such term is explained when first encountered in the text. A glossary has also been provided for ease of understanding in Appendix A.1.

## 2.2 The Hera ring

During the 1992 and 1993 runs there were two detectors working on the Hera electron-proton ring at DESY, Hamburg. H1 is covered in this thesis, the other detector was Zeus. The Hera ring (See Figure 2.1) is 6.4 km in circumference and accelerates protons anticlockwise at a design energy of 820 GeV and electrons clockwise at a design energy of 30 GeV. Design luminosity is $1.5 \times 10^{31}$ cm$^{-2}$s$^{-1}$. During the first two years of running, the energies achieved have been 820GeV and 26.7 GeV for protons and electrons respectively. Only $\sim$1% of design luminosity was achieved in these first two years of running amounting to a total of just less than 1 pb$^{-1}$.

The particles are kept in separate beamlines, using superconducting magnets for the proton ring and 'warm' magnets for the electron ring. The beams are brought together at two sites on the ring, North hall for H1 and South hall for Zeus. Within each beam the particles are grouped in bunches, with the centre of each bunch separated by 96 ns from the next bunch. The ring is designed to hold a maximum of 220 bunches during nominal operation, during 1992 running 10 bunches in each beam were filled. During 1993 there were 60 filled bunches in each beam.

Most (90%) bunches are filled such that a full proton bunch and a full electron bunch pass through the interaction point simultaneously, with the remaining 10%



(6 of the 60 filled bunches in 1993) of the bunches arranged so that only one of the beams has a filled bunch in the detector. These are called pilot bunches and are used for calibration and background monitoring purposes.

The electrons are provided by a series of available preaccelerators. Electrons are accumulated from a linear accelerator (linac) and stored at 500 MeV in a small storage ring until 60 mA have been accumulated. These are injected into DESY II and accelerated to 7 GeV.

New preaccelerators were required to accelerate the protons. A 50 MeV linac delivers a 6 mA beam of negatively charged hydrogen ions. These ions are stripped of their electrons on injection to DESY III where they are collected into 11 rf 'buckets' and accelerated to 7.5 GeV.

The electrons and protons are then transferred to PETRA II where they accumulate into a maximum of 70 bunches (in each beam) and the protons are accelerated to 40 GeV. The particles are then transferred to their respective beamlines in Hera for final acceleration.

This process is repeated three times to provide 210 bunches.

Figure 2.1: *Plan view of the Hera ring*

## 2.3 Physics at the H1 detector

The H1 detector is designed to detect and differentiate between the particles produced in the collision between a proton (at 820 GeV) and an electron (at 30 GeV). The collision remnants which are sufficiently long-lived to be detectable are photons, hadrons, mainly pions, and leptons. H1 is designed to differentiate between the various types of particles by storing information about their mass, charge, momenta, energy and penetrative capability for later analysis and reconstruction.

Particles are detected by their interaction with material in subdetectors. The momenta of charged particles are measurable by the path (bent by the magnetic field) of ionization they produce in material they pass through. The drift chamber trackers measure these paths. The energy of charged and neutral hadronic particles can be measured by the charged remnants of strong interactions which the particles undergo as they pass through the material of the calorimeter.

Leptons and photons interact electromagnetically forming showers of particles. Electrons lose energy via bremsstrahlung (which is very sensitive to particle mass) giving off photons. These high energy photons pair produce electron-positron pairs which lose energy via further bremsstrahlung. Electrons have low mass and interact rapidly (i.e. within a short distance) in this way. A separation from charged hadronic particles is therefore possible as electrons do not penetrate the calorimeter as far. Muons, with higher mass, penetrate through the calorimeter, losing energy mostly by ionization.

High energy photons pair produce charged particles (as above). Lower energy photons excite atoms of the media they pass through.

The subdetectors are designed to localize and/or measure the charge produced from the pair production or the light from the low energy photons. This data is then digitized for later reconstruction.

The data from the subdetectors is reconstructed giving the position, charge, energy and momenta of the particles. From this data, the physics processes of the interactions in each event can be studied.

The majority of physics occurring in the H1 detector is from neutral current interactions, with a low $Q^2$ photon exchanged. In such events, the virtual photon penetrates the proton to interact with a quark. This splits the proton producing hadronic jets, and the momentum transferred via the photon causes the electron to



scatter. H1 is designed to differentiate electrons from hadrons with a high efficiency.

Charged current interaction also occur, producing neutrinos which, to first order, do not interact with the material of the detector and so some collision energy is lost. It is important for the H1 detector to be hermetic to other particles for an accurate measurement of this missing energy to be made.

Muons are useful in identifying heavy flavour events, and are also a pointer to some exotic interactions, where lepton number is not conserved, so H1 must have a good capacity for finding muons.

## 2.4 Overview of H1 Apparatus

See Figures 2.2 and 2.3

The H1 detector is asymmetric because of the asymmetry of the beam energies, with the greater part of the calorimetric mass in the forward (outgoing proton) direction. This allows the high energy of the forward going hadronic proton fragments to be contained and their energy measured.

The difference in beam energies is a result of synchrotron losses affecting the less massive electron by several orders of magnitude more than it affects the proton. The equation describing synchrotron energy loss per revolution ($dE$) is [1]:

$$dE = \frac{4\pi e^2 v^3 E^4}{3Rc^{11}m^4} \tag{2.1}$$

$E$ is the beam energy.

$R$ is the orbit radius.

$m$ is the mass of the particle.

$v$ is the velocity of the particle.

The $1/m^4$ factor is the decisive one, the electron has a rest mass of 0.511 Mev/$c^2$ as opposed to the proton mass of 938 Mev/$c^2$.

Figure 2.2: *Cut-away view of H1 showing the main subdetectors*



The H1 detector is made up of several subdetectors, each designed for a specific task. Here an overview is given, describing the function of the subdetectors. Further details are given in individual subdetector sections.

The subdetectors are divided into three general groupings, trackers (which collect directional information), calorimeters (which collect information on energy) and others (which aid the other two in their jobs or detect specific types of particles) such as the muon system.

The trackers are essentially gas filled chambers with wires (kept at a high voltage) running through them. Charged particles passing through ionize the gas. The charge is then attracted to the wires which are attached to readout devices and measure the location of the charge collected, principally by timing. Paths of the particles causing the ionization can then be reconstructed from each wire which collected charge. The momentum of the particles can then be calculated from the curved path.

The trackers in H1 consist of central chambers with wires strung along the beam axis and forward/backward chambers with wires strung perpendicular to the beam axis. Drift chambers provide accurate measurements of location and proportional chambers give a rapid response for triggering purposes.

The calorimeters are the main liquid argon (LAr) calorimeter, the backwards electromagnetic calorimeter (BEMC), the tail catcher and the plug. The LAr calorimeter covers the central and forwards area and the BEMC covers the backward area. The tail catcher measures hadronic and muonic energy escaping from the LAr. The plug measures hadronic energy in the forward direction near the beampipe.

Calorimeters work on the basic principle of absorbing a particle's energy by interactions and sampling the number of particles produced, with the energy measurement based on the number of such particles. The BEMC does this by detecting the number of photons produced via scintillation. The LAr does this by measuring the ionization they produce. In order to provide material in which the particles can interact, the sensitive material is interleaved with absorbing material (such as lead or steel) in which the interactions can occur.

A superconducting solenoid provides a homogenous magnetic field. The iron return yoke includes streamer tubes which are part of the muon system. Forward and backward endcaps include more streamer tubes, and the forward muon system, located outside the forward endcap and including a toroidal bending magnet, completes the muon system.

The luminosity system, an electron and photon tagger located downstream of the electron beam, gives a measure of instantaneous luminosity by measuring the rate of a well understood bremsstrahlung process.

Scintillator planes, the vetowall and ToF provide background discrimination by timing.

Information from all these subsystems is collected each bunch crossing and a trigger decision made. Once a trigger has fired, the data from all subdetectors is transferred to permanent storage for later analysis.

Continuous monitoring of the status of subdetectors is achieved by online reconstruction of certain data as well as slow control hardware monitoring.

Figure 2.3: *Side view of H1 showing the main subdetectors, with luminosity system shown below.*



## 2.5 Magnet

The H1 superconducting magnet is designed to bend charged particles passing through the detector to aid in their identification. The magnet consists of a superconducting solenoid (Nb-Ti & Cu) with an operational current of 5514 A, and an iron return yoke surrounding the main (LAr) calorimeter. A magnetic field of 1.15 Tesla is produced in a region 3.6 m long, with a diameter of 1.6 m. The magnet is cooled by circulation of helium gas cooled in an external heat exchanger.

The iron return yoke is an octagonal barrel parallel to the direction of beams. It is laminated and includes streamer tubes which make up part of the muon system. The tracking chambers require the B field to be known to 0.3% accuracy and the deviation from 'average' field is very small in the interaction region.

A compensating magnet at -4.4 m cancels the effect on the beam of the longitudinal magnetic field of the main coil. This allows longitudinal polarization of e-beam and minimizes any closed-orbit shifts caused by misalignment of the H1 magnet.

A toroidal magnet is part of the forward muon system and located at mean $z$=7.9 m. It has an inner radius of 0.65 m and an outer radius 2.90 m with a length of 1.2 m. The 12 coils of water-cooled copper have a current of 150 A passing through them. This produces a magnetic field which varies with radius from 1.75 T at 0.65 m to 1.5 T at 2.90 m.

## 2.6 Tracking

See Figures 2.4 and 2.5.

The H1 tracking system is designed to detect charged particles from an interaction and give information on their direction and momentum. There are three main parts to it. The central tracking detector (CTD), the forward tracking detector (FTD) and the backward proportional chamber (BPC).

Figure 2.4: *The forward trackers.*



It has been designed to reconstruct jets with high particle multiplicity and measure the momentum and angles of isolated particles to within $\sigma_p/p^2 \approx 3\times10^{-3}$ GeV$^{-1}$ and $\sigma_\phi \approx 1$ mr.

Track reconstruction in the central region is based on two large concentric drift chambers CJC1 (inner) and CJC2 (outer). The chambers have wires strung parallel to $z$ with drift cells inclined with respect to $r$ and achieve a resolution of 170 $\mu$m in the $r\phi$ plane and 1% of the wire length in the $z$ direction.

Two thin drift chambers, central inner (CIZ) and central outer $z$ chambers, aid the measurement of charged track momenta in the central region, with sense wires parallel to the beam direction. CIZ lies inside CJC1 and COZ lies between CJC1 and CJC2. These two chambers have a resolution of 300 $\mu$m in $z$ and 1-2% of $2\pi$ in $\phi$.

Multiwire proportional chambers provide level 1 trigger information over the full solid angle able to distinguish between successive bunch crossings. These are the central inner (CIP) and central outer (COP), forward (FWPC) and backward (BPC) proportional chambers. CIP lies inside CIZ and COP lies between COZ and CJC2.

Tracks with polar angle $\theta$ <30 $^{\rm o}$or $\theta$ >150 $^{\rm o}$are not reconstructed well in the CTD. The reconstruction of forward tracks is improved by having a high radial density of accurate space points, provided by many wires strung in the bending plane closely spaced in $z$. The FTD provides such information from three nearly identical supermodules. These each contain (in increasing $z$): three different orientations of planar drift chamber (good $\theta$ measurement) FWPC for fast triggering, a passive transition radiator (to aid in electron/pion discrimination) and a radial wire drift chamber ($r\phi$ information).

Figure 2.5: *Detail of Forward Trackers.*



## 2.7 Calorimetry

The subdetectors providing calorimetric information to H1 are designed to provide identification of and energy measurement of electrons, and penetrating charged or neutral particles as well as being able to measure jets with high particle densities. Good granularity provides some directional information. The calorimeter was placed inside the coil to limit the amount of dead material in front of the electromagnetic calorimeter.

All energy resolutions are expressed as a fraction or percentage :

$$\frac{x\%}{\sqrt{E}}$$

The energy is measured in GeV unless stated otherwise.

### 2.7.1 Liquid Argon calorimeter

See Figure 2.6

The liquid argon calorimeter (LAr) covers the central and forward regions of H1. It has two main parts, a hadronic part (4.5 to 8 interaction lengths) outside an electromagnetic part (20 - 30 radiation lengths $X_o$). The calorimeter has good segmentation (45000 cells) to optimize detector response and minimize the number and size of dead spaces ('cracks'). No cracks point toward the vertex, an arrangement known as semi-pointing geometry. Liquid argon was chosen because of its stability of response and proven technology.

Unlike the Zeus calorimeter, the LAr is non-compensating and this causes the response to hadrons to be ~30% less than that to electrons. Software corrections are made to the data offline. The calorimeter achieves an energy resolution of 10-13% / $\sqrt{E}$ for electrons and 50% / $\sqrt{E}$ for charged pions.

The calorimeter is segmented along the beam axis into 8 self supporting 'wheels'. The six barrel wheels are further segmented in the azimuthal ($\phi$) plane into 8 identical stacks or octants.

Figure 2.6: *Side view of liquid argon calorimeter.*

The hadronic stacks are made of welded stainless steel absorber with independent readout cells (containing liquid argon) between the plates. The orientation of the absorber plates is such that incident particles have angles $> 45^0$. The cells use a plastic board made of G10 to mount readout pads on. G10 is an epoxy resin+fibreglass construct. Each sampling cell has 19mm (16mm absorber and $2 \times 1.5$mm readout cell plates defining active region) stainless steel with a G10 board in the centre of the active region equipped with readout pads to collect charge deposited into the gap.

Electromagnetic (e.m.) stacks have readout cells composed of G10-Pb-G10 sandwiches separated by spacers defining liquid argon-filled gaps. The basic sampling cell consists of: 2.4mm Pb absorber, 2.35mm LAr as active material with (per gap) one readout plane and one absorber plane.

Signals are read out to preamplifiers located just outside the cryostat. After some multiplexing of signals 65000 channels are read out into analog receiving units (512 channels per unit). Single gain and double gain ADC boards are used to convert signals which are readout by DSP (digital signal processor) modules, Approximately 0.15% of channels are non-functional, a number which has remained stable since



installation.

### 2.7.2 BEMC

See Figure 2.7

The backwards electromagnetic calorimeter (BEMC) is designed to detect the electron from low-$Q^2$ (5-100 GeV$^2$) DIS events and covers an angular range of $150^{\rm o} < \theta < 176^{\rm o}$ corresponding to a pseudo-rapidity $\eta$ $-1.5$ to $-3$. The front of BEMC is at $z = -144$cm and the calorimeter is 45cm thick (22.5 radiation lengths, 1 hadronic absorption length) and consists of 88 stacks aligned parallel to the beam line.

Each stack is made of a lead-scintillator sandwich; fifty 4mm thick active sampling layers of plastic (SCSN 38) scintillator are interleaved with forty-nine 2.5mm lead plates. There are 56 stacks with a square cross-section ($15.7 \times 15.7$ cm$^2$), and 32 with trapezoidal or triangular shapes to approximate the size of the circular support barrel.

Each stack is read out by two pairs of 8cm wide wavelength shifters (WLS), on opposite sides of BEMC with a separate 16cm wide WLS covering only the last 15 sampling layers (6.8 radiation lengths) to give a separate measurement of e.m. showers. The output of the WLSs is fed to PIN photodiodes (pd), one pd per long shifter read out separately to measure light attenuation and give an impact position. The shorter WLSs have 2 diodes each because of width, but each pair of diodes is fed into a single readout because improvement of shower position is not expected. A total of 472 channels are used to readout the data from BEMC.

Four WLS bars make one stack. For each stack, the analog signals from the bars in that stack are summed to provide input for the inclusive electron trigger. A second set of stack sums are formed for the overall calorimeter trigger sums. The timing and gain of individual stacks are adjusted to provide the BEMC single electron trigger (BSET).

Figure 2.7: *X-y view of BEMC.*



The pulse shaping used to readout the BEMC signal mean that timing accurate to within 1 bunch crossing is not available except for selected information used in the trigger (BSET).

The energy resolution of BEMC is $\sim 20\%/\sqrt{E}$. Using light attenuation properties of the scintillator plates a position resolution of ~1.3 cm can be achieved (much better than stack dimensions of $16\times16$ cm$^2$). Electronic noise was measured at approximately 450 MeV per cluster, and attempts to lower this noise were made throughout the run. This noise was 'coherent', i.e. the noise from each cluster added together.

About 70% of hadrons passing through BEMC interact with the calorimeter, depositing, on average, about 30% of their energy. The minimum ionizing signal is only $2\sigma$ above the electronic noise level and remains undetected. Hadronic resolution of $\sim 80\%/\sqrt{E}$ has been achieved.

### 2.7.3 Tail catcher

The tail catcher measures hadronic energy which escapes from the LAr calorimeter in order to give a more accurate total energy measurement. It utilizes the pads attached to 11 of the 16 limited streamer tube (LST) layers of the instrumented iron (see section 2.8.1). Two sets of LST layers are summed longitudinally by tower builders (TB), forming front tower signals from the 5 inner layers and back tower signals from the 6 outer layers. Pad size is 30 cm$\times$30 cm in the the endcap and 50 cm$\times$40 cm in the barrel region.

Analog signals from the TBs are passed out to superboards (containing 128 channels) which amplify and integrate the signals. There are 3888 channels total, and details of coverage is given in the table below. The tail catcher achieves an energy resolution of $\sim 100\%$ / $\sqrt{E}$

| Region | $\theta$ | Segmentation | # of channels |
|---|---|---|---|
| Forward endcap | $6^{o} \leq \theta \leq 33^{o}$ | $x$ and $y$ | 552 |
| Central barrel | $33^{o} \leq \theta \leq 137^{o}$ | $\phi$ and $z$ | 2784 |
| Backward endcap | $137^{o} \leq \theta \leq 172^{o}$ | $x$ and $y$ | 552 |

### 2.7.4 Plug

The plug is designed to close a gap in acceptance between the beampipe and the forward part of LAr in the region $0.6^o < \theta < 3.0^o$ in order to have better energy flow measurements. Though far forward in $z$, it is used to minimize the missing part of the total transverse momentum.

Geometrical constraints come from the size of the return yoke limiting the plug to a cylinder with a diameter of $\sim 0.7$ m and a length of $\sim 0.7$ m. The sampling calorimeter is made up of 9 copper absorber plates and 8 interleaved sensitive layers of large area silicon detectors. Important construction parameters are given in the table below:

| | |
|---|---|
| Position | $(+)476 \leq z \leq 545$ cm |
| Overall radius | $6 \leq r \leq 32$ cm |
| Radius detector planes | $6 \leq r \leq 25$ cm |
| Polar angle range | $12.5 \leq \theta \leq 58$ mr |
| Number of detectors | 672 |
| Total length | 69 cm $\equiv 4.25\lambda_{abs} \equiv 44.6X_0$ |

Each detector board has 44 Si detectors - 32 quadratic 6 triangular and 4 rectangular giving a 96% coverage of the area. Two boards cover the $xy$ detector plane. Pairs of detectors are merged into 336 readout channels. Trigger towers are formed by merging signals from consecutive channels in $z$.

The plug does have some problems. The sampling is fairly coarse, and there is some lateral and longitudinal leakage. Energy resolution is $150\%/\sqrt{E}$, sufficient for its function however.

## 2.8 Muon system

### 2.8.1 Instrumented Iron

See Figure 2.8.

The iron return yoke of the H1 magnet is interleaved with limited streamer tubes (LST), some of which are used in the tail catcher, but most of which form the instrumented iron muon system. The system is designed to detect and measure tracks caused by penetrating muons and covers angles $5^o < \theta < 170^o$.

The LSTs are made from halogen free luranyl (plastic). The basic element of the system is an 8-fold profile with cell size $10\times 10$ mm$^2$. A silver coated Cu-Be wire



(100 $\mu$m diameter) at ground potential runs along the centre of each cell. Profiles are coated in low resistivity paint and the HV applied to this surface. The top of the profile has a luranyl cover ($\sim$10 M$\Omega$). Profiles are paired in boxes and several boxes are combined into one streamer tube layer. Strips or pads (depending on the tubes purpose) are glued to the high resistivity side of the layers, and the entire layer electrically isolated from the iron.

Pads are used for energy measurement with some granularity in depth and are part of the tail catcher, while the strips provide 3-D space points for tracking purposes.

A total of 13000 profiles in 911 streamer chambers are arranged in 16 layers depth in gaps in the iron yoke. From the interaction point outwards there are:

- 1 so-called 'muon box' of 3 layers (2 with strips perpendicular to wire direction, 1 with pads)
- 3 gaps with pad layers in each
- 1 larger gap with 1 strip and 1 pad layer
- 5 gaps with pad layers in each
- outside the iron another 'muon-box'

The chambers are filled with a non-flammable gas ( $CO_2$,argon,isobutane in the ratio 88:2.5:9.5). The chambers can be operated at low voltage (3000V) for injection and have a standard operating voltage of 4500 V. Read out crates (ROC) each read out 12300 digital channels representing 24 chamber planes of 512 channels each. A maximum readout rate of 300-500 Hz is possible.

Wire hits can be reconstructed with a resolution of 3-4 mm, strip hits with 10-15 mm resolution and pads have a 10 cm resolution.

Figure 2.8: *The muon system, showing arrangement of the streamer tubes.*



### 2.8.2 Forward Muon System

See Figure 2.9

The forward muon system is located outside the iron yoke between $z$=6.3 m and $z$=9.5 m. It utilizes drift chambers either side of a toroidal magnet (to bend the particles passing through and aid in momentum resolution) to cover polar angles $3^{o} < \theta < 17^{o}$. It is designed to measure high energy muons with a lower limit of 5 GeV (from material in front of the chambers and multiple scattering in the toroid) and an upper limit of 200GeV (because of the toroid field strength).

The six drift chamber planes, three on each side of the detector, are arranged as shown in Figure 2.9 and contain 1520 drift cells in total. The planes increase in size from ~4 m diameter ($z$=6.47 m) to ~6m diameter ($z$=9.33 m) and are divided into octants supported on an aluminium frame. Four planes have their drift cells aligned to measure polar angle $\theta$ providing measurement of momentum , and the remaining two planes measure the position in $\phi$.

Each plane consists of a double layer of drift cells staggered by half a cell width. This allows left-right ambiguities to be resolved and $t_0$ measurements to be made. Drift cells have a rectangular cross-section of depth 20 mm, width 120 mm and lengths between 400 mm and 2400 mm. A central sense wire runs longitudinally along the cell giving a maximum drift distance of 6 cm. The sense wires of adjacent planes are joined by a resistor allowing determination of track position both transverse to and along the direction of the wire.

Figure 2.9: *The forward muon system, with detail of drift cells.*



The gas used is argon;$CO_2$;methane in a ratio of 92.5;5;2.5. Charged particles passing through ionize the gas, the charge from this moving through the drift field to the sense wire, which is maintained at high (positive) voltage. Drift velocity is $\sim$50 mm/$\mu$s.

Charge and time analysis is performed using the rise and peak of the pulse from each wire. Position resolution is $\sim$250 $\mu$m, momentum resolution is 24% at 5 GeV falling to 36% at 200 GeV. Tracks are reconstructed in three stages. First, hits in each double layer are paired, these pairs are associated into track segments on each side of the toroid and finally track segments are linked through the toroid.

## 2.9 Luminosity System

The luminosity system consists of two main parts, the electron tagger (ET), located at $z$=-33.4 m, and the photon detector (PD), at $z$=-102.9 m. It is designed as a multipurpose device. Its main purpose is to measure instantaneous luminosity with a statistical precision of $\sim 2\%\mathrm{s}^{-1}$ under nominal conditions. It also measures absolute luminosity in the interaction region ($\sim$5% accuracy), provides electron beam monitoring for HERA, tagging of photoproduction events and energy measurement of small angle scattered electrons and radiative photons from initial state radiation.

The luminosity system is designed to detect electrons which have interacted with the proton and given off a photon which is detected in coincidence with the electron. The angular distribution of these particles is peaked in the direction of the e-beam (polar angles $\sim$19 $\mu$r) so the detectors need to be very close to the beampipe and far away from the interaction point.

Scattered electrons are bent by magnets between -5.8 m $> z >$ -23.8 m to pass through an exit window at $z$=-27.3 m. The photons leave through an exit window at $z$=92.3 m pass through a Pb filter (2 radiation lengths - $X_0$) followed by a water Cerenkov (1 $X_0$) counter to protect the PD from the high synchrotron flux. The water counter can be used as a veto (VC) to select only clean events where the bremsstrahlung photon passes through the filter without interacting.

Both ET and PD are on remotely controlled movable platforms and can be moved down from the beam pipe to protect the detectors during beam injection.

Luminosity is calculated from Bethe-Heitler events, $ep \rightarrow ep\gamma$, which have a large and precisely calculable cross-section. Background comes from beam gas events ($eA \rightarrow eA\gamma$) which at design luminosity occur at $\sim 10\%$ of the $ep \rightarrow ep\gamma$ rate. This background is measured using the pilot bunches.

The table below summarizes important information on the luminosity system assuming nominal beam conditions and design luminosity.

| Measurement | unit | ET | PD |
|---|---|---|---|
| Energy interval, $E_\gamma/E_e$=1-$E_{e'}/E_e$ | | 0.2-0.8 | 0.004-1.0 |
| Polar angle acceptance interval | mrad | 0-5 | 0-0.45 |
| Average acceptance for luminosity events | % | 48 | 98 |
| Average acceptance for photoproduction events | % | 38 | - |
| Visible $ep \rightarrow ep\gamma$ cross section | mb | 28 | 174 |
| Luminosity rate for $E > E_{thr} = 4$ GeV | MHz | 0.4 | 1.3 |
| Photoproduction event rate | Hz | 20-30 | - |

The system can tag quasi-real photoproduction events with $Q^2 < 0.01$ GeV$^2$ in the energy interval $0.2 < E_{e'}/E_e < 0.8$. For these events only energy in the ET is used for triggering with the PD and VC used as a veto. In coincidence with main detector trigger elements this suppresses proton induced background by a factor 200 and enriches the photoproduction physics sample by a factor of 20.

The detectors themselves are total absorption Cerenkov calorimeters, made of KRS-15 crystals, formed into a hodoscope. Each cell of the counter is read out by a separate FEU-147 photomultiplier tube (pm). The table below summarizes their characteristics:

| Parameter | unit | ET | PD |
|---|---|---|---|
| Aperture | mm$^2$ | 154×154 | 100×100 |
| lateral granularity | | 7×7 | 5×5 |
| Radiation length $X_0$ | cm | 0.93 | |
| Moliere radius | cm | 2.10 | |
| Crystal length | cm | 20 | |
| Time resolution | ns | <3 | |
| Energy resolution | % | $1 \bigoplus 10$ | |

The VC has two pms working in different modes. The first is standardly included in the photon detector trigger. The second operates with increased voltage to react with 100% efficiency to e.m. showers from photons with $E_\gamma$ >1.5 GeV. The veto signal in the trigger branch is an OR of these two signals.

Both detectors are continually re-calibrated during data taking using the energy constraint $E_{ET} + E_{PD} = E_{Beam}$. This gives an absolute calibration of better than



1% although individual calibration constants may change by up to 5-20% during a run.

## 2.10 Scintillators

There are two main subdetectors using scintillators, ToF and the vetowall. Both are designed to trigger when penetrating particles travelling with the proton bunch pass through. This trigger can be used to veto events at the level 1 trigger (Section 2.11.1).

### 2.10.1 ToF

See Chapter 3.

### 2.10.2 The vetowall

See Figure 2.10.

The vetowall is made up of two parts, the outer vetowall and the inner vetowall, located at distances of $z$=-6.5 m and -8.1 m respectively. Each has two planes of scintillator, each plane being identical.

The inner vetowall covers the area near the beam down to a radius of 11cm. The four pairs of counters (NE114 6mm thick) cover a total area of 100×90 cm$^2$ and are read out via 2 photomultipliers each. The counters are shielded against e.m. showers (synchrotron radiation) by 4 cm thick lead walls. Penetrating particles are identified by coincidences between two scintillators with a time resolution of ±3 ns.

Figure 2.10: *The vetowall xy view*



The outer vetowall has 20 large counters in 2 pairs of 10, the largest with an area of 2.1 $\times$0.9 m$^2$. The wall covers a total area of $\sim$ 5$\times$4 m$^2$ which overlaps (in $x$-$y$) the inner vetowall and most of the liquid argon calorimeter and endcap.

The counters are made of 1 cm thick plastic (NE110) scintillator attached to twenty 5" pms (VALVO XO 2041) in mu-metal shield to protect them from the ($\sim$ 10 mT) fringe fields from the main and compensating magnets of H1. A large iron wall with a thickness of 5 cm separates the the walls of the large veto wall.

A 3m concrete shield between the vetowall and H1 protects the experiment from low energy showers of beamgas remnants.

Coincidence resolution of $\pm$8 ns is dominated by the long flight path of photons produced in the scintillator. Light attenuation over distances of $>$ 1.5 m leads to inefficiencies of $< 10^{-5}$ in detection of minimum ionizing particles. The time resolution is easily enough to separate e-and p-related events, but beamgas/beamwall interactions occurring between the VW and the detector itself can obviously not be detected. These are covered by ToF.

QMW was responsible for the logic forming the trigger signals from the vetowall as well as monitoring online the performance of the VW. Coincidences from pairs of laterally parallel counters are formed in NIM logic. These coincidences are strobed into 3 windows : background (BG - covering the time proton background particles are expected) interaction (IA - covering the time interactions from the vertex are expected) and global (GL - covering one bunch crossing). Two of these (background and global coincidence) are sent to the CTL for inclusion as trigger elements.

Online monitoring of amplitudes, rates and efficiencies takes place via a CAMAC-Macintosh system, with 42 individual channel counter coincidences read out to the data acquisition in interaction and global gates.

## 2.11 Trigger

The purpose of the H1 trigger is to select interesting $ep$ collisions from background interactions. It is formed of four levels of triggers, each of which studies information from the detector with increasing depth and attempts to reject background at each stage.

Data from each subdetector is pipelined locally for between 27 and 35 beam crossings and given a beam crossing identifier. Each subdetector sends digital *trigger elements* (containing a compressed fraction of the subdetector's data) to the level 1 trigger. These are combined into *subtriggers* from which an initial decision is made to reject or keep the event. If an event signal (L1keep) is given, all subdetectors stop recording information and the data in their pipelines is read out. Once this is finished each subdetector clears its pipeline and awaits initialization from DAQ (Section 2.13) before it begins collecting information again. Higher trigger levels further analyse the full data and a final decision is made to accept or reject the data. Once an event is accepted, the information for that event is stored permanently on cartridge.

The only essential difference between $ep$ and $eA$ interactions is the location of the point of interaction. Given the bunch sizes and separations $ep$ collisions can occur only within a given volume of space, inside the detector. Tracks with an origin outside the detector can therefore be used to eliminate background. There is also, however, a source of background from within the area of $ep$ collisions, caused by beam gas interactions. Further cuts are necessary to remove these.

Useful subtriggers vary from run to run according to conditions within the detector (only the electron beam for instance) and so a set of 'standard triggers' is set up for various running conditions. A (programmable) trigger mask is used to deactivate (in hardware) unwanted trigger elements.

### 2.11.1 Level 1

The level 1 trigger (L1) correlates the trigger elements sent from each subdetector, and a decision to reject or accept the event is made within 2.2 $\mu$s (22 beam crossings). The pipelining of data means that the L1 decision introduces no deadtime, and so no loss of potential physics events. Only if the event is accepted and reconstructed at higher levels (L2, L3 or L4) is any deadtime introduced.

Combinations of trigger elements are formed into subtriggers by the L1 trigger, as described in section 2.11.2. A vertex requirement and/or a veto (provided by separate, specific trigger elements) is placed on certain subtriggers to improve the quality of the data taken with that subtrigger.

The rate at which subtriggers arrive at L1 is, depending on the subtrigger, often too high for the data from each trigger to be stored permanently. In order to limit



the number of triggers to a reasonable level each subtrigger has a separate prescale factor applied to it. This is an programmable number which causes the trigger to ignore the first $n$ triggers ,where $n$ is the prescale factor, and let only the $(n+1)$th trigger be counted. This process is repeated as soon as the $(n+1)$th trigger has fired.

Subtrigger data is formed into four 32 bit words, each bit corresponding to a specific subtrigger and set only if that subtrigger fired in that event. Raw subtriggers are formed from the unprescaled triggers, and actual subtriggers are formed from the triggers which survive prescaling. The OR of the four actual subtrigger words is used as the L1keep signal: if zero the event is rejected, if not then the event is read out to be further analysed by higher levels of the trigger.

### 2.11.2 Subtriggers

There are many subtriggers, each with its own purpose in helping identify an $ep$ collision. Here only the main categories are covered. See Appendix B.1 for more information. These include :

1. Veto signal. Signals from ToF indicate background events which occurred outside the detector and these signals are used to provide a veto for certain subtriggers.

2. Z vertex. An estimation of the $z$ vertex position is made from all tracks in the central and first forward proportional chambers.

3. Forward ray. Forward tracks analysed to find any rays pointing backwards towards a vertex.

4. Other tracking triggers.

5. Calorimeter trigger. These include localized energy sums, a total energy sum, time of event ($t0$). The BSET trigger attempts to identify scattered electrons.

6. Muon triggers.

7. Luminosity trigger. Can detect scattered electron and photon from photoproduction events.

### 2.11.3 Level 2 (L2) and level 3 (L3)

The level 2 and 3 intermediate trigger levels are designed to operate during the deadtime caused by the readout of event an event after the L1keep signal. For the 1992 and 1993 runs these were not installed.

The design parameters foresee that L2 processing be finished within 20 $\mu$s and the L3 decision be made within 100$\mu$s. The data acquisition system can handle a maximum rate from L3 of 50Hz. With a typical deadtime of 1ms for fully accepted events, the L1 (L2) trigger should not exceed a rate of 1000 Hz (200 Hz) if the deadtime is not to exceed 10%.

During the 1992 run the level1 trigger was forced to keep to 50 Hz by the DAQ data acceptance limit. This was offset by the low background level from the beams running at 1% of design luminosity.

### 2.11.4 Level 4

The level 4 (L4) filter farm is an asynchronous software trigger which uses the raw data from an event as the basis for its decision-making. In 1992 fourteen processor boards ran in parallel, each processing one event until a decision is reached on that event.

The algorithm used by the L4 filter is composed of discrete logical modules which partially reconstruct the event. Certain criteria are used to decide whether an event is to be rejected, and as soon as one of these criteria is met, reconstruction stops and the next event is processed. This helps minimize the deadtime introduced by this method.

The actual rate of triggers taken is about 5-10 Hz.

## 2.12 Slow control

The slow control system is designed to be an alarm system for hardware failures (BBL3) and also to monitor quantities from subdetectors which should remain constant. These include high voltage settings, gas pressures, and other mundane but vital numbers. Each so-called slow channel (SC) corresponds to one of these quantities. The nominal values of each SC are maintained in a database. Subdetectors are initialized with by their subsystem in accordance with values from this database.



If a SC differs significantly from its database value, a microevent occurs. Microevents are stored in a slow event buffer until enough microevents are stored, the status of an SC changes, a set time has passed, or a direct command to take a slow event (SE) is received. A SE is then sent to the central slow control computer. Slow events are stored in database form for later analysis.

Slow control alarms are sent if problems are detected in slow events.

## 2.13 Data acquisition

The data acquisition system (DAQ) controls the readout and storage of raw data for each event. There 270000 analog channels which are read out and digitize taking up $\sim$3 Mbyte per event. The DAQ zero suppresses and reduces the data volume to 50-100 Kbyte per event, which saves on data storage room by a factor of 25 and speeds event taking. The system used currently has a transfer limit of 1.2 Mbyte $s^{-1}$ which defines the upper limit on the rate of data taking ($\sim$ 16 Hz).

The DAQ is conceptualized as three distinct parts:

1. Branches. Subdetectors store and digitize data in a format suitable for transmission. Each branch is independent from the others.

2. Consumers. Subsystems monitor and record data onto permanent storage media by receiving and collating information from the branches

3. Controllers. External processes initiate and control the system allowing outside intervention.

Each branch has a central subdetector crate which passes information into a fibre optic taxi ring when commanded by the controller. The branch is autonomous up to this point, allowing branches to be removed without problem during normal running. Subsystems also have subsystem trigger controllers which independently coordinate each system's response with the CTL. Data is held within multi-event buffers (MEBs) within each subsystem.

The event coordinator controls all management processes and during acquisition searches all subsystems' MEBs for next event. Once all subsystems have returned the same event number the DAQ reads the event out.

# Chapter 3

# ToF

## 3.1 Physics in the Backward Area

### 3.1.1 Low-$Q^2$ and low-$x$ physics

The kinematics of interactions at H1 causes a large fraction (90%) of DIS events to lie in the region $10^{-4} < x < 10^{-2}$ and 20< $Q^2$ <100 GeV$^2$ (See Section 1.4, Figure 1.9). During the first two years of running of HERA, the low luminosities (1% of design) mean that these areas will be the most important as they have a reasonable number of events.

Photoproduction physics occurs within the kinematical range 0< $Q^2$ <10 GeV$^2$.

### 3.1.2 Observing Physics in the Backward Area

The backward area of H1 contains BPC, BEMC and ToF (See Figure 3.1), and it is in this area that early physics studies are mostly directed. Low-$Q^2$ interactions, which dominate, lead to the electron being scattered through small angles and passing through BPC and BEMC, while low-$x$ events can have hadronic fragments from the proton boosted in the backward direction.

Other particles, as well as those from this physics process, also pass through the detectors. Those particles which are associated with the proton beam can be separated, by timing, from those associated with the electron beam, using ToF.



Figure 3.1: *The backward area of H1, showing the location of ToF, BEMC and BPC.*

The five main sources of particles passing through the subdetectors in the backward area are:

- particles from the interaction point,
- beam halo travelling with, but displaced from, the proton beam,
- secondaries—hadronic fragments travelling with proton beam,
- synchrotron radiation from the electron beam.
- hadronic secondaries from e-gas interactions.

The time difference between the halo/secondary signal and the interaction signal is dependent on the position of the detector, but in the backward area the beam halo signal is always before the interaction signal. Synchrotron radiation and e-gas secondaries have a similar (but not identical) time distribution to each other and to physics events.

### 3.1.3 Beam Halo

Beam halo travels with each proton bunch and effectively 'fills' the beam tunnel, but is concentrated around the beam pipe. It consists of muons produced from pions which were in turn produced from protons which have escaped from the magnetic field and interacted with the material of the beam pipe. These particles are travelling at the same effective velocity as their associated proton bunch and so arrive at the detector simultaneously with the bunch.

They are travelling parallel with the beam and so pass through a large length of the detector.The particles can leave a significant amount of energy distributed in small quantities equally throughout its path. These tracks can pass through calorimeters specifically designed to detect transverse energy radiating out from the interaction point. The muon can deposit energy in each cell of the detector and so can appear as a shower of particles from an interaction, causing a false trigger in the calorimeter.

### 3.1.4 Secondaries

This is the name given to hadronic particles produced by collisions of protons with matter very close to the beam. Several sources of such radiation are present in the backward area.



1. Collimator
2. Getter Pump
3. Beam pipe itself

The secondary particles will leave similar signals in the apparatus as 'physics' particles from the e—p collision point. Their only difference is their timing, energy spectrum and position of origin.

### 3.1.5 Synchrotron Radiation

Synchrotron radiation is produced by the electrons in their beam radiating off energy. This synchrotron radiation is a continuous spectrum (peak at 100 KeV) and travels in time with the electron beam. Thus energy will often be deposited in the interaction window (see Section 3.2.5). Fortunately this radiation can be absorbed by a few mm of lead ($X_0 = 5.6$mm).

### 3.1.6 E-gas interactions

These interactions occur inside the beam pipe with a much smaller cross-section than for the proton beam. As the particles are hadronic, they are much more penetrating than synchrotron radiation. The expected rate for e-gas events is $\sim$10 Hz for 5 mA of electrons, a typical value for 1992-3 runs.

### 3.1.7 Associated problems

The problem caused by the beam halo and secondaries is one of triggering. If halo is travelling with a particular bunch crossing, it will cause subdetectors to trigger even if no interaction particles are present. Neither the trackers nor the calorimeters are fast enough to resolve the time difference between the halo and the physics signals, which is the easiest and fastest way to differentiate between the two.

The rate of these triggers is very high, typically 5000 Hz for the 1993 run, which can cause a problem. While the detector is reading out data from an event, no more triggers can be accepted until the read-out is finished 2.2 $\mu$s later. If the trigger rate from background events is high enough, the detector will be continually reading out. This will lead to huge dead-time losses of interesting physics events which are missed while read-out takes place. There is also a problem with sheer volume of information. Only a limited pipeline is available from the data acquisition to the storage area, and so the maximum trigger rate the system can handle is a few tens of hertz.

### 3.1.8 Solutions

To overcome this problem it was necessary to introduce a separate subdetector which covered the whole area of beam halo and was able to distinguish between the halo and the physics. As it is not possible to distinguish the two using the different energies the time difference and position of the halo is utilized as a trigger.

Initially a single subdetector, the vetowall, was installed a few metres away from the interaction point in the backward direction. The device consists of a pair of scintillator walls that extend around the beam pipe to fill the same area as the tunnel, although it is actually just inside the experimental area, providing coverage for the outer part of the main detector. When a beam halo event is seen a 'veto' signal sent to the trigger which can be used to prevent spurious data being taken.

Monte Carlo simulation of background indicated that the vetowall was insufficient to give total coverage of the main detector. Particles which interacted with the beam pipe after passing through the vetowall position would not be vetoed. Neither would hadronic particles emerging with a small angle, which were within the beam pipe itself when the bunch passed through the vetowall.

This meant that a small area of detector next to the beam pipe would be vulnerable to these false triggers, which occurred at a high rate. In order to provide coverage for the BEMC against these a second subdetector was installed in the experiment, outside BEMC and inside the warm cylinder. This subdetector is called the time-of-flight wall, or more commonly ToF, and is also an array of scintillation counters, or hodoscope.

Originally, ToF was to have been built by Hamburg University and some initial feasibility studies were performed on the scintillator and light collection techniques [14]. Hamburg was unable to build ToF, however, and Queen Mary and Westfield College designed and built it. The Hamburg studies were used as a starting point for the design and the truncated cone light collection technique was utilized in the final design.



## 3.2 ToF

The time-of-flight detector is a pair of scintillator walls located in the backwards area of the H1 detector between BEMC and the nitrogen shield.

### 3.2.1 Design: Requirements and Restrictions

In order to be able to physically fit inside the nitrogen shield ToF must be less than 400 mm thick. It covers as large an area of BEMC as possible, to maximise the vetoing of unwanted particles, and has a granularity matching the BEMC stacks to provide extra information about 'real physics' particles.

ToF is able to distinguish between the beam halo particles and the real physics particles arriving 13-15 ns later. It is able to come to a logical decision fast enough (3 bunch crossings) to be part of the level 1 trigger in H1 (which makes its decision in 22 bunch crossings). It is able to work in the H1 magnetic field of 1.15 T.

In order to be able to reach inner detectors within the warm cylinder, ToF is demountable, without the need to break the beam pipe. Thin lead sheets protect the counters from the large amounts of synchrotron radiation expected in the apparatus. Also, during initial periods of beam, the area covered by the inner counters could be exposed to high levels of radiation concentrated near the beampipe. To minimize damage from such radiation, the centre counters were mounted on shutters which allow horizontal movement up to 200 mm away from the beam pipe. The shutters are pneumatic to avoid magnetic field interaction problems which would affect electromagnetic stepper motors and are remotely controlled from the electronics chariot ('rucksack') which contains the rest of the ToF readout electronics.

### 3.2.2 Construction of ToF

ToF was designed and built by QMW College London, with help from the University of Birmingham in the construction phase in Germany. See Figures 3.2, 3.3, 3.4, 3.5.

#### Overview

The apparatus consists of two parallel planes of plastic (NE104) scintillator mounted perpendicular to the beam line on a stainless steel frame with photomultiplier tubes (pms) attached horizontally to the scintillator (see Figure 3.2). Each wall of ToF is made up of smaller counters to help rapid detection of particles passing through. The counters are mounted on a (non-magnetic) steel frame to minimize eddy currents in a magnet quench.

### Details of construction

The walls of ToF (called ToF 0 and ToF 1) are each 30 mm thick NE104 plastic scintillator and made up of smaller pieces (referred to as counters) each with a separate photomultiplier tube. ToF 0, located at $z$=-2.25 m has 8 counters, measuring $317 \times 634$ mm$^2$. ToF 1, located at $z$=-1.95 m has 16 smaller counters measuring $317 \times 317$ mm$^2$. This wall is next to BEMC and has the same granularity as a BEMC stack.

The tubes are mounted horizontally (perpendicular to the scintillator) and a raised bevel mount (2) is used to collect light from the scintillator. The mount is a truncated cone attached to the surface of the scintillator of a similar size to the sensitive area of the PM tube. On the opposite surface of the scintillator, centred on this cone, a 'countersunk' hole (1) was drilled. Photons produced within the scintillator (2) are then reflected up into the PM tube (5). The whole pm assembly is held against the bevel mount by springs to ensure a minimum gap between the pm and the light guide.

The photomultiplier tubes are Hammamatsu 2490-01 PM tubes, these work in a high magnetic field but with gain reduced by a factor of 100. There is an amplifier ($\times$40) built by D. White of RAL into each photomultiplier base to partially offset this effect.

The six inner counters, four on ToF 0 and two on ToF 1, are mounted on pneumatic shutters, remotely controlled from the rucksack or the ToF DAQ and control MAC. This enables these counters to be moved up to 200 mm horizontally away from the beam line. This feature was incorporated in case of damagingly high levels of radiation near to the beam itself during early beam tuning exercises. Pneumatic rams were chosen, over electromagnetic stepper motors, because they are unaffected by the magnetic field of H1.



Figure 3.2: *X-Z cutaway diagram showing bevel for reflecting light into photomultiplier.1 Countersunk hole. 2 Scintillator. 3 Truncated cone. 4 Metal shield. 5 Photomultiplier tube (pm). 6 Base for pm.*

Lead plates, 6.4 mm thick, cover each counter on the inside of each wall in order to absorb synchrotron radiation and prevent this from 'ageing' the counters (6.4 mm = $1.1X_0$). They will also prevent coincidence hits in both walls simultaneously, as well as protecting BEMC from such radiation.

Each counter has its own high voltage (HV) supplied by a LeCroy 4032a HV unit, capable of providing up to 3.3 kV with max output of x mA per channel This is required because differences in pm-tube manufacture, slight differences in the pm-tube-scintillator interface, and ageing of the scintillator will lead to each counter having its own operating voltage. The method of determining this voltage is given in Section 4.4.2 (plateauing).

Figure 3.3: *XY view of both walls of ToF, as if the viewer was standing at the interaction point.*

The whole apparatus can be demounted from the beam pipe by separating the top counters (plus the shutters) from the bottom ones. This allows rapid access to subdetectors further inside the warm cylinder, such as BEMC. The whole process takes ~2 hours.



Figure 3.4: *YZ view of ToF, with protons travelling right to left.*

### 3.2.3 Extracting light from the Scintillators

Scintillation counters allow for the rapid detection of charged particles, including minimum ionising particles (mips) which deposit a relatively small proportion of their energy in the scintillator. Charged particles passing through the scintillating material excite electrons which then rapidly (~1 nanosecond) de-excite by emitting a photon. These photons then travel through the scintillator, possibly exciting/de-exciting further electrons. The photons produced can be detected by means of a photomultiplier tube placed against one edge of the scintillator, usually via a light guide to match the area of the photomultiplier tube to the area of the scintillator. The transit time of photons travelling through the scintillating material is only a few (~0.5-3.0) nanoseconds (see section 4.4).

This rapid detection of particles is fast enough to differentiate background particles from interaction particles by their timing. Standard photomultiplier tubes necessary to the device are unable to work in the H1 magnetic field. A$\beta$-field of only a few hundred Gauss causes photoelectrons produced inside the pm-tube to be deflected, missing the amplifying dynodes.

To get around this problem, light-guides can be installed on one face of the scintillator wall (usually the smallest) to transmit light from the scintillator to a pm mounted away from the magnetic field. Roughly equal numbers of photons reach and pass through each outside face of a rectangular piece of scintillator regardless

Figure 3.5: *Schematic figure showing ToF 0 and ToF 1. Detail of bevel mount for scintillator and the position of the lead shield is shown. 1. Scintillator. 2. Steel mounting frame. 3. Lead. 4. Bevel mount. 5. Metal shield containing photomultiplier tube and base.*



of its dimensions, so it is best to choose the smallest face and match this to the sensitive area of the pm-tube being used.

Unfortunately there was no room in the backward area for the light guides necessary to bring the light out from the scintillator. A possible way around this was to use optical fibres, but it was found to be impractical for a number of reasons (bending of the fibres, low light transmission).

Because it was impossible to transmit the light out of the detector, it was decided to locate the pm-tubes inside the magnetic field. This required the use of special high-field pm-tubes. The pm-tubes chosen (Hammamatsu 2490-01) had to be parallel to the magnetic field in order to function and so had to be placed in the centre of the *largest* face of the scintillator, perpendicular to it.

This led to further problems: the amount of light collected in this way would be much less than that of a conventionally mounted pm-tube. The sensitive area of the pm-tube is $\sim$2500 mm$^2$ compared to the scintillator area of $\sim$100,000 mm$^2$. Thus only about 2.5% of the light reaches the pm in a concentrated burst. In addition to this loss, the high-field pm-tubes provide a gain $\sim$ 100 times less than normal when operating in the H1 magnetic field.

In order to overcome this problem the scintillator was made much thicker than in standard scintillation counters to allow each particle more material to interact with, and so produce more photons. A bevel mount (described in Section 3.2.2) was used to collect some of the light which would have escaped through the thinner edges of the scintillator.

### 3.2.4 Read-out and DAQ

There are 24 signals (1 for each counter) which are fed through NIM logic and read out via CAMAC (for local monitoring) and VME (for central DAQ- Data AcQuisition). The NIM logic discriminates the input pulses and then determines if they are in any of 3 time windows (see Section 3.2.5). The logic is located in the 'rucksack' (an electronics trailer attached to the side of H1, outside the shielding wall) on the 1st floor in racks G13 and G14.

### 3.2.5 logic

The logic is designed to send a trigger signal to the CTL (Central Trigger Logic) whenever there is a hit in both walls of ToF within a given time window (see below). Please study the logic diagram (Figure 3.6) whilst reading this section.

The input signals are processed individually to begin with. First they are discriminated and fanned-out into 5 outputs per incoming channel. Of these outputs, 3 go to separate strobed coincidence units, 1 goes to a CAMAC controlled OR and 1 goes to a TDC stop via a suitable (160 ns) delay to ensure the data arrives later than the start pulse (defined by the HERA clock).

The 3 coincidence units are strobed by 3 individually timed pulses which are defined relative to the HERA clock. Any hits occurring within these strobe windows are fanned-out and passed through further logic to define these 3 triggers:

1. Interaction. A hit in a time window ∼15 ns wide in time with particles from an interaction (green symbols on logic diagram).

2. Background. A hit in a time window ∼20 ns wide in time with the background particles associated with the proton beam (red symbols on logic diagram).

3. Global. Any hit in a time window ∼90 ns wide. This window encompasses both of the previous ones (blue symbols on logic diagram).

Hits occurring outside these time windows are ignored, but in principle very few hits should occur outside of the global window. The widths of these windows were changed during the running period in the light of experience. See Appendix C.1.6 for details.

There are 4 outputs from each coincidence unit for each incoming signal The first of these channels passes through more logic and is used for the trigger. The other outputs go directly to scalers and such like (see diagram). All 3 coincidence units have outputs to the MWPC (Multi-Wire Proportional Chamber) receiver card (labelled RC on the diagram) and scalers. The MWPC read-out contains the non-trigger ToF information sent to the central DAQ.

The Brussels Group (who looked after the MWPC readout) kindly allowed the use of their readout because of financial constraints on ToF and the availability of spare channels in their system.



Only the Global strobe has a Plateau output, the others have an output to the BEMC DAQ. The Plateau output is used in ongoing efficiency checks on the ToF scintillators as is explained below.

The trigger output for each of these windows is ORed separately over the counters of each wall.The ORed outputs from each wall are ANDed together, still keeping the signals for each window separate. This results in 3 output trigger signals.

The logic was changed during the 1993 run to provide edge-triggered timing of events. This would help minimize events being labelled as both interaction and background. The effects of edge triggered logic on the data are described in Section 4.6.1.

There is also some logic for starting and resetting the TDC's and scalers (this is coloured yellow on the logic diagram), which occurs the bunch crossing after any data is found in any channel. The HERA clock signal is used as a starting pulse for these, and also as a reference to label any event as being in one of the 211 bunch crossings. A 'first bunch' signal from the central trigger is used as an absolute reference point. This latter part of the logic is labelled 'Bunch I.D. Monitoring'.

Flash analog to digital converters (FADCs) were used as FTDCs (flash time to digital converters) to store the time of signals from individual ToF counters in the global window for offline reconstruction. Certain ToF triggers (see Appendix C.1.1) were also sent. The FTDCs used were part of the central tracking system, and the reconstruction of the FTDC data is described in Chapter 6.

### 3.2.6 Capabilities

ToF is designed to differentiate between particles passing through it in time with the proton beam and particles passing through from the interaction point. Particles passing through the scintillator will not be absorbed fully but will cause excited atoms to release photons which are reflected through the material and detected by the photomultiplier tube.

The NE104 scintillator has a decay constant of 1.9ns. This is the time for 1/e of the excited atoms to release a photon. This transmission through the scintillator takes up to 5 ns (depending on hit position) in the larger counters (ToF 0) and slightly less in the smaller counters. There is an unknown delay within the PM tubes themselves, caused by the internal amplification and reamplification of the initial photo-electrons. This delay is of the order of 20 ns. The pms introduce a jitter of ~0.5 ns.

Therefore, from the particle entering the scintillator to a signal emerging from the PM tube, there is an average delay of 25 ns with a standard deviation of around 2 ns.

Cables, 36.5 m long, connect the PM tubes to the logic itself and cause a delay of 157 ns. The signals from the pm tubes are sorted by NIM logic, and data is sent to the CTL indicating a hit in one or more of the 3 windows defined above. This data emerges from the logic after about 67 ns.

The total time from a particle leaving the interaction point, to a data signal arriving at the CTL is therefore around 3 bunch crossings. This is too fast! The other subdetectors send their data around the 20 bunch crossing mark, so our data is pipelined by a special unit (called a TGD) until it can be sent to the trigger logic simultaneously with other data from the same event.

Data is sent in the 3 time windows defined above only when there is a hit in both walls of scintillator within that time window. The background signal is indicative of proton beam halo and is used in the first level trigger as a veto. The Interaction signal can be used as a timing reference for other subdetectors and also to add to BEMC data to help in tagging (amongst other things) incompletely absorbed electron showers. See Section 5.6.3 for details of the rates of various ToF triggers.



Figure 3.6: *Logic diagram for ToF.*

# Chapter 4

# Early work

## 4.1 Introduction

Early tests were performed on the scintillator, photomultiplier tubes (pms) and base/amplifier chain, first separately and then on a fully assembled counter. Further tests were made on site in DESY on the complete ToF device.

## 4.2 Photomultiplier Tests

The pm tubes (Hammamatsu high-field pm tubes originally installed in the UA1 experiment-see Appendix C.1.9 for the numbers) were tested for their response and stability of signal using a photon source ($Cs^{137}$ activating a Sodium Iodide crystal) placed against the pm window and sealed in a light-tight box. No amplifier was used for this test. The depth of the output pulse from the pm when HV was applied was noted at two voltages: 2000 V and 2500 V.

All but 2 pms (AM 613 and AM 633) were found to be working acceptably.

| Tube numbers | Response at 2000 V | Response at 2500 V |
|---|---|---|
| All except those noted | 50-100 mV | 200-500mV |
| AM 633 | 1400 mV | Off scale |
| AM 613 initial* | 400 mV | 1400 mV |
| AM 613 final* | 80 mV | 300 mV |

Table 4.1: Pm output response.

* AM 613 began with this output level each time HV was applied and then settled to the lower value within a few (~5) seconds.



## 4.3 Amplifier and base tests

The pm base (a resistor chain) was tested by measuring the resistance of each link in the chain once the base was constructed. Once all resistances were within specification, the base was tested for voltage breakdown by applying 2500 V across the resistor chain. All bases passed the test.

## 4.4 Counter studies

When Hamburg were unable to build ToF, QMW studied Pilcher's thesis work and used it in the design of the counters ([14]). Certain further tests were performed to confirm his work and provide initial benchmark numbers for the beginning of the run.

### 4.4.1 Timing

Flight time within the scintillator was measured in one of the large inner ToF 0 counters. A pair of small scintillators were placed above and below the ToF counter being tested, to define a small region of that counter. The two small counters were used to trigger a QVt (in $t$ mode) start for cosmic rays passing through them.

A small delay was introduced to the signal from the ToF counter under test and the signal from that counter was used to stop the QVt. After enough events were collected, the trigger counters were moved to other positions on the sheet as shown in Figure 4.1.

The results are as follows:

| Point on diagram | Distance from pm tube (mm) | Time difference (ns) |
|---|---|---|
| A | 60 | 0 |
| B | 190 | 3.8 |
| C | 350 | 4.9 |

Table 4.2: Photon flight path timing difference within the scintillator

There is therefore a measured average difference of ~5 ns between particles passing near the pm tube and those in the corner of the counter. This measurement shows the timing difference caused by light transit time within the scintillator and is one of several sources which add to the resolution of ToF (see Section 6.4.3).

Figure 4.1: *Inner ToF 0 counter, showing positions of trigger counters (A to C) for timing tests. Refer to Table*

### 4.4.2 Plateauing

#### Efficiency of detection

Scintillation counters work by detecting the photons produced by the relaxation of electrons excited by the passage of charged particles through the scintillating material. The photons hit the sensitive area on the photomultiplier tube releasing photo-electrons which are accelerated through a high potential to a dynode. The potential difference between each dynode is a fixed fraction of the high voltage applied to the tube as a whole. Electrons hitting the dynode cause a shower of secondary electrons to be released. These are further accelerated by the next dynode in the chain. This multiplication continues through the dynode chain and a charge is collected at the output which is proportional to both the number of photo-electrons produced at the window of the pm and the voltage applied to the pm.

At low voltages the potential is insufficient to release electrons at the next dynode in the chain. As the voltage is raised, the ratio of secondary to incident electrons increases and an increasing charge is collected at the output. When the voltage is high enough, the number of photo-electrons reaching the next dynode in the chain ensures that, for a given number of primary photoelectrons the amount of charge collected at the output is constant. There is a region of voltages for which this constant ratio holds.



A counter running at such a voltage would show an output charge distribution similar to Figure 4.2. The broad peak in the centre (B) is produced by real hits within the scintillator. It is broad for several reasons. The charge is proportional to the number of incident photons. This number varies because of the quantum efficiency of the pm itself (not all incident photons produce photoelectrons), the path of the MIP, and the distance from the pm itself, as well as the natural statistical variation.

Noise (electronic or thermal, for example) can produce electrons at any one of the dynodes and these have their own output charge distribution (the exponentially falling part of the distribution on the left hand side of Figure 4.2). The dip (B), is the point at which the discriminator threshold should be set (see next paragraph).

At much lower voltages the peak (C) moves to the left and less events are above threshold. At higher voltages the noise peak moves to the right, and the gap (B) narrows or disappears altogether, and noise begins to dominate.

The peak voltage produced is proportional to the total charge from a signal. This allows the use of discriminators to accept as much of the true signals as possible while rejecting as much noise as possible. The efficiency of pm operation is dependent on both the voltage of the pm and the threshold value chosen. This was determined for ToF to be 100mV. If the pm voltage is raised above the peak operating voltage, output signals created by noise become large enough to fire the discriminator.

#### Measuring efficiency

The best operating voltage of a counter can be measured by a process called plateauing. This finds the lowest voltage which maximises the efficiency of detecting charged particles passing through the scintillator. The basic method for doing this is to use two small counters (A and B, say), kept at a fixed voltage, to define a small area on a third counter (the one which is being plateaued-C). The counters are set up so that particles passing through counters A and B should pass through counter C also.

A coincidence of counters A and B is used as a trigger to define a time window (of $\sim$20 ns) for the coincidence of all three counters. The ratio of triple counts (A,B and C) to double counts (A and B) was then plotted for several difference voltage values of counter C.

The efficiency was calculated at each voltage step, with efficiency defined as the ratio of triple coincidences to doubles coincidences. This rises to a maximum value which depends on the operating voltage of the trigger counters.

Initial results were:

| Voltage | Efficiency |
|---|---|
| 1400 | 48% |
| 1500 | 90% |
| 1600 | 96% |
| 1700 | 96% |

Table 4.3: Efficiency at various Voltages

Figure 4.2: *Typical distribution of charge from a photomultiplier tube.*



**Plateauing using triples**

The sheer number of triple coincidences can be used to give an indication of how efficiently the counter is operating. Using the plateauing set-up above, the counter is 'plateaued' by measuring the rate (i.e. number) of triples coincidences at several different voltages to find the optimum operating voltage. Plotting the number of triple coincidences against voltage produces a distinctive 'plateau' curve (See Figure 4.3). This shows an approximately linear rise (A) from a threshold voltage (B) to a 'knee' (C) above which is a flat plateau (D). At a higher voltage (E) the number of coincidences rises exponentially.

The threshold is the point at which the potential within the pm is strong enough to create sufficient secondary electrons to produce an output signal above the discriminator threshold. The initial rise shows the increasing proportion of pulses with high enough charge to fire the discriminator. The 'knee' and plateau are caused by the counter detecting all the 'real' signals which arrive at the pm window, so no increase in rate is seen. The final rise is caused by noise from within the pm itself beginning to dominate the output signal.

A voltage 100-200 V above the 'knee', somewhere in the plateau region is the region at which pm counters are typically run. The counter is operating efficiently, and noise is not yet a problem.

Figure 4.3: *Idealised plateau curve for a ToF counter.*

### 4.4.3 QVt tests

Measuring the charge produced from the pm it was possible to reconstruct the number of photo-electrons originally produced in the sensitive window of the pm.

The coincidence logic used to plateau the counter was used to generate a QVt start pulse. The charge was collected from the third counter at each trigger. The data was built up into a histogram showing a pedestal value (generated by noise in the QVt) plus the number of occurrences of a trigger with a particular charge.

The mean of a distribution can be approximated from its width. For an approximately Poisson distribution $\sigma$ has contributions from statistical and other sources (e.g. Landau width).

$$\mathrm{sd}^2 = \sigma^2 + \Sigma(\text{other sources}^2) \tag{4.1}$$

A Poisson distribution has $\sigma = \sqrt{n}$. Assuming the distribution to be Poisson we can calculate a lower limit to the number of photoelectrons arriving at the window of the pm.

$$\frac{sd}{mean} = \frac{1}{\sqrt{n}} \tag{4.2}$$

here

$$\frac{\sigma}{mean} = \frac{3.3}{20.3} = \frac{1}{\sqrt{38}} \tag{4.3}$$

So $n$ is 38. As described above this is a lower limit on $n$, with an error of $\pm$ 6 statistical, but an upper limit which depends on the other contributions to the width.

A different method of estimating the number of incident photo-electrons is to measure the mode charge (20) produced, and use a typical gain value ($2\times 10^5$). This gives $n$ a value of $\sim$200 $\pm$100, which is consistent with that found above.

## 4.5 Tests in Germany before running

Before assembly, the scintillator and pms were tested to find any damage which had occurred during transit. The pms were tested for light response using a Cobalt$^{60}$



source and Sodium Iodide crystal. Results were similar to the earlier light test, with AM613 and AM633 displaying the same oddities as in Section 4.2.

### 4.5.1 Rates

The rates at which individual ToF counters fire because of random pm noise affects the accidental coincidence rate and hence the number of unwanted vetoes. The rates were measured before ToF was installed.

#### Singles rate

The singles rates for each counter at plateau voltage were $\sim$20-50 Hz. This was from all sources.

#### Doubles rate

The coincidence of signals from particles passing through both walls of ToF will generate the primary trigger signals passed to the H1 central trigger (See Chapters 2 and 3). Therefore the rate of accidental triggers from single hits coinciding by chance is an important measure of inefficiency. The singles rate was much greater in actual running (See Section 4.6.7) and the same calculation was repeated for those conditions.

The doubles rates from random coincidences were calculated as follows:

Probability of a hit in one counter = rate $\times$ time window.

Probability of 2 hits in the same time window = (Probability for 1 hit)$^2$.

Rate of double hits (Hz) = Probability of 2 hits * number of time windows per second.

$P1 = 200 \times 2 \times 10^{-8} = 4 \times 10^{-6}$

$P2 = (4 \times 10^{-6})^2 = 1.6 \times 10^{-11}$

$N = 1.6 \times 10^{-11} \times 5 \times 10^7 = 8 \times 10^{-4}$

The calculated rate of accidental coincidences is $8\times 10^{-4}$ Hz. This is much lower than the actual doubles rate from cosmic rays of $\sim$2Hz and indicates that random coincidences are not a big problem and should cause a negligible number of false vetoes.

**Triples rate**

Counters were formed into triples by opening the ToF shutters and using the overlap of the inner counters as the other trigger counter. Plateau voltages were found for each counter in this way.

A rough approximation of the expected triples rate was made by estimating the solid angle ($\Omega$) through which a cosmic ray must pass in order to strike the three counters used to plateau a counter, and using this to estimate the rate given that the rate of vertical cosmic rays at ground level is $\sim$100 Hertz m$^{-2}$ steradian$^{-1}$ and the rate of cosmic rays is approximately proportional to $\cos^2\theta$ (where $\theta$ is the angle measured from the vertical). Only the centre of each counter fell within this cone so the area studied is only 0.01 $m^2$.

A typical estimate (for 000,003 and 101) gave :

solid angle ($\Omega$) = 0.1 steradians.

angle of incidence ($\theta$) = 50$^{\mathrm{o}}$

Vertical rate = $\sim$100 Hz m$^{-2}$

Size of counter = $0.01 m^2$

$$Rate = \Omega \times cos^2\theta \times 100 = 10 \times cos^2(50^{\mathrm{o}}) = 0.4Hz \tag{4.4}$$

All calculated paths gave results of $\sim$ 0.1 to 0.5 Hz.

The actual triples rate was ($\sim$0.2 Hz) at plateau voltage. This was in agreement with the calculated rate for doubles and shows that accidental coincidences were not a problem in using triples to plateau the counters of ToF.

## 4.5.2 Plateauing

Each counter was plateaued in turn using the method described in Section 4.4.2 to find an approximate plateau value. The trigger counters were other ToF counters using the open shutters to allow coincidence with an inner counter. This process was repeated using the approximate plateau values to find a more accurate plateau.

Rough plateau values for each counter had been determined by eye from the triples rates but plateau runs using this method were very time consuming to perform. It was found that doubles could be used to plateau a counter, as long as the counter kept at a fixed voltage was at a reasonable plateau voltage itself.



Using the triples plateau value for the fixed-voltage counter, the voltage of the plateauing counter was varied and the results plotted in Figure 4.4 - doubles rate vs voltage.

This shows similar features to the triples plateau diagram but the plateau area above the knee is much smaller or (in some cases) non- existent. The rise begins much more rapidly than in triples plateaus. This is caused by the increase in efficiency of detecting particles which pass through the edge of the scintillator as the voltage is increased. This is not seen so much in the triples as particles which just clip one counter are less likely to pass through both the other counters.

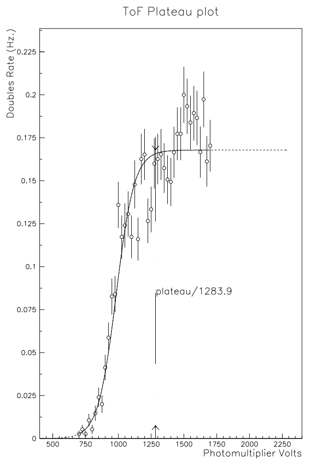


Figure 4.4: *Doubles vs triples rate for a ToF counter.*

The final plateau value was chosen by fitting the function given below, to the data and choosing a particular point of the function as the plateau value. The function was a combination of a linearly rising function added to a (1 + tanh) function. The (1+tanh) function required a 3 parameter fit but provided the linear rise and 'knee' part of the plateau.

$$X = P(1 + tanh((HV - t)/R) \tag{4.5}$$

P is the peak height (point at which 'knee' is reached).

t is the turn on point (voltage at 50% of the peak height).

R is the voltage range required to go from 12% to 88% of the peak height.

The linear function was simply $y = Mx + c$. The plateau voltage was defined as being 300V above the turn on point found by the fitting program.

Throughout the 2 run periods, doubles plateau curves were formed for each counter and the plateau voltage updated. This was done during periods of no beam. The process was automated and controlled from the MAC which ran the online monitoring of ToF rates. The counters were grouped in eights and these eight were plateaued simultaneously. Doubles rates were counted at 10 different voltages centering on the nominal voltage. A history of the plateau voltages for each counter are shown in Figures 4.5, 4.6, 4.7.

The counters operate at a lower gain (and hence efficiency) within the H1 main field. This required separate plateau voltages to be maintained for field on and field off conditions. The field-on conditions required higher plateau voltages. This is shown clearly in the history plots, where for each counter, the plateau voltages fall into two distinct groups, high for field-on conditions, low for field-off.

As the runs progressed, the scintillators became damaged by radiation from the beam and the scintillators were degraded in performance. This meant that the pms had to be run at a higher voltage to get the same efficiency. This is shown in the history plots with higher plateau voltages at later times.



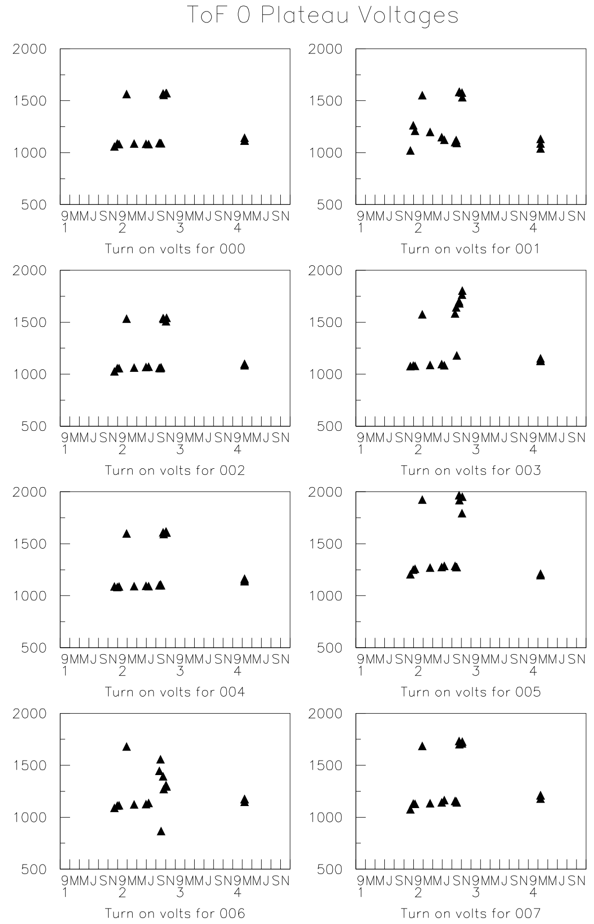


Figure 4.5: *History plots showing the change in plateau voltage for each counter in ToF 0 as time went on. The x-axis is labelled in months. Note the separation into field on (high) and field off (low) plateau voltages.*

## 4.6 ToF changes

### 4.6.1 Logic changes

The original method of forming coincidences (by the overlap of strobes) led to certain events having both a background and an interaction trigger after reconstruction, but only an interaction trigger at the central trigger logic.

In order to remove this ambiguity, the overlap coincidence logic was changed to edge triggered logic for the 1993 run, where the leading edge of a ToF counter pulse was used to define the time of the input to the strobe, and so could only exist in one of the two strobes (See Figure 4.8).

This allowed the strobes to be altered to maximize the efficiency of ToF.

### 4.6.2 Changes to ToF strobes

The position of the ToF trigger strobes greatly affects the efficiency of vetoing background and hence the deadtime of the experiment. During early running the strobes had yet to be optimized, and were changed several times for reasons explained below.

During early running the interaction (IA) strobe was set a few ns after the background (BG) strobe. The width was small (6-8 ns) initially, but once it became clear that the ToF interaction trigger element was present in a large fraction of low-$Q^2$ data, the IA strobe was widened. Information from the FTDCs showed that the low-$Q^2$ data struck ToF (especially ToF 1) earlier than the vast majority of ToF interaction triggers. The IA strobe was brought closer to the end of the BG strobe for this reason.

The BG strobe itself was initially set wide to catch very early background events. It was later decided that only the time region of the proton beam's passage through ToF should be vetoed.

The changes to strobe timings are given in Appendix C.1.6



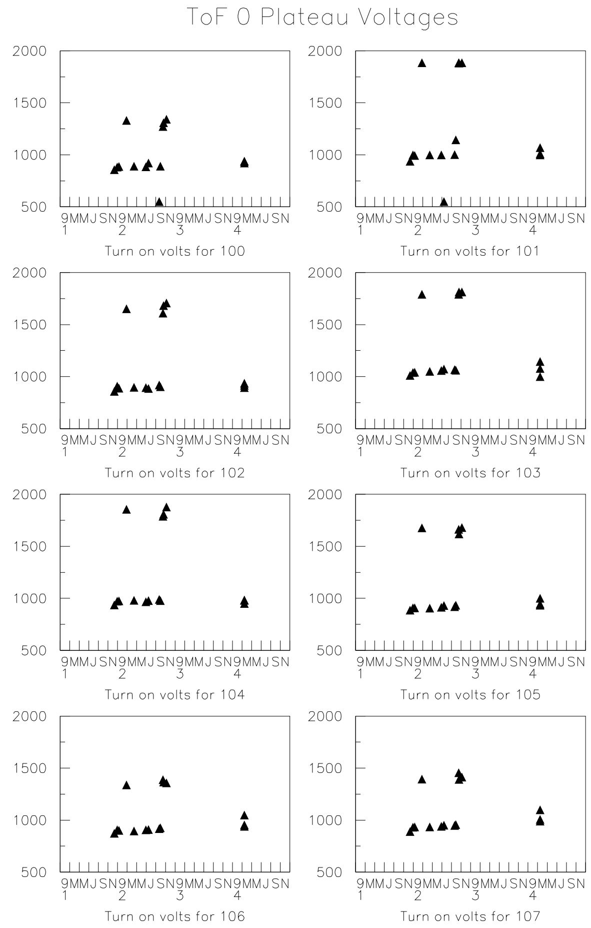


Figure 4.6: *History plots showing the change in plateau voltage for the first 8 counters in ToF 1 as time went on. The x-axis is labelled in months. Note the separation into field on (high) and field off (low) plateau voltages.*

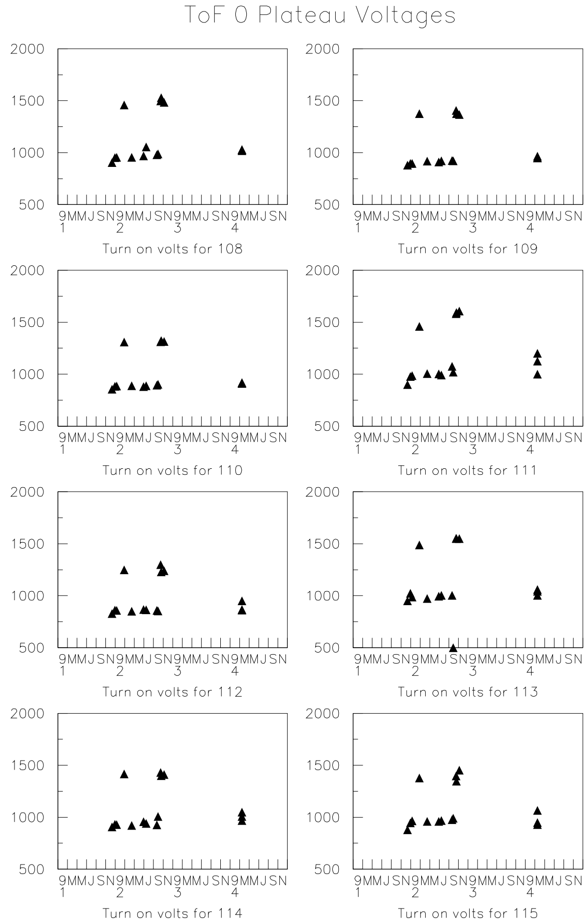


Figure 4.7: *History plots showing the change in plateau voltage for each counter in ToF 0 as time went on. The x-axis is labelled in months. Note the separation into field on (high) and field off (low) plateau voltages.*



Figure 4.8: *diagram showing how strobe overlap triggers ToF.*

### 4.6.3 Trigger changes

There were eight channels provided for ToF input into the level1 trigger. Later use of three more channels was provided for extra input. The three most important trigger elements were background, interaction and global and were always provided to CTL. The other channels provided various signals as defined in Appendices C.1.1 and C.1.3.

The length of the ToF BG trigger signal sent to the L1 trigger was changed to allow out of time triggers from other subdetectors to be vetoed, as defined in Appendix C.1.4.

For the 1993 running 6 bunch crossings were vetoed each time a veto signal was sent to the CTL. This led to a deadtime of 0.35% which is negligible compared to other sources of deadtime.

### 4.6.4 HV settings

Appendix C.1.9 shows the High Voltage settings adopted for running, both field on or field off.

### 4.6.5 Hardware changes

For the 1993 run period a lead shield was introduced around the beam pipe to reduce the amount of synchrotron radiation hitting ToF.

### 4.6.6 FTDC

Flash time to digital converters (FTDCs) were added to help analyse ToF hits offline to improve background rejection and aid the setting of strobe positions. Initially only the three coincidence trigger signals were sent to FTDCs from the central jet chamber. For the 1993 run, FTDCs were available for signals from each ToF counter as well as 8 trigger signals. See Appendix C.1.11 and chapter 5 for further information.

### 4.6.7 Rates

### 4.6.8 Lining up the counters

Each counter within a wall of ToF was 'timed in' with the other counters in that wall by measuring the peak of the proton beam distribution as recorded by the online TDCs.

The cable length within the logic and CAMAC readout was made identical for each counter. The peak of the proton beam online TDC distribution was then used to line up the counters within each wall. This process was completed by run 29670, whereupon all counters were within 0.25 ns of each other.

Further work on individual counter timing is covered in Chapter 7.

## 4.7 Rates Studies

An estimate of the spacial distribution of particles passing through ToF can be found from the decrease in singles rate as one ToF shutter is moved away from the beam pipe. The overall global trigger rate and singles rates from the internal counters of ToF were recorded with one shutter stationary and the other moved gradually in.

The rates and position are shown in table 4.5 and figure 4.9. The ratio of the rate recorded in the moving shutter to that recorded in the stationary shutter is used, in order to minimize fluctuations caused by any alteration in beam conditions.



| ToF Counter singles rates | IA rate | BG rate | GL rate | GL coinc |
|---|---|---|---|---|
| 000 | 1285 | 1908 | 3320 | 991 |
| 001 | 1835 | 3016 | 5310 | 1444 |
| 002 | 1146 | 1947 | 3191 | 967 |
| 003 | 3119 | 5571 | 9352 | 4398 |
| 004 | 2152 | 4905 | 7413 | 4078 |
| 005 | 984 | 1610 | 2669 | 1045 |
| 006 | 1239 | 2387 | 3897 | 1368 |
| 007 | 793 | 1666 | 2667 | 1086 |
| 100 | 542 | 795 | 1522 | |
| 101 | 458 | 1113 | 1641 | |
| 102 | 706 | 1340 | 2163 | |
| 103 | 242 | 484 | 801 | |
| 104 | 374 | 1100 | 1576 | |
| 105 | 1982 | 3382 | 5685 | |
| 106 | 1674 | 3253 | 4938 | |
| 107 | 685 | 1257 | 2067 | |
| 108 | 713 | 1448 | 2331 | |
| 109 | 1874 | 3177 | 5242 | |
| 110 | 1649 | 3447 | 5270 | |
| 111 | 1181 | 1796 | 3157 | |
| 112 | 494 | 742 | 1561 | |
| 113 | 639 | 1248 | 2034 | |
| 114 | 864 | 1379 | 2408 | |
| 115 | 521 | 724 | 1431 | |

Table 4.4: ToF singles rates

The plots all show an (almost) linear fall of rate with increasing distance from the beam pipe.

| ToF shutter position | | Global rate | T003 | T004 |
|---|---|---|---|---|
| +x (mm) | -x (mm) | (Hz) | (Hz) | (Hz) |
| Open 200 | Open 200 | 3229 | 3180 | 2717 |
| Closed 0 | Closed 0 | 3972 | 5450 | 4611 |
| 0 | 42 | 3896 | 4855 | 4613 |
| 0 | 110 | 3763 | 4105 | 4583 |
| 0 | 155 | 3721 | 3738 | 4595 |
| Open 200 | Open 200 | 3213 | 3170 | 2706 |
| Closed 0 | Closed 0 | 4000 | 5330 | 4560 |
| 38 | 0 | 3870 | 5376 | 4123 |
| 116 | 0 | 3783 | 5344 | 3448 |
| 154 | 0 | 3762 | 5352 | 3160 |

Table 4.5: *Rates as a function of ToF shutter position.*

The singles rates fall linearly from a maximum in the closed position to about 60% of their initial value when fully open. The ToF global trigger falls by only 10% (per shutter) for the same movement.

The ToF counters mounted on the shutter are inside the other ToF counters in their wall and so have some shielding provided by the lead mounted in that wall. This, coupled with the linear fall in singles rate with increasing distance from the beam pipe indicates one of two things:

- If the singles rate is from particles which are unable to penetrate more than one ToF counter (e.g. synchrotron radiation) then the linear increase in singles rate with decreasing distance (See Figure 4.10) indicates a constant spatial distribution. Assuming no hits from particles penetrating through the covered portion of ToF, the singles rate increases as more of the ToF counter is 'uncovered', and is directly proportional to the amount of ToF which is uncovered (i.e. inversely proportional to the distance from the beampipe).

- There is a linear increase in the number of penetrating particles with decreasing distance to the beampipe. This is reflected in the global trigger rate (See Figure 4.11), which increases linearly with decreasing distance and must be made up of penetrating particles (a coincidence of both walls is required by the ToF trigger logic).



The actual distribution is almost certainly a mixture of these two. The slight increase in ToF singles rates at $x=0$ may indicate a non-linear part of the distribution occurring inside and which is measurable just outside the beampipe, but ToF is physically unable to get close enough to determine this for certain.

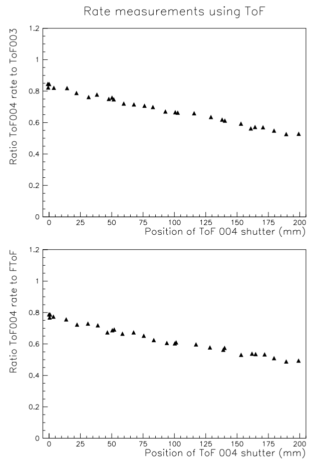


Figure 4.9: *Upper plot shows the ratio of the rate of the moving ToF 0 counter divided by that of the stationary ToF 0 counter against the position of the shutter. Lower plot shows similar ratio but comparing moving shutter with th FToF global rate.*

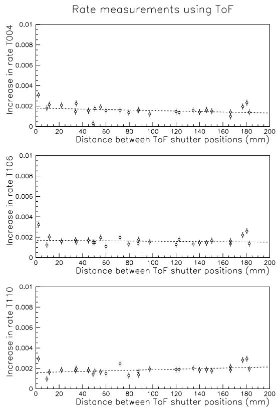


Figure 4.10: *Rate of change of singles rate against difference of ToF shutter positions for all three counters in the positive ToF shutter. The flat distribution is shown as positive and indicates a linear increase in rate with decreasing distance to the beampipe.*



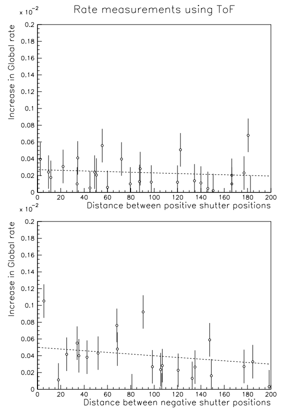


Figure 4.11: *Upper plot shows the change in the Global ToF trigger rate (divided by that of the stationary ToF 003 counter) against the difference in position of the moving positive shutter. Lower plot shows the change in trigger rate for the moving negative shutter.*

# Chapter 5

# Performance of ToF

## 5.1 Performance of ToF

Using data stored on an event by event basis, an offline study of the performance of ToF was made. Event data stored on magnetic tape and used in this analysis includes event data from individual ToF counters and the H1 trigger. The results of this analysis were very useful in determining event signatures in ToF and aided timing studies covered in later chapters.

This chapter gives a description and explanation of the performance of ToF by studying three sorts of data:

- Luminosity runs. Data was taken while colliding electron and proton beams were present in the machine. Physics data is a subset of luminosity data.

- Cosmic runs. Data was taken using cosmic rays to trigger the apparatus and no beams were present in the machine. ToF was used to trigger all the events studied in this sample.

- Monitor runs. Both beams were present, but only ToF data was read out. This data was used to generate 'calibration' data for ToF.

The use of ToF as a level 1 trigger to veto $\sim$99% of the total trigger rate meant that optimization of the trigger was a high priority. Data from hit multiplicity studies was combined with trigger information to study alternatives to the coincidence triggering which ToF was designed to use. Trigger and event rates were also studied.



## 5.2 Available Data and Relevant Read-out

For all run periods, ToF information was read out via the MWPC VME system and stored using the BOS data storage system [16]. A number of bunch crossings (referred to here as bc's) of data, centred on the nominal event bc are stored. This number was changed for different run periods (see Section 5.7.1 and Appendix C.1.7). A feature of the ToF readout means that bunch 0 is the latest bunch crossing, and the highest numbered bunch the earliest. Data from each strobed time window for each ToF counter was stored as well as copies of the trigger data sent to the CTL.

The ToF trigger elements are listed in Appendix C.1.1 .

ToF timing data (from TDC information) has been stored in a variety of BOS banks (Appendix C.1.11) and is covered fully in Chapter 6. However, typical timing distributions and a comparison of timing and trigger data will be shown here.

## 5.3 Proportion of ToF data

Event data accepted by the H1 trigger is stored on magnetic tape and called 'raw' data. This is processed to reconstruct extra data (such as particle tracks) not initially defined. Reconstructed data is kept on so-called POT tapes. The results of the final level of reconstruction (e.g. particle identification) are stored on DST tapes. So-called 'physics' data is a subset of the DST data, which is collected using offline software cuts to remove unwanted background events.

Raw data was used for most of this analysis, with any reconstruction being performed as necessary, as background events are removed in the final reconstruction process.

ToF data is present on a large fraction of most datasets, and is dependent on run conditions. Some subtriggers have a ToF trigger as one of their elements (See Appendix C.1.2). Table 5.1 shows a typical breakdown of ToF trigger elements present in various datasets. However, ToF data is present on 90-99% of the low-$Q^2$ physics data (selected by offline software cuts - see appendix D.1), but only 10-30% of the raw data (data stored directly on magnetic tape without any offline software cuts applied).

The 'errors' given for the raw, level 4 reject, and DST tapes are run-dependent variations caused by beam conditions. The errors given for the physics samples are

| Data Sample | ToF events | Background | Interaction | Global |
|---|---|---|---|---|
| Raw | 30%±5% | 6.9% | 10.0% | 14.7% |
| Level 4 reject | 24.2± 5% | 2.3± 1.5% | 19.3± 5% | 23.7 ±3% |
| DST | 17.7% | 1.1% | 14.9% | 16.9% |
| Physics ELAN | 98%±1% | 0.013%±0.007% | 75.1%±0.6% | 3.3%±0.1% |
| Physics etag | 90%±2% | 0.003%±0.002% | 65.4%±0.2% | 2.3%±0.3% |

Table 5.1: *Proportion of events with ToF information*

1-sigma statistical fluctuations.

## 5.4 ToF trigger data

Data from the three ToF triggers is available from three sources: the H1 central trigger data (CTL), the ToF local readout, and via reconstruction of the ToF counter data. A comparison of these three sources gives a measure of the efficiency of the ToF trigger. Both subtriggers and trigger elements were used in early studies, but the subtriggers were shown to be representative and form the basis of all results presented here.

The ToF triggers consist of:

- Interaction Triggers (IA). These events are triggered by a coincidence of the two ToF walls in the interaction time window. During most luminosity runs, the ToF interaction trigger was not used on its own, rather, it was present only as a trigger element in conjunction with other triggers which were used to study physics events.

- Background Triggers (BG). These events are triggered by a coincidence of the two ToF walls in the background time window. Most background events are vetoed at level 1, but a small proportion appear on the data tapes.

- Global triggers (GL). These events are triggered by a coincidence of the two ToF walls in the global time window. They should appear in conjunction with any IA or BG trigger.

- Single wall triggers. These occur when there is any hit within a wall of ToF. ToF 0 and ToF 1 have their own individual triggers.



Most ToF triggers are caused by background events, even if they do not generate a BG trigger. This is true of all subdetectors within H1, however. Careful offline analysis is required to find true physics events.

### 5.4.1 Interaction triggers

ToF interaction (IA) triggers have timing consistent with being from the physics interaction point, but are in fact mostly synchrotron radiation. IA triggers occur in a high proportion of physics events, especially Low-$Q^2$ events. Before the introduction of edge-triggered logic, events could be given both a background and interaction trigger. Appendix C.1.3 shows the run ranges during which the ToF IA subtrigger was used.

### 5.4.2 ToF background triggers

These events are almost exclusively proton background events. Most ToF background (BG) triggers were vetoed by the level 1 trigger, but there are three different ways a ToF BG event can appear on a data sample.

- ToF monitor triggers. These are used for background studies and use the ToF BG to trigger event but have a high prescale value (4096 for 1992 run). (See Section 2.11.1 for a definition of prescale value).

- 'Unvetoable' triggers. Certain subtriggers, by arrangement, did not have the ToF veto applied. Events triggered by these subtriggers may therefore have a ToF BG trigger. They are prescaled at the rate of the trigger which fired.

- Out of time triggers. These are caused by other (non-ToF) triggers firing outside the $t0$ bunch crossing. They have no ToF BG trigger element set in the event bc, but do have a BG trigger read out in a different bc. They occur mostly during the period when the ToF veto was only 3 bunch crossings wide.

ToF background monitor triggers make up only 0.25% to 1.0% of data on a POT tape, representing 1/10th of all BG data on the tape, with out of time triggers forming another 1/10th. The remaining BG events are all unvetoable triggers.

### 5.4.3 ToF global triggers

ToF global triggers (GL) occur in events where signals occur in counters in both walls of ToF within the same bunch crossing. The global trigger should be set if either (or both) an interaction or background trigger is present. For certain run periods the ToF global trigger was a monitor trigger (see Appendix C.1.2). Events which have a global ToF trigger, but neither a background or interaction trigger are almost exclusively background events from proton remnants which are no longer contained within a bunch.

### 5.4.4 Comparison of trigger information

The 3 sources of ToF trigger data (see Section 5.4) are local read-out (local), H1 central trigger (CTL) and offline reconstruction (reconstructed). By combining the data from these sources graphically in a so-called trigger matrix, an indication of the agreement between sources can be seen.

The matrices were used to find inconsistencies in the trigger data (from hardware faults) so that they could be removed or explained.

There are three trigger matrices, each displaying one of the three sources against another of the sources (see Figure 5.1):

- ToF trigger at CTL in the event bunch crossing against trigger recorded by MWPC readout (local).
- ToF trigger reconstructed in software against trigger recorded by MWPC read-out (local).
- ToF trigger at CTL in the nominal bunch crossing vs trigger reconstructed in software.

Data from each source is represented by the converted-bit number (from 0 to 7) defined in section 3.2.5; 1 representing an IA trigger, 2 a BG trigger and 4 a GL trigger. These numbers are additive, so an event with all triggers present is represented by a 7. Each matrix has the 0,0 point in the bottom left-hand corner.

Each event is entered as an element in the matrix, with the column and row corresponding to the data from that trigger source. Thus an event with a reconstructed



BG trigger (bit 2) and a local GL trigger (bit 4) would be row 2, column 4 of the second matrix.

Diagonal elements indicate agreement between data sources, off-diagonal elements indicate disagreement. The main reasons for disagreement between the sources are mistimed triggers, hardware failure or an artifact of the logic.

Figure 5.1 shows the three trigger matrices for typical luminosity data.

The top matrix shows the comparison of local and CTL data and the diagonal entries indicate very good agreement. Those events along the bottom of the matrix (CTL = 0, local not = 0) indicate that the ToF CTL trigger did not occur in the CTL $t0$ bc.

The central matrix shows the comparison of local trigger and reconstructed trigger. There are a set of events along the left hand side (local = 0, reconstructed not = 0) which indicate events which did not fire the ToF local trigger because the overlap of signals from each wall was insufficient to fire the coincidence trigger (see Section 3.2.5). This is a feature of the ToF logic. Timing data from these events confirms that this is indeed the reason, with the counter hit times widely spaced (rms separation of 10 ns or more - corresponding to the length of the logic pulses).

### 5.4.5 Agreement between counter data and triggers

The local readout data from triggers and counters was compared to see how efficiently the ToF hardware was working.

| Trigger | Events with CTL and reconstructed triggers |
|---|---|
| Reconstructed Global | 81.5% |
| CTL Global | 99.9% |
| Reconstructed Interaction | 86.3% |
| CTL Interaction | 99.9% |
| Reconstructed Background | 95% |
| CTL Background | 80.9% |

Table 5.2: *Comparison of the CTL and reconstructed data with the BRTE trigger data.*

As can be seen, most reconstructed global and interaction triggers have a similar reconstructed trigger. Background events sometimes have no CTL trigger, but reconstruct as background. These events have trigger times which are spread throughout the background strobe, indicating that such events are caused by inefficiencies

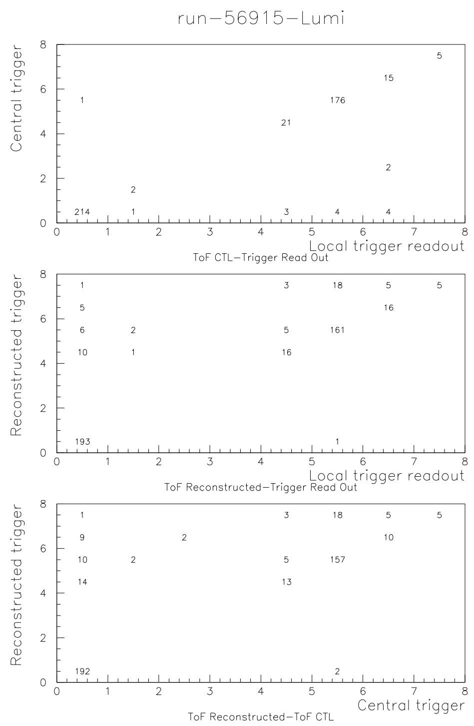


Figure 5.1: *Trigger matrices. Diagonal entries indicate good agreement.*



in sending the trigger information to the CTL, not an inefficiency in the forming of strobes.

## 5.5 Total proportion of triggers with ToF background data

So far, a claim has been made that ToF vetoes 99% of all triggers. Online studies indicate that ToF has a huge effect on the trigger rate (deadtime falls from ~100% to 10%) and offline studies have quantified the effect on various subtriggers, as explained below.

ToF information is present on almost all events which cause a level 1 trigger in H1 because of the large amount of background particles which trigger subdetectors despite not being interesting physics. These events often have a ToF background trigger present, and are vetoed.

A small proportion of these events are kept for monitoring purposes and from these an analysis of the subtrigger's 'trigger-quality' has been made. The trigger-quality is the proportion of that particular subtrigger's data which contains a ToF background trigger element.

This was performed in the following way, studying raw and Level 4 rejected events. It assumes that each event with a prescale factor $n$ (See Section 2.11.1) represents $n+1$ other events with identical trigger elements.

First, all subtriggers were reconstructed from their trigger elements. The lowest prescale factor of the actual subtrigger was used as the prescale factor ($n$) for that event. If no ToF BG trigger element was present, an event was considered to be $n+1$ non-background events for each reconstructed subtrigger in that event.

If an event contained a ToF BG subtrigger (reconstructed or actual), then it was considered to be $n+1$ background events for each reconstructed subtrigger firing in that event. From this each subtriggers' trigger-quality can be found (see table 5.3).

The important thing to notice in this table is that most triggers are almost ~100% background.

Subtriggers which are not represented here had no background events within the sample, but had relatively few (~1000) events as they were prescaled at a low value (usually 1).

| Subtrigger | Proportion BG | Subtrigger | Proportion BG |
|---|---|---|---|
| 10 - 11 | >99.9% | 96 - 98 | >99.9% |
| 21 | 88.1% | 99 | 98.2% |
| 22 | 92.3% | 101 -116 | >99.9% |
| 31 | 66.7% | 125 | 98.0% |
| 32 | >99.9% | 126 | 56.6% |
| 94 | 14.3% | 127 | >99.9% |

Table 5.3: *Trigger Quality for 93 POT data*

Exceptions to these are the tracking triggers (33 to 44) which have a high prescale and many events, but which have better vertex information and so less likelihood of containing a background event.

## 5.6 Analysis of ToF trigger data

### 5.6.1 Effect of the edge triggered logic

As mentioned in previous sections, the original ToF design had coincidence logic which used the overlap of signals from each wall as a trigger. As a result of the number of events labelled as both background and interaction, edge-triggered logic was installed and was in use after run 57887. Under this hardware scheme, any hit in one wall produces a signal of fixed length, labelled as either background or interaction. The coincidence of these signals forms the trigger improving the resolution of events near the strobes.

Table 5.4 shows the performance of ToF, before and after installation of the edge-triggered logic.

The edge-triggered logic cuts down the number of reconstructed events labelled as both background and interaction, giving good agreement between the central trigger and the reconstructed trigger.

The proportion of events which are reconstructed as background, but have no corresponding CTL BG trigger is also much smaller.

The sharpness of the strobes falls faster with the edge triggered logic, but can still be seen because of the method of FTDC (Flash Time to Digital Converters) reconstruction which is itself only accurate to $\pm$ 1 ns (See Section 6.2.1).



| Effect | Before ETL | After ETL |
|---|---|---|
| Proportion of CTL data labelled as both BG and IA | 2.3% | 0.2% |
| Proportion of reconstructed data labelled as both BG and IA | 12.5% | 0.2% |
| Proportion of reconstructed BG events missed by CTL | 59.5% | 17.9% |
| Time for strobe to fall to 0 | | |
| Trigger | 4-5ns | 2-3 ns |
| Individual counter | 3ns | 2ns |

Table 5.4: *Effect of the Edge-Triggered Logic on ToF trigger performance.*

### 5.6.2 Single wall triggering

When it was decided to build TOF, the exact singles background rates present in the detector were unknown, and it was decided that triggering via a coincidence between the two walls was the safest strategy. The singles rate measured to date has been fairly low (see Section 4.6.7) and the results of using singles hits to veto H1 events are covered below.

Using 'physics' events chosen via software cuts developed by the ELAN group (See Appendix D.1 and [17]), the effect of various single-wall trigger schemes was checked. This was done by finding the proportion of physics events which would be lost if a particular trigger scheme was in use.

The schemes considered and the effects on POT and physics datasets are given in table 5.5. The 1992 physics cuts were not optimised at this time, and the calculated percentage loss is therefore too high, but gives a strong indication of which cuts are most effective.

| Veto condition | POT events removed | physics data removed |
|---|---|---|
| 1 No BG hit in any wall | 53.4% | 42.3% |
| 2 No BG hit in ToF 1 | 47.4% | 37.3% |
| 3 Number ToF 1 BG $\leq$ ToF 1 IA | 42.4% | 11.1% |
| 4 Any ToF 1 IA | 27.7% | 13.7% |
| 3 and 4 | 56.5% | 2.5% |

Table 5.5: *Percentage of dataset containing ToF events which does not pass the veto condition and is therefore removed.*

Appendix C.1.3 shows the vetoing levels added for the 1993 run. These were used in conjunction with certain triggers (eg BEMC single electron trigger (BSET) subtriggers 3-5)to cut down the amount of background.

### 5.6.3 Trigger Rates

Typical trigger rates for the ToF triggers are given below in table 5.6. The online rates are taken from the monitor program during typical 1994 running conditions. The offline rates are calculated from offline data using POT and Level 4 reject data counting each event with a trigger of the correct sort as $n+1$ events, where $n$ is the prescale factor of that event. The offline rate is lower than the online rate because of deadtime in the trigger, and the high number of background events which are rejected and never get onto data tapes. The acceptance rate is the rate at which ToF events were accepted onto the offline data tapes, taken from DST tapes.

| Trigger | Online (Hz) | Offline (Hz) | Acceptance Rate (Hz) |
|---|---|---|---|
| Interaction | 3600 | 3000 | 0.8 |
| Background | 5500 | 4700 | 0.1 |
| Global | 8500 | 7800 | 0.95 |

Table 5.6: *Measured rates for the ToF trigger elements.*

## 5.7 Analysis of ToF local Readout

Offline data from ToF was first used to optimise the readout, and then to study the performance of ToF. Results from this analysis are used in later chapters.

### 5.7.1 Bunch crossing of data

The ToF local readout was stored in a pipeline of 32 consecutive bunch crossings (bc's). When the H1 CTL sent a trigger signal, this data was read out and stored permanently on data tapes. Once initial testing was complete only 10 bunches were read out (the $t0$ bc, 3 before it and 6 after it). A feature of the readout meant that bunch 0 was *after* bunch 1, with bunch 31 being the first bunch.

The timing of the readout was tuned until ToF data fell almost exclusively into one bunch crossing, relative to the CTL $t0$ bunch crossing. This nominal event bc



varied according to the run period; for the 1992 run it was bc 22, for the 1993 run it was bc 7.

Triggers from other subdetectors with a mis-timed $t0$ caused ToF information to appear in other bc's.

A typical bunch crossing distribution is shown in Figure 5.2.

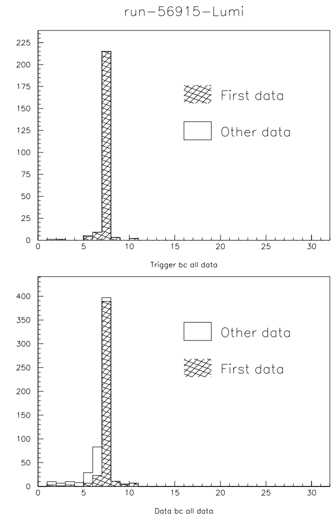


Figure 5.2: *Bunch crossing for data and trigger. Luminosity data.*

### 5.7.2 Event Hit Multiplicity in ToF

Event hit multiplicity represents an important secondary source of information on event type. By considering the hit distributions in both ToF 0 and ToF 1, as well as total hit multiplicity, background and interaction events could be distinguished, although not on an event by event basis.

#### Hit multiplicity in ToF Walls

Figure 5.3 shows the total event hit multiplicity for a monitor run (54665).Those events with a BG trigger are darkly shaded. Note the difference between BG and non-BG events. BG events have a mean multiplicity of 8, an initially flat distribution, and a slowly falling tail. Other events have a mean multiplicity of 5 and falls from an initial peak of 2 counters firing to virtually nothing at 10 counters firing.

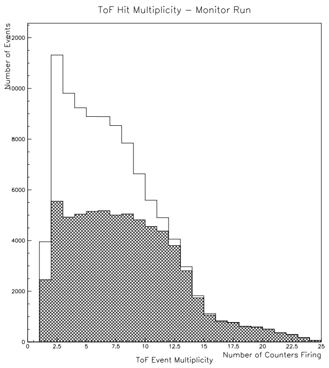


Figure 5.3: *Upper plot: number of channels firing. The large amount of background events are shown as shaded. Note that almost all high multiplicity events are background.*

### Hit rate per counter

Figure 5.4 shows the proportion of events with any ToF data, in which a particular counter fires. The inner counters have a much higher proportion of hits, although this is most pronounced in the IA and BG distributions. This is a result of the higher flux of particles near the beampipe as the bunches pass through ToF.

Those counters situated on the negative $x$ side of H1 (on the outside of the beam line) show a higher flux for both IA and BG triggers because losses from both beams occur preferentially on the outside of the ring.

In later luminosity runs the relative height of the central counter peaks is lower, caused by the inclusion of extra lead shielding around the beam pipe.

## 5.7.3 Bunch ID plots

Figure 5.5 shows the distribution of events within the bunches.

For the Autumn 92 run this was 9 on 9 bunches, with 1 electron and 1 proton pilot bunch. The trigger composition of each bunch is also shown. For interacting bunches about 50% of events have an interaction trigger element and about 20%



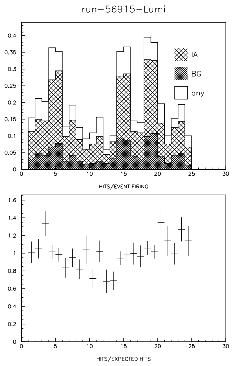


Figure 5.4: *Pattern plots. Upper plot: fraction of events with ToF data in that counter. Lower plot shows hits vs expected hits.*

have a background trigger element and the rest have neither. About 40% of the events in the proton pilot bunch have a background trigger, and only 10% have an interaction trigger.

In the Summer '93 data, up to 90 on 90 bunches were used, and very few background event have been taken through unvetoable triggers.

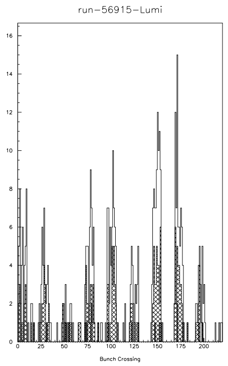


Figure 5.5: *Bunch crossing of data. For this run 90 bunches of each type were in the machine.*

## 5.8 Timing information

The timing information is provided by FTDCs which digitise a stretched version of ToF NIM pulses. These are reconstructed to give the start time of the pulse (See Chapter 6). For early runs, only the trigger channels had such information readout, but all counters were readout individually for the 1993 run.

### 5.8.1 Reconstructed FADC times

Figures 5.6 shows the reconstructed time of the ToF global trigger. The background and interaction peaks can be clearly seen. Events with background (BG with dark shading) or interaction (IA with lighter shading) trigger elements are highlighted. The timing has been correlated to the nominal event $t0$. The unshaded area between the peaks is caused by the inefficiency at the start and end of the trigger strobes.

Events with a BG trigger element have reconstructed times between -34. and -7. Events with an IA trigger have reconstructed times between -7. and 18. This compares with widths measured from a projection of the plot of 22 and 23ns respectively. The greater spread is caused by the ToF hardware (see below).

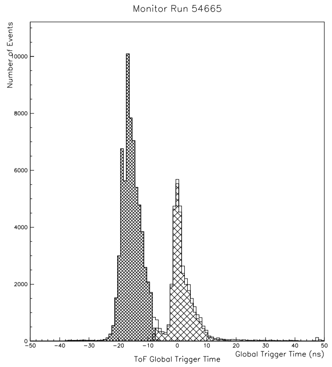


Figure 5.6: *ToF Monitor run Global Trigger event time. Darkly shaded events have a BG trigger, lightly shaded ones an IA trigger.*



### 5.8.2 Comparison of trigger times

The two timing scatter plots (Figure 5.7) show the relative timing of the ToF 0 global OR against the ToF 1 global OR and the timing of the IA or BG trigger vs the global trigger.

The first of these has a central 'fuzzy' area which shows the time difference between hits in the two walls of ToF. The second of these has a straight line, indicating that the global trigger and IA/BG trigger are firing together. The small horizontal lines which deviate from this occur because of the nature of the trigger hardware. Signals produced by events which have a global time a few nanoseconds before the start of one of the other trigger strobes are still active when the trigger (IA or BG) strobe becomes sensitive. The resulting (IA or BG) trigger time for all these events is the time of the start of that strobe. This is seen most clearly in the cosmic data.

Both plots of figure 5.7 have large areas which are lightly shaded. These represent events which have a hit in a ToF wall in a beam crossing following that of the trigger. Such events are not associated with a particular bunch and have a fairly flat timing spectrum.

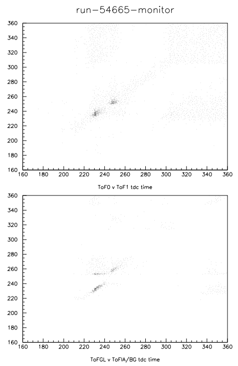


Figure 5.7: *Relative timing. Luminosity data.*

## 5.9 Conclusions

Initial studies of ToF trigger and counter data showed that a gross separation of background events from interaction was possible using multiplicity and timing. It was also useful in identifying areas where further work was needed. These included: labelling events with IA and BG triggers as one or the other; FTDC information was needed from individual counters to aid in background discrimination. Also, any errors which occurred during running were quickly identified by use of such information.



# Chapter 6

# Analysis of offline FTDC information

## 6.1 Reconstruction of the offline FTDC data

The timing data from the ToF flash-analog-to-digital converters (FADCs called thus FTDCs in this thesis) contains information helpful to the separation of background from interaction particles and is vital for monitoring the position of the relevant strobes. Resolution and flight time between the walls of ToF have been measured. Comparison of ToF TDC data with ToF trigger and counter read out information gives insights into the efficiency of the ToF triggers.

Data from several periods was studied, from Autumn '92 until summer '94. For 1992 (which was split into 6 FTDC periods) the coincidence trigger channels and Global OR channels had FTDC information available. In 1993 (split into 10 periods), timing signals were provided for the ToF coincidence triggers, the ToF 0 and ToF 1 global ORs and for each individual ToF counter. Full details of the data available are given in Appendix C.1.11.

## 6.2 Initial Studies

Early FTDC studies showed a fault in the online reconstruction. This had to be corrected before further studies could be undertaken.

### 6.2.1 Hardware

The ToF FTDCs are located in the central tracking area, and underwent several changes in number and location (see Appendix C.1.11). The FTDCs work by integrating the input signal and then sampling its leading edge. The samples are taken every 9.6 ns (1/10th of a bunch crossing and also known as 1 FTDC clock pulse) using an 8-bit flash ADC and stored for later reconstruction. The start time ($t0$) of the input pulse is found from the stored charges, by extrapolating the time when the charge was zero.

The FTDCs were designed for use with the drift chamber, and used a linear online reconstruction algorithm. The first two stored charges were used to extrapolate the event $t0$ with an accuracy of ~100 psecs [19].

The discriminated NIM output pulses from the TOF logic (Section 3.2.5) sent to the FTDCs were too short and show a full (and non-linear) 'charging capacitor' shape (see Figure 6.1). This caused a problem in the reconstruction (see Section 6.2.2). Hardware constraints made it impractical to lengthen the input signals, so a separate reconstruction algorithm was developed by the author, for which an accuracy of ±1.0 ns is quoted.

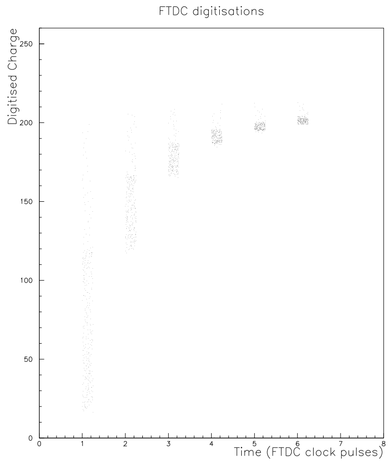


Figure 6.1: *Digitized charge stored by FTDC for the six FTDC clock pulses after signal start time. Note the distinctive charging capacitor shape.*



### 6.2.2 Initial findings

Initial findings indicated that the ToF strobes were set as expected and background events were earlier than interaction events. Further study showed that period five data (the first with any significant amount of FTDC data) had narrow peaks in the TDC structure, repeated every 9.6 ns. (See Figure 6.2). This was an artifact of the online algorithm which reconstructed the same start time for a wide range of input pulse amplitudes. This is shown in Figure 6.3. A method has been developed to recover a usable time from the digitized pulses. This has been used to analyse the data from period 5 onwards.

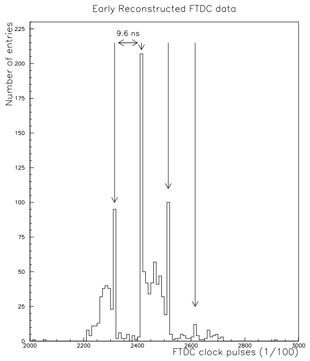


Figure 6.2: *ToF FTDC time distribution calculated using the online Qt algorithm clearly showing the peaked structure.*

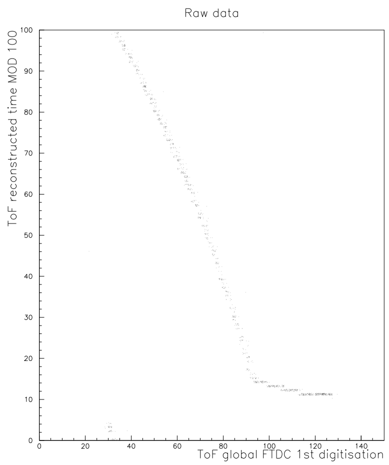


Figure 6.3: *Pulse start time reconstructed by Qt (in 1/100ths of an FADC clock) against 1st charge above pedestal for ToF global FTDC. Note the large range of charges (90 to 130) which gave a similar time (10 - 14).*



## 6.3 Recovering TDC data from later runs

The aim of this process is to provide a general reconstruction algorithm in which channel dependent parameters would be used to reconstruct a start time from the stored FTDC charges. To do this a general function describing the start time of a charging capacitor from charge accumulated at given times was used to generate parameters for each FTDC channel, as follows:

The equation describing a charging capacitor is [18]:

$$\frac{dQ}{dt} = \frac{-Q}{RC} \tag{6.1}$$

where Q is the charge on the capacitor, and RC is the time constant of the capacitor. This can be rearranged to give the charge at a fixed time in the future from the charge at time $t0$. Similarly, one can calculate the time at which the charge was 0 (ie the pulse start time) from the other (later) charges.

### 6.3.1 Finding the General Algorithm

The function describing a charging capacitor can be rearranged in terms of a start time $t0$, a maximum charge $A$ and a decay constant $\tau$:

$$D(i) = D(0) + A(1 - e^{-(t_i - t_0)/\tau}) \tag{6.2}$$

where $D(0)$ is the charge at $t_0$, $D(i)$ the charge at time $t_i$. For charges separated by a time $DT$ this becomes:

$$D(i+1) = D(0) + A(1 - e^{-((t_i + DT) - t_0)/\tau}) \tag{6.3}$$

For the first sample (ie setting $i$=0) we have:

$$D(1) = D(0) + A(1 - e^{-DT/\tau}) \tag{6.4}$$

To calculate A we must use Equation 6.2. This can be expressed as:

$$A \times e^{-(t_i - t_0)/\tau} = A + D(0) - D(i) \tag{6.5}$$

Subtracting D(i) (from Equation 6.2) D(i+1) (from equation 6.3):

$$D(i+1) - D(i) = A \times e^{-(t_i - t_0)/\tau} \times (1 - e^{-(DT/\tau)}) \tag{6.6}$$

Putting Equation 6.5 into Equation 6.6 we have:

$$D(i+1) - D(i) = (A + D(0) - D(i)) \times (1 - e^{-(DT/\tau)}) \tag{6.7}$$

This function describes the relationship of one charge to the previous one and allows calculation of the starting point of the charge. That is, the parameters of the function for a given capacitor are fixed and therefore if they are known, the start time can be generated from one or more of the stored charges.

The solution of this function is universal, monotonic and linear and produces a plot similar to Figure 6.4 with a slope determined by $\tau$.

$$Slope = -(1 - e^{-DT/\tau}) \tag{6.8}$$

Rearranging we have:

$$\tau = -DT/Ln(1 - slope) \tag{6.9}$$

From Equation 6.7 the intercept of x=0 on Figure 6.4 (D(1)-D(0)) is just

$$intercept = (A + D(0)) * slope \tag{6.10}$$

which gives us the parameter $A + D(0)$, referred to from now on as $A$.

A plot of $Q_i$ against $Q_{i+1} - Q_i$ for the FTDC data shows this straight line (Figure 6.4) describing the relationship of one charge to the previous charge. The parameters of the universal curve (Figure 6.4) were calculated from graphs such as these for each of the ToF FTDC channels.



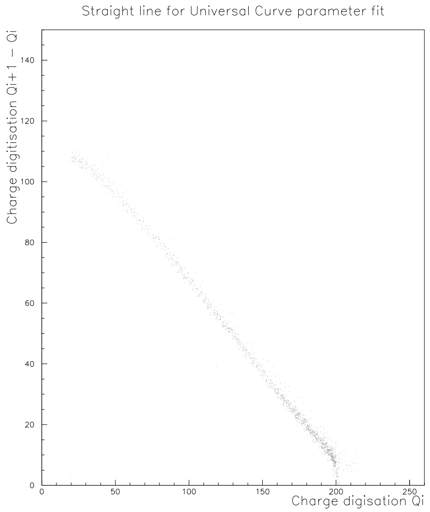


Figure 6.4: *Comparison of FTDC digitised charge with next digitised charge for each event. The slope of the linear part of the plot allows calculation of the $\tau$ parameter, the intercept with x=0 or y=0 allows calculation of the A parameter.*

### 6.3.2 Reconstructing the start time

With the parameters available, hit times were reconstructed for each counter in each event. The intial method of reconstruction was inadequate, and a so revised method was developed.

#### Initial method

Parameters $A$ and $\tau$ were calculated for each channel in each run period. A pulse start time was reconstructed for the first hit in a ToF FTDC channel for each event. The reconstruction equation used was:

$$t0 = ((10 * clockpulse) + 10.0 + (\tau * ln(1 - Diff))) * 0.96 \tag{6.11}$$

where

$$Diff = (FTDCcharge1 - pedestal/(A - pedestal))$$

The second (and third and fourth) charges could, in principle, have been included. However, the range of charge that these cover is small compared to that of the first charge and the accuracy gained from including these charges is minimal.

The time spectra produced using this equation had 1 to 1.5 ns gaps present in it, caused by an erroneous pedestal value (too low), an artifact of the FTDC operation. In addition, although the straight line fit describes the majority of data, the lowest values (Q<20) of the first charge indicate that the initial part of the charging capacitor shape has a slower rate of charging. Therefore the maximum charge reached in the first FTDC clock pulse is less than that calculated from the parameters. Therefore a refined method was developed, covered below.

#### Refined method

This method rescaled the first FTDC charge to lie between 0 and a maximum value MaxQ. The parameter A is rescaled to $A_{maxQ}$so that MaxQ represents a time of 1 FTDC clock pulse. This removed the 1 ns gap present in the initial reconstruction. $A$ (as opposed to $\tau$) is varied because it is within the log term.

This new method requires three parameters ($A_{MaxQ}, \tau$ and Qmin) for each channel, but only two pieces of data (first digitisation and FTDC clock start time) and gives the time for a hit in ToF as:



$$((100 * starttime) + 10 * (10.0 + \tau * ln(1 - frac))) * 0.096 \tag{6.12}$$

$$frac = (FTDCcharge1 - Qmin)/A_{maxQ}$$

This method, in fact, is easy to apply at level 4 and gives an accuracy of $\pm 0.5$ ns.

A second problem was present for period 5 and 6 data. Space limitations in the ToF logic meant hardware constraints caused the digitised charges to rise to a maximum at digitisation 3 and fall for later digitisations.

The same method was used to reconstruct these channels, but the fitting of a universal curve was more prone to error, as only the first three charge digitisations appeared on the plot used to determine the parameters. Small spikes and 0.5 ns gaps remain in the data for these channels, even after several different parameterisations.

The parameters were used to produce some plots of cosmic data. The peaked structure had disappeared and the distribution was flat, as expected. (See Figure 6.5). The gap at 290-295 ns is caused by the global time window being 5ns shorter than one HERA clock cycle. The peak at 296 ns is a feature of the hardware, where pulses of finite length, produced in the logic during the 5 ns where the global strobe was inactive, cause triggers as soon as the strobe becomes active once more.

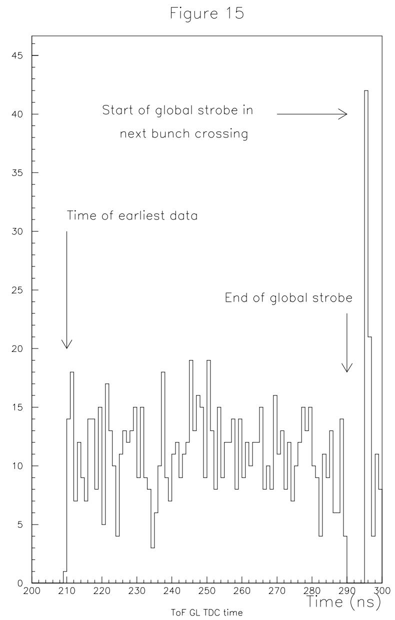


Figure 6.5: *ToF global coincidence timing reconstructed from new FTDC parameters. Distribution is flat.*

## 6.4 Analysis of reconstructed TDC information

The FTDC data was used to check the position of the ToF strobes. The trigger and individual counter information was combined with reconstructed FTDC times to measure efficiencies, resolution and the fall in efficiency at the end of the background strobe (See Section 6.4.2). Comparison of physics events with synchrotron events, showed a consistent difference in peak position, indicating that an offline discrimination of physics and background events can be made. Finally a discrepancy in FTDC results was explained (See Section 6.5).

Several test runs were made whilst preparing for luminosity in the summer 93 run. These runs were used by the author to find new parameters for the FTDC's and to measure strobe efficiencies and positions. Both cosmic and proton beam data was taken. The widths of the strobes were measured using cosmic runs. A full list of changes is given in Appendix C.1.6. A change in the H1 timing caused the proton



peak to temporarily straddle the point at which the background strobe ends and the interaction strobe starts. The fall in efficiency was again measured, confirming the earlier results.

### 6.4.1 Aligning the FTDC channel timings

For early 1992 running, the convention was to align the counters to the peak position of the proton distribution, both online and offline, because physics data and interaction data was had insufficiently defined peaks. Gaussian curves were fitted to the proton distributions, and the peaks were aligned. A scatter plot of channel time against the global time was used to measure the relative offset of each channel. The measured corrections were included in offline calculations.

Once physics data was available, a different standard was applied :the proton peaks had insufficient data in them because almost all background events were vetoed. For run data from '93 and after, the physics peak (as defined by the ELAN cuts) was used as the ToF-$t0$ of an event. All counters were lined up such that the peak of the data centred on zero. In instances where this was not practical (such as the background trigger FTDC) the zero point was extrapolated from other data.

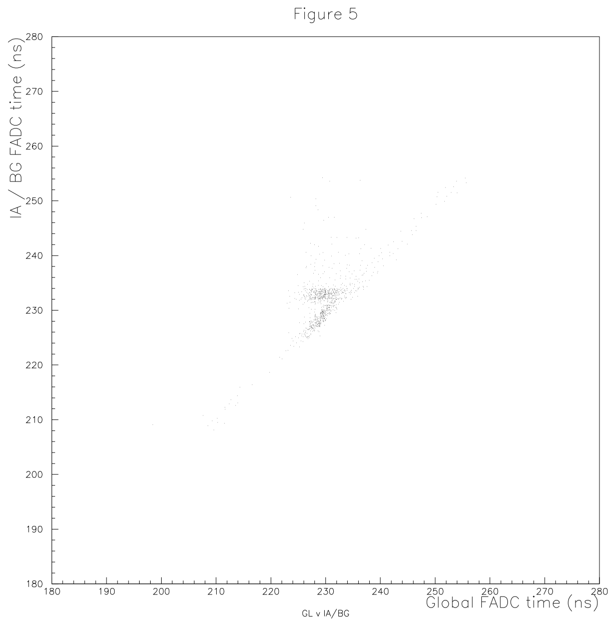


Figure 6.6: *Plot showing time calculated by new Qt aligned to make global, interaction and background times equal. Data from proton only test run in early summer 93 with proton peak straddling both time windows. The horizontal line represents interaction events with the correct global trigger time, but earliest possible interaction time.cf Peak in Figure 6.5 at 295 ns.*



### 6.4.2 Strobe settings and Efficiency

A measurement of the separation of the background (BG) and interaction (IA) strobes was vital to the calculation of ToF efficiency. For runs after the Summer of '93, the offline FTDC trigger plots were used to measure this. Previously, the online TDC trigger plots were used.

The comparison of FTDC information with trigger information also gives a measure of strobe efficiency. Plotting those events with a background trigger bit on the global FTDC trigger plot we have a direct measurement of the fall off of efficiency towards the end of the background trigger. For run period 2, when strobes were not optimised, a measurement was made (Figure 6.7). The left hand peak is small because of the large (4096) prescale applied to the ToF BG trigger.

The fall in efficiency is shown in Figures 6.8 & 6.9. It falls from 100% to 0% in 2 ns. This is combined with the width of the proton and electron peaks to give an estimate of those background events which are wrongly labelled as interaction. See Section 7.3.

A second source of inefficiency is caused by the operation of the ToF scintillators. Particles exiting the scintillator late in the background strobe produce a narrow output pulse from the strobed coincidence unit in the ToF logic (see Section 3.2.5). These pulses register in the MWPC readout of each individual channel, but are too narrow to register at the level 1 trigger.

Cosmic runs give the best measure of this inefficiency as they have a flat timing distribution and showed that: 3% of the events with reconstructed BG triggers do not have a BG trigger element and 20% of these (0.6% of the BG triggers) are at the end of the background strobe, while the remainder are at the start. Therefore the effect of the inefficiency at the end of the strobe is small, and furthermore for luminosity runs occurs in the trough between the electron and proton peaks where relatively few events occur.

The effect no longer occurs with the new edge triggered logic which was installed for the 1994 run.

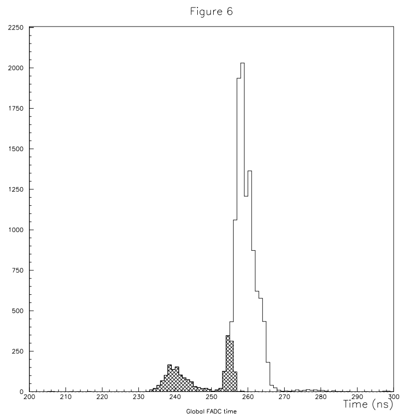


Figure 6.7: *ToF Global trigger times as calculated by online Qt from period 2 data. Events with a background trigger element set are shaded.*

### 6.4.3 Resolution

The resolution of ToF was measured by subtracting the ToF1 global OR time from the ToF0 global OR time, on an event by event basis. This was done separately for events both with and without BG triggers, fitting a Gaussian shape to the central peak of the distribution. The results are shown in Figure 6.10.

Luminosity data shows events with a BG trigger have a resolution with a sigma of 2.0 ns, while those with an IA trigger have a resolution with a sigma of 2.8 ns. The decrease in resolution for IA events is caused by contamination by late proton background particles. The resolution from monitor run data has a sigma 2.0 ns for both peaks. Pilot bunch data from the monitor run, without contamination, shows a difference of 1.44 ns in the mean position of the peaks. The difference in the means of the distributions results from the delay to the background strobe of ToF 0 in order to compensate for the 1.5 ns flight time between ToF 0 and ToF 1. Those events from particles travelling with the protons have a mean near -1.5. Those travelling with the electrons beam should have a mean near zero. The measured flight time difference between background and interaction particles is only 1.0 ns, however. This is thought be caused by late proton associated particles which contaminate the interaction events.



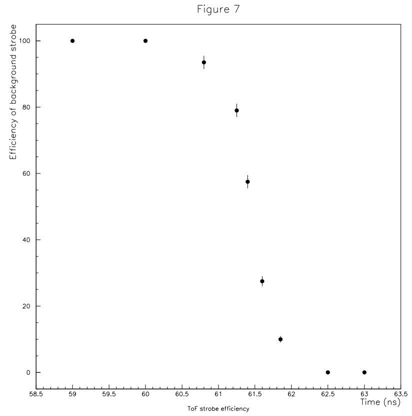


Figure 6.8: *Fall in efficiency of the background strobe, from online data.*

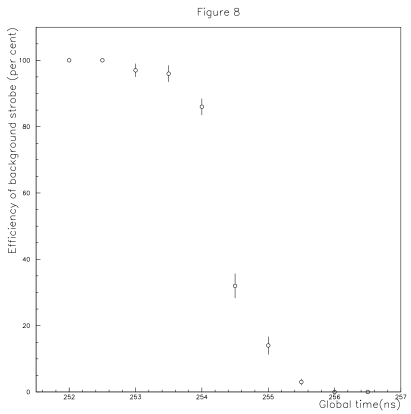


Figure 6.9: *Fall in efficiency of the background strobe, caused by logic overlap problems, offline data.*

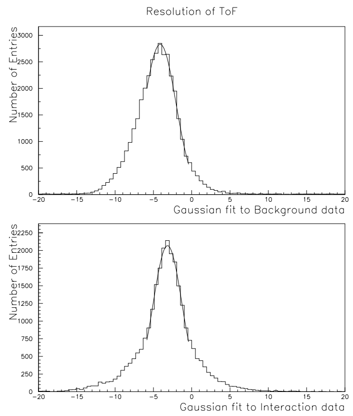


Figure 6.10: *Resolution of ToF from the monitor run. Upper plot is for data with a background trigger, the lower plot for data with an interaction trigger. Difference between the peak positions is 1.0 ns. Sigma for background data is 1.9 ns, and 2.1 ns for interaction data.*

### 6.4.4 Trigger channels

The three sources of ToF FTDC trigger data were compared in order to measure the inefficiency in forming the L1 ToF veto and the efficiency of the FTDCs. The data for each trigger channel was compared with the trigger element data reaching the CTL see table 6.1. For the global trigger channels, the FTDC peak separation was also noted. See Figures 6.11 through to 6.13.

| Trigger channel | FTDC + L1 | FTDC alone | L1 alone |
|---|---|---|---|
| ToF Interaction | 55503 | 61 | 300 |
| ToF Background | 65398 | 113 | 275 |
| ToF Global | 97896 | 198 | 925 |
| Interaction | | 0.11% | 0.54% |
| ToF Background | | 0.17% | 0.42% |
| ToF Global | | 0.22% | 1.93% |

Table 6.1: *Comparison of information from FTDCs with that from CTL*

The table shows the difference between what is received at the level 1 trigger and what reaches the FTDC. A good agreement exists between the CTL and FTDC results with the discrepancy caused by out of time triggers.



Figure 6.11 shows the ToF triggers which require a coincidence between the walls of ToF. The spike at the beginning of the ToF interaction trigger data is caused by events which occur in the background window late enough that they still have a signal present when the interaction window begins. Comparing the global and interaction trigger times for such events (Figure 6.13) shows this difference clearly.

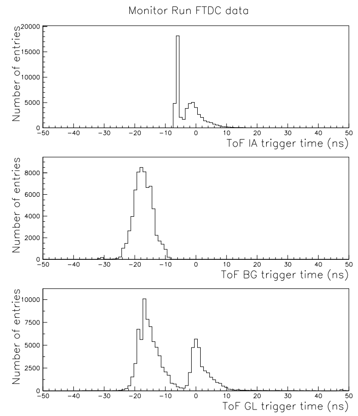


Figure 6.11: *ToF trigger FTDC timing distributions for a monitor run, without the veto applied. The top plot shows the timing of the interaction trigger, the middle plot shows the that of the background trigger and the bottom plot shows that of the global trigger.*

### 6.4.5 Individual counter channels

Individual counter FTDCs provided the most useful analysis data. Earliest and average event times were studied, and a comparison was made with FTDC trigger times. The results were used to calculate the likelihood of events being background or interaction (See Section 7.4).

In the monitor run data (see Figure 6.14), the relative heights of the interaction and background peaks show that the inner counters receive the bulk of the electron-associated hits, whereas the proton background is more evenly spread, as described in Section 5.7.2.

In the FTDC distributions of the outer counters, no electron peak is discernible. The inner counters, especially ToF 003, have pronounced interaction peaks. The interaction peak of ToF 003 is mirrored in the ToF global FTDC distribution, with relatively early hits in the ToF 003 interaction window defining the time of the ToF 0 OR signal. When this is ANDed with the (earlier) ToF 1 OR signal, the ToF 003 time defines the ToF global trigger time.

Such events are thought to be caused by prompt (direct) particles from the interaction point striking ToF 003 in such a position that the photons travel directly into the pm tube and so arrive early.

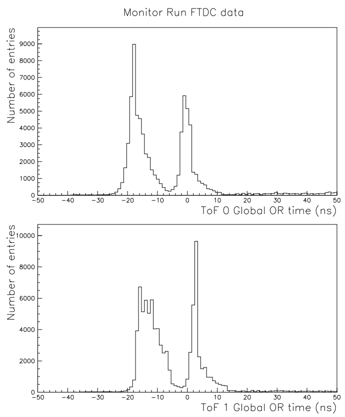


Figure 6.12: *ToF trigger FTDC timing distributions. Upper plot shows ToF 0 global OR timing, lower plot shows ToF 1 global OR timing.*



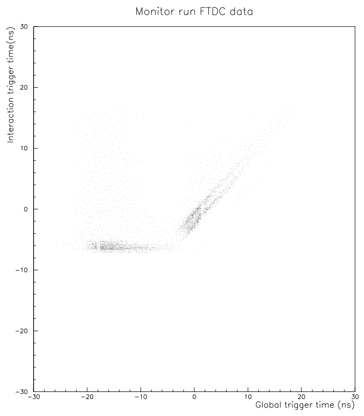


Figure 6.13: *interaction trigger time against global trigger time. Events in the horizontal part of the distribution have the correct global time, and the earliest possible interaction time.*

Another interesting feature of the FTDC distributions is shown in Figures 6.14. This shows the time distribution of hits in counters when there is a hit in the the early part of the ToF 003 distribution ($-3.0 < t0$ in ToF003$<$ 2.0 ns). A visible 'interaction' peak now appears in 'all' the counters.

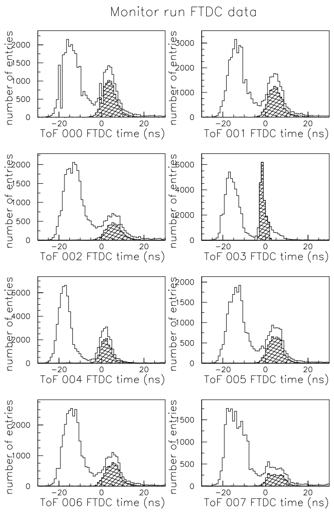


Figure 6.14: *FTDC distributions for ToF 0 counters.*

## 6.5 Analysis of the position of the interaction peak

The calculated separation of the electron and proton peaks, assuming a velocity of $c$ for all particles, is 15 ns for ToF 0 (which determines the time of the Global trigger for IA events). This takes into account the position of ToF with respect to the interaction vertex and the flight time between the walls of ToF. The measured separation was 17 ns.

Interacting bunches have a similar number and timing of interaction triggers compared to electron pilot bunches, indicating that both are dominated by electron beam background (mostly synchrotron radiation). 'Physics' events occur at the calculated time (15 ns) indicating that there is no hardware problem.

Fitting Gaussian curves to the interaction peaks of the ToF 1 global OR of three samples of varying purity shows the differences in the peak shape and position (See Figures 6.15 to Figure 6.17).

The interaction peak of the normal lumi events and the farm rejected events (which are mostly composed of $e$-beam background hits) are almost identical.

This difference is seen in data selected using the ToF IA trigger and in data with-



| Figure | Event sample type | IA Peak Position | sigma |
|---|---|---|---|
| 11 | Normal Lumi | 220.8 ns | 2.0 ns |
| 12 | Farm rejected events | 220.5 ns | 1.5 ns |
| 13 | ELAN physics sample | 218.5 ns | 2.6 ns |

Table 6.2: Relative position of interaction trigger FTDC peaks for physics and non-physics datasets

out a ToF IA trigger. The absolute position of the peaks is about 1 ns different but the relative positions are the same. Figure 6.18 shows all the peaks superimposed, no ToF IA trigger cut has been imposed.

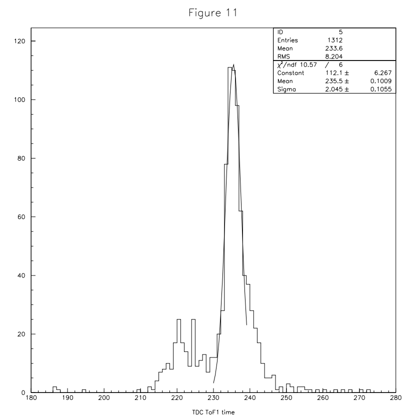


Figure 6.15: *ToF1 global OR timing for typical Lumi run.*

The time difference between the background and the interaction peaks is given in Table 6.3. The separation of the peaks of these distributions, as recorded by the online and offline TDCs, shows a discrepancy with the calculated flight time. The peaks of the *physics* distributions are closest to those calculated (usually within 1 ns).

| Counter | Calculated peak Separation | Measured online separation | Offline Monitor separation | Offline L4reject separation | Offline Physics Separation |
|---|---|---|---|---|---|
| 000 | 15.3 | 19.0 | 18.7 | 19.2 | 16.0 |
| 001 | 15.2 | 18.0 | 17.8 | 19.4 | 15.4 |
| 002 | 15.3 | 18.5 | 18.5 | * | 15.8 |
| 003 | 15.0 | 15.0 | 16.7 | 17.2 | 18.0 |
| 004 | 15.0 | 20.0 | 18.0 | 17.1 | 16.8 |
| 005 | 15.3 | 19.0 | 18.3 | 18.1 | 16.3 |
| 006 | 15.2 | 18.5 | 18.5 | 17.6 | 16.0 |
| 007 | 15.3 | 19.0 | 18.3 | 18.2 | 15.4 |
| 100 | 13.4 | * | 17.5 | * | 14.9 |
| 101 | 13.2 | * | 15.1 | * | 13.3 |
| 102 | 13.2 | 18.5 | 14.8 | 15.2 | 13.8 |
| 103 | 13.4 | * | 17.1 | * | 14.0 |
| 104 | 13.2 | 16.5 | 17.4 | * | 14.8 |
| 105 | 13.1 | 13.5 | 14.3 | 14.8 | 15.2 |
| 106 | 13.1 | 15.0 | 14.4 | 15.2 | 14.9 |
| 107 | 13.2 | * | 17.3 | * | 14.1 |
| 108 | 13.2 | 16.0 | 16.3 | 16.5 | 14.6 |
| 109 | 13.1 | 14.5 | 14.4 | 14.3 | 14.4 |
| 110 | 13.1 | 15.0 | 15.1 | * | 14.8 |
| 111 | 13.2 | 18.5 | 16.7 | * | 13.2 |
| 112 | 13.4 | * | 17.0 | * | 14.1 |
| 113 | 13.2 | 16.0 | 15.4 | * | 13.7 |
| 114 | 13.2 | 17.0 | 16.2 | * | 14.4 |
| 115 | 13.4 | * | * | * | 14.4 |
| Global | 15.2 | 17.5 | 17.2 | 18.4 | 16.0 |
| ToF0 OR | * | * | 17.2 | 18.4 | 14.3 |
| ToF1 OR | 13.2 | 16.5 | 14.9 | * | 12.9 |

Table 6.3: *Proton - Electron Peak separations in ns for various datasets. Separation is greater than calculated in all cases, but physics data is nearest to calculated values.*

A * in the table indicates that no electron peak was discernible in the data.

Reasons for the discrepancy were sought. The following possible causes were tested:



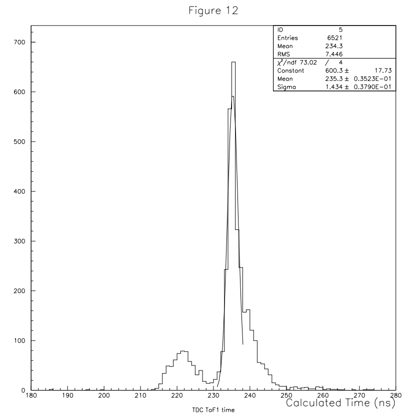


Figure 6.16: *ToF1 global OR timing for farm rejected events.*

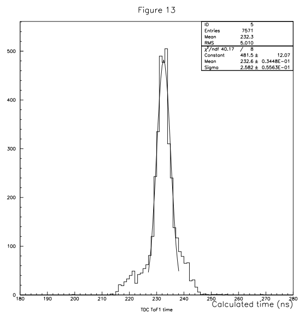


Figure 6.17: *ToF1 global OR timing for Elan DIS events.*

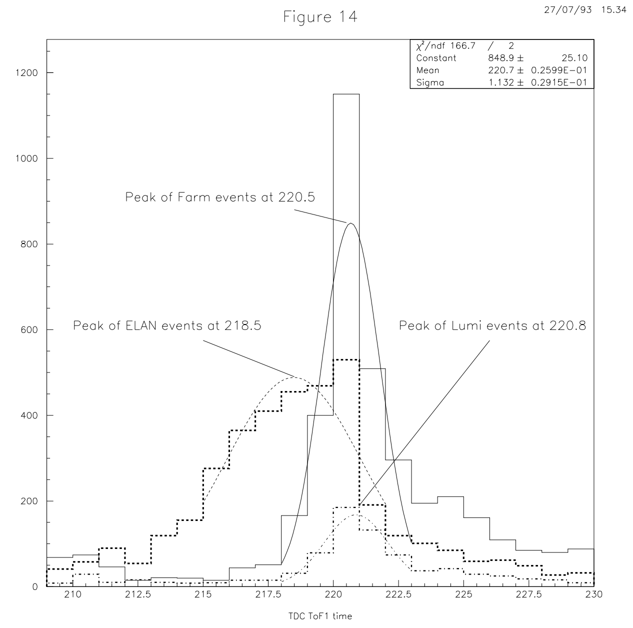


Figure 6.18: *ToF 1 global OR timing for three sorts of data. Peak of interaction distribution for physics events is 2 ns earlier than those of normal events.*



1. Bias from the hardware. The ToF trigger ANDs the first counter signal from each wall to generate a trigger signal. This may bias the means of the FTDC distributions as only the first FTDC signal in a particular channel is reconstructed.

2. Single hits from electron background dominating the data. Background associated with the electron beam, such as synchrotron radiation was expected to be quite high near the beam pipe, and could affect the timing distribution of hits in ToF.

3. Bunch structure. The proton and electron beams are expected to have a different structure from each other. This may be reflected in the peak separation.

4. Helical path of low–momentum electrons as they pass through the magnetic field of H1. If the path is much changed, the electrons will arrive at ToF later than one would expect, even if effectively still travelling at $c$.

5. Transit time in the scintillator and event multiplicity. The FTDC distribution for each counter in ToF shows an initial peak followed by a slower fall. These are thought to originate from prompt photons (initial peak) escaping rapidly from the scintillator and reflected photons (tail of distribution) which are up to several tens of nanoseconds late. This may cause the observation that high multiplicity events have a different time distribution to low multiplicity events.

6. Backscatter from behind ToF. A large quantity of metal (The nitrogen shield) lies at $z$=-2.3 m, from which particles could backscatter into ToF, causing signals in ToF which are later than expected.

**Hardware Biases**

Timing misalignments between counters caused by the ToF logic may cause the trigger times to be artificially late or early. If the counter is present in many events, this effect will be large. By looking at the individual counter timings and their respective single-wall OR trigger times, any differences were noted and their effect (if any) remedied. In principle, the time difference between the counter with the earliest time and the global OR for that wall should be very small and constant.

The counters fell into two categories:

- In-time counters (e.g. ToF 107). These have a narrow spiked distribution offset slightly from 0 as expected.

- Out of time counters (e.g. ToF 109). These have an initial spike offset further from 0, and a small but noticeable tail towards 0. The inner counters have significant tail in both ToF 0 and ToF 1.

The tail is defined as the proportion of data more than 1.5 ns after the peak position.

Out-of-time counters are too early with respect to the global OR, and the tail is caused by other counters triggering the Global OR. For those events in which the *only* counter firing within a particular wall is one from the second category, the timing distribution is a sharp peak about the spike position, indicating that these counters indeed have their zero point defined late. When the correct zero-point is used, the distributions of all counters show sharp peaks without any tail. The corrections are allowed for in the (software) event reconstruction process.

### Singles rates

Synchrotron radiation from the electron beam causes the majority of singles hits in ToF. The photons radiated by the electron are usually of low energy (typically a few hundred keV) and are absorbed by the lead shielding of ToF or by the bulk of BEMC.

A typical set of singles and coincidence rates is given in Table 6.4. Comparing the coincidence and singles rates for each counter, and for ToF as a whole, it can be seen that the singles rate for each counter is far too low for the coincidence rate to be caused by random coincidence of synchrotron hits in ToF.

For counter 000, for example, there are 4473 singles hits per second. For a trigger to fire, a hit must occur within the same beam crossing in ToF 1. The total singles rate (in Hz) for this time was about 55000. There are $1/9.6 * 10^{-8}$ beam crossings per second. Therefore the 'accidental' singles rate from random correlation of these hits is approximately $55000 \times 4473 \times 9.6 \times 10^{-8} = 23.6$Hz This compares with the actual coincidence rate of 1930, almost a factor of 100. Therefore, the late peak cannot be described by synchrotron radiation, as the rate is too low.



| Counter | Global Coincidences (Hz) | Singles Rate (Hz) |
|---|---|---|
| 000 | 1930 | 4473 |
| 001 | 3075 | 6184 |
| 002 | 2047 | 4500 |
| 003 | 8042 | 11073 |
| 004 | 7426 | 10198 |
| 005 | 4639 | 8212 |
| 006 | 2755 | 5581 |
| 007 | 2203 | 3876 |

Table 6.4: *Typical rates in ToF Counters.*

### Bunch structure

The proton and electron bunches had different shapes, with the proton bunches much larger than the electron bunches. If the distribution of the protons within a bunch were concentrated toward the front, this would produce an increased separation. However, it would also cause most interactions to occur at $z = +1.0$m, which is inconsistent with reconstructed events.

A comparison of the ToF time distribution of individual bunches shows that the electron and proton peaks are in similar positions for both interacting and pilot bunches. See Figures 6.19 and 6.20. Therefore bunch structure on its own cannot explain the timing discrepancy.

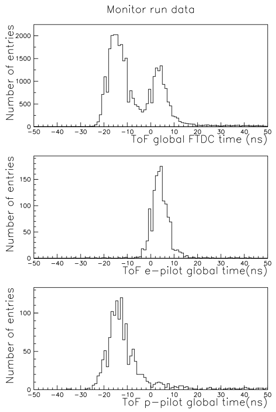


Figure 6.19: *Peak separation of a single counter, ToF 000, for interacting and pilot bunches. Interacting bunches have a peak separation of 17.0 ns, pilot bunches a separation of 17.5 ns.*

**Helical Path of the electron**

As electrons are charged particles, as they pass through the magnetic field of the H1 coil, they may be deflected in a helical path. Thus, a particle travelling parallel to the direction of the B field undergoes no deflection in that direction. Charged particles with a low momentum, such as those created by the large flux of synchrotron radiation, have a smaller radius of curvature than those from high momentum particles from a physics interaction.

A non-interacting electron travels at $c$ in the $z$ direction and is unaffected by the B-field. Only those particles with any transverse momentum will be affected. As the $z$ motion is unaffected, the arrival time of a particle at $z$=-1.95 (ie the $z$ position of ToF) will be identical whether the field is on or off. The curved path of the deflected particles means that they arrive nearer to the beam pipe than those particles unaffected by the magnetic field. Particles with a large proportion of transverse momentum, but low total momentum, which would otherwise escape from the detector in the barrel region, can be deflected into ToF in this way. Such particles would have a time distribution later than expected and could contribute to the larger than expected peak separation.

From run 60180 to run 62643, the H1 field was not operational. The FTDC



timing distribution showed that *both* the interaction and background peaks shifted by $\sim$3 ns, and is related to transit time in the pm. The separation of the peaks remained constant. Therefore, the helical path taken by electrons was not contributing significantly to the separation of the peaks.

**Transit time in the scintillator and event multiplicity**

Two particles passing through a counter of ToF simultaneously, but in different positions, will take different lengths of time to emerge from the scintillator, and give rise to different event times. Hits nearer the pm tube will give rise to earlier event times than those further away.

Comparing the multiplicity of hits in ToF, with the ToF trigger times for these events (Figure 6.21), there is a correlation between earlier times and high multiplicity events. This follows because high multiplicity events have a high probability of a particle passing close to a pm. Background events tend to have a high multiplicity, whereas low multiplicity events dominate in the interaction window (see Section 3.2.5).

Separating events by their multiplicity, a better measurement of the relative position of the interaction and background peaks can be made. Events were separated into two sets:

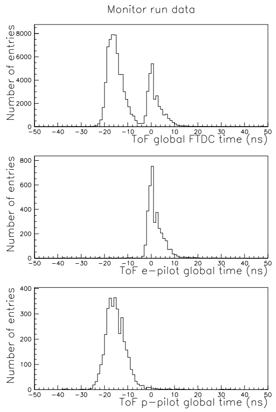


Figure 6.20: *Peak separation of a global trigger is identical for interacting and pilot bunches - 16 ns.*

1. Those events with 1 or 2 hits in each wall.
2. Those events with 4 or more hits in ToF 0 and 6 or more hits in ToF 1.

Gaussian fits were made to these sets using various FTDC channels. Table 6.5 shows the peak separation for the different datasets which is indeed increased in high multiplicity events by up to a nanosecond. This cannot explain the full discrepancy, however.

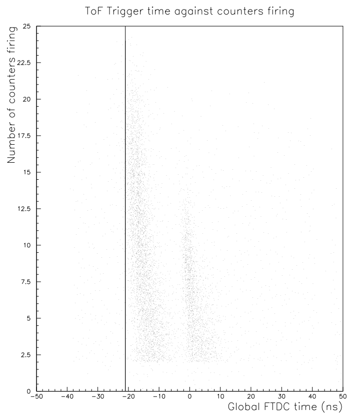


Figure 6.21: *ToF trigger time against number of counters firing. The more counters that fire, the earlier the event tends to be.*

| Data used | Low Multiplicity | High Multiplicity |
|---|---|---|
| Global trigger | 15.9 | 16.4 |
| ToF 0 global OR trigger | 15.5 | 17.0 |
| Earliest ToF 0 hit | 16.0 | 16.9 |
| Average ToF 0 counter time | 16.3 | 16.0 |
| ToF 1 global OR trigger | na | 15.5 |
| Earliest ToF 1 hit | 13.3 | 14.2 |
| Average ToF 1 counter time | 13.5 | 13.0 |

Table 6.5: *Peak separation for different FTDC datasets*

**Backscatter**

For ToF, backscattered events are those with particles which pass through ToF in the interaction window, but with tracks that indicate they originated from behind



ToF (ie away from the interaction point). The such particles would tend to have a later time then particles hitting ToF direct from the interaction point. Such events occur in electron-only bunch crossings and so are not late proton-associated particles. It was determined that backscattered particles were the major contributor to the increased peak separation and is therefore covered in a separate section below.

## 6.6 Backscattering of Particles

Particles travelling from the interaction point which pass inside the beam pipe at $z = -2.0$ m but which are scattered off material behind this, could then pass back through ToF (See Figure 6.22). Such events would have a time distribution later than those which passed directly through ToF from the interaction point and could explain the discrepancy in the peak separation. The peak of events in ToF 003 are consistent with direct particles from the interaction. The later peaks in the outer counters may be caused by backscattered interaction particles from a source behind ToF (at more negative $z$).

By separating events according to their 'directionality' (forward-going or backward going tracks) and examining the timing of such events, it will be shown that there is a contribution to the increased peak separation from backscattered events.

Figure 6.22: *Diagram showing the backscattering of particles from a point behind ToF.*



### 6.6.1 Directionality

Tracks can be extrapolated from the position of hits within ToF in a given event and assuming all tracks begin inside the beam pipe, a direction of travel can be inferred and is referred to as a track's directionality.

The directions which were inferred are summarized below.

- 'Backward'. Events with hits in only the central counters of ToF 1 and the outer counters of ToF 0 imply that the particle is travelling in a backward direction and that the event appears to originate from the beampipe at $x <\sim -1.8\ m$ ie in front of ToF.
- 'Backward loose'. Such events have either a hit anywhere in ToF 1 and no hit in the inner counters of ToF 0, or a hit in the inner counters of ToF 1 and a hit anywhere in ToF 0, or a hit in the inner counters of ToF 0 only. This is a looser requirement than 'backward' but may indicate a backward direction of travel.
- 'Forward'. As 'Backward', but with ToF 0 and ToF 1 reversed in the definition. Tracks indicate a forward direction.
- 'Forward loose'. As 'Backward loose', but with ToF 0 and ToF 1 reversed in the definition. Again, this has a looser requirement than 'Forward'.

These definitions were used to construct directionality matrices (see Figure 6.23), and Figure 6.24) which would help isolate those events which had evidence of backscatter. Events were placed in the matrix according to the location of hits in that event (e.g. ToF 0 or ToF 1, inner or outer counters). Events with no hit in ToF 0 (ToF 1) are represented in the left-(bottom-)most element. Events with a hit in only the inner counters make up the next element to the right (next higher element). Events with a hit in only the outer counters form the third row (column) element, with hits in both the inner and outer counters included in the right-hand (top-most) element. From this matrix, the apparent direction of particle travel can be inferred. Elements with boxes around have the most reliable directional information, (see Figure 6.25).

- Parallel events ('P' in matrix). These represent tracks travelling parallel to the beam pipe and therefore have no directional information .

- No direction ('N' in matrix). Events with hits in all sections of ToF or in only one wall give no indication of direction.

- Events which appear to come from the interaction point ('F' in matrix). i.e. backward.

- Events which appear to go toward the forward direction ('T' in matrix).

Once the direction of travel was inferred, it was compared with the trigger time of the event to label the event as backscattered or non-backscattered. The counter timing of the hits in each event was studied to see if there was any difference in ToF 0 - ToF 1 transit time between backscattered an non-backscattered events.

Backscattered interaction particles would hit ToF 0 before ToF 1, whereas direct particles would hit ToF 1 before ToF 0 and therefore will show a timing difference. The difference between the average ToF 0 event time and the average ToF 1 event time for an event is defined here as the travel time. By calculating the travel time for those events labelled as backscattered and those labelled as direct, a comparison can be made. Backscattered events should have a negative travel time with repect to non-backscattered events.

Figure 6.23: *Diagram showing which elements of the matrix provide directional information. Events with F elements have tracks from the interaction point. Events with T elements have tracks going towards z=0.*



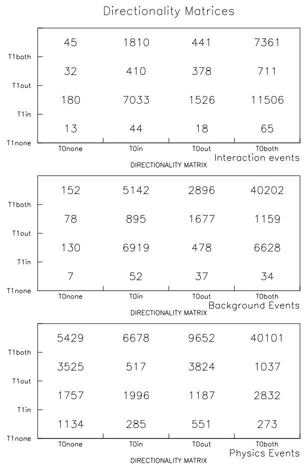


Figure 6.24: *Matrices showing number of hits in inner or outer counters of ToF. From these a measure of the direction of events can be made.*

Figure 6.25: *Figure showing particle direction inferred from position of hit in ToF. Assuming the origin is always in the beam pipe, track 1 appears to come from the interaction point and hit inner counters of ToF 1 and outer counters of ToF 0. Track 2 appears to come from the incoming proton direction as it hits inner counters of ToF 0 and outer counters of ToF 1).*



### Evidence for backscatter

The ToF monitor run (run 54665), which has a large number of background triggers (BG), and the ELAN physics sample, which includes events both before and after final physics cuts, were used in this study. The monitor dataset was divided into two subsets, those with BG triggers and those with IA (interaction) only triggers.

The proportion of apparently backscattered events in each sample is given in Table 6.6.

| Event type | Expected direction | Backscattered direction |
|---|---|---|
| Monitor BG | 12.0% | 15.0% |
| Monitor IA | 46.0% | 10.0% |
| Physics before cuts | 18.5% | 11.0% |
| Physics after cuts | 29.0% | 14.5% |

Table 6.6: *Proportion of apparently backscattered events inferred from direction of travel*

The proportion of backscattered events seems independent of the sample, and the physics sample, (after cuts) which has the expected peak separation, has one of the highest proportions of apparently backscattered events. Actually, the 'backscattered' events in the post-cut physics sample are more likely to be real physics which happen to hit the inner counters of ToF 0 and the outer counters of ToF 1 simultaneously. Most physics events have some ToF information in them, caused by particle showers escaping from BEMC and being recorded in ToF 1.

The travel times for backscattered and direct events from the various datasets is given in Table 6.7.

| Event type | Expected | Backscattered | Difference |
|---|---|---|---|
| Monitor Background | -4.1 ns | -1.1 ns | 3.0 ns |
| Background single hit | -2.0 ns | 0.2 ns | 2.2 ns |
| Monitor Interaction | 2.6 ns | -1.2 ns | -3.8 ns |
| Interaction single hit | -0.8 ns | -2.3 ns | -1.5 ns |
| Physics before cuts | 0.8 ns | -0.1 ns | -0.9 ns |
| Physics after cuts | 0.7 ns | 0.6 ns | -0.1 ns |

Table 6.7: *Relative timing of events $<\mathrm{ToF}\ 0> - <\mathrm{ToF}\ 1>$.*

Events are divided into several groupings. Single hit events are those with a single hit in each wall. The average times were used to remove any bias caused by triggering. Events from the monitor run have a peak separation that is larger than expected, while for the post-cut physics events the peak separation is essentially as expected. The accuracy is to $\sim \pm$ 0.5 ns).

The difference in flight times between events labelled as backscattered and those travelling in the expected direction is ~2-4 ns. This compares with the expected time difference of ~3 ns (ie twice the flight time between the walls of ToF), assuming a velocity of $\sim c$.

Post-cut physics events show very little timing difference between 'backscattered' events and those travelling in the expected direction, showing that for this sample there is very little true backscattering. This is mirrored in the peak separation for this sample, which agrees well with the theoretical separation.

## 6.7 Conclusion

Although efforts were made to improve the reconstruction of the Autumn 1992 FTDC data, the problems which were present throughout the run meant that no significant improvement occurred. Techniques developed in this attempt were, however, very useful in the Summer 1993 run and allowed a rapid improvement in the speed and accuracy of reconstruction compared with 1992.

Offline analysis showed that the larger than expected peak separation seen in some of the ToF FTDC distributions was in part caused by backscattered particles and in part by the effects of the different event multiplicities of background and interaction events.



# Chapter 7

# Background contamination and loss

## 7.1 Methods of calculating the efficiency of ToF.

With the trigger and FTDC data from ToF understood, two independent measurements of the efficiency of ToF were made. The measurement of efficiency is vital to maximise the vetoing of background events while minimising the loss of wrongly-vetoed physics events. Efficiency is defined in terms of contamination of the physics sample by background (BG) events or loss to the physics sample from wrongly vetoed physics events.

The dominance of triggers from forward going background particles over those from physics particles requires the ToF veto to bring the trigger rate down to acceptable (~ few Hertz) levels. As ToF vetoes 99% of all triggers which occur in H1, it is vital to know what proportion of real physics events are lost because of the position of the ToF background time window.

The first (earlier) measurement uses ToF BG triggers in the physics sample to estimate contamination. The second method uses FTDC data to estimate the loss to physics.

Offline methods of estimating background contamination is presented as well as a log-likelihood method of separating background from non-background events, which combines the FTDC information from individual ToF channels. This method is used for contamination studies.

## 7.2 Measurement of Contamination and Loss

### 7.2.1 First Method using BG Triggers

For the 1992 data, a measurement of background contamination in four physics samples was made using trigger data, comparing the number of events which had a ToF BG trigger with the number of events which did not. This measurement provides a correction to the measured cross-section for the four processes studied: ELAN, HADES, $\gamma$-p and $\rho$.

#### Method of calculation

By comparing the number of ToF background (BG) triggers with the total number of unvetoable (qv) events within a given sample, an unbiased estimate of efficiency was measured. Wrongly-vetoed physics events lower the measured cross section for physics processes.

The final correction to each cross-section is given by the proportion of events in the sample with a ToF trigger (a), multiplied by the percentage of physics events labelled as background (b). For each sample, only those software cuts which have no ToF component are used, resulting in the four 'final ToF physics samples'.

Initially, two conservative assumptions are made:

The proportion of background events wrongly labelled as interaction events is independent of physics process studied.

All events in the final sample are real physics events, so any remaining background events must be wrongly labelled interactions.

To find (a), the number of events in each final ToF physics sample with ToF trigger elements is found. This is compared to the total number of events in the final ToF physics sample for that process to give the proportion of events which are affected by ToF.

To find (b), the number of events with a ToF BG trigger is compared to the number of events which *could* have had a ToF BG trigger and have some sort of ToF trigger present. The latter group includes only those events triggered by actual subtriggers which, by arrangement, do not have the ToF veto applied to them (unvetoable triggers). Such events give an independent measure of the proportion of events vetoed by ToF at level 1. and include all ToF BG triggers.



For certainty, the physics events which contain ToF BG triggers were studied to check whether they were indeed good physics interactions or genuine background events which had evaded the software cuts.

#### Results

The four physics samples studied, all contained low-$Q^2$ physics, as this was the first year of operations and only low-$Q^2$ events had occurred in sufficient numbers for statistical analysis. The ELAN and HADES samples were found using cuts given in [17] and contained D.I.S. candidate events. As BPC/BEMC were used extensively in this search, proton background was a large potential problem.

The $\gamma$p sample contained photoproduction events, which were selected by finding an electron of the correct energy in the electron tagger. In principle, this trigger was less affected by proton background at level 1 and so had no veto applied for much of the running period.

The line marked * in the table was calculated slightly differently from the others. All independent triggers are considered in the final number, and no correction is made for the proportion of ToF hits in the sample (all events were taken by the same trigger). Scanning was conducted and determined that some background events had background-like ToF activity. Therefore the 9 events quoted in the sixth line of the above table are those events which are labelled as interaction events after scanning.

#### Comparison of the Samples

Each sample shows a low proportion of background events present. The actual proportion of background events in each sample varies, but the proportion of events with a background trigger to events with a ToF interaction trigger remains constant within errors at 4.9±1%, the number found from the online calculation [20].

Note that the $\gamma$p sample has a very small correction simply because most of the events taken were independent of the ToF veto.

### 7.2.2 Second Method - FTDC timing

#### Method

To estimate the loss to various physics samples because of the ToF veto, the FTDC data from the ToF global trigger was used. A Gaussian distribution was fitted to

| Data | ELAN sample | HADES sample | $\gamma p$ sample* | $\rho$ sample |
|---|---|---|---|---|
| Number of events in sample | 2461 | 1691 | 1024 | 7018 |
| Number of events with an unvetoable trigger | 458 | 51 | 776 | 193 |
| Number of events with any ToF trigger | 1323 | 752 | 299 | 165 |
| Number of events with a ToF trigger and unvetoable trigger | 48 | 31 | 241 | 30 |
| Number of such events with background trigger element (BGtrig) | 2 | 1 | 24 | 5 |
| Of these: accepted real physics events with unvetoable trigger and BGtrig | 2 | 1 | 9* | 5 |
| Proportion of IA events with BGtrig and a monitor trigger | 4.2± 3.0% | 3.2± 3.2% | 3.7± 1.2% | 16.7± 7.5% |
| Proportion of events with IA trigger | 53.7% | 44.5% | 29.2% | 2.4% |
| Proportion of independent triggers with a ToF BG trigger | 0.44% | 1.9% | 1.1% | 2.6% |
| Total correction to cross section | 2.3± 1.6% | 1.4± 1.4% | 0.26± 0.09% | 0.40± 0.18% |
| Total correction to cross section 2nd method * | na | na | 0.29± 0.11% | na |

Table 7.1: *Corrections to 1992 data from ToF FTDC results.*



the peak of the ToF global trigger FTDC distribution. The number of events in the portion of the fit which corresponded to the peak of the FTDC distribution was normalised to the number of events in the peak. The difference in the number of events in the data compared with those in the fit was then taken to be the number of events cut by ToF. The ToF global FTDC was chosen as it should include all events which could in principle be vetoed by ToF (i.e. a hit in both walls) but in fact were not (because of their timing).

A Gaussian fit was chosen because the centre of the physics peak has a Gaussian shape and the peak is not wide enough to fit different curves to the rising and falling parts of the distribution. Any attempt to fit a rising distribution would include bins which have events missing from them, and would therefore underestimate the loss.

The physics peak has a different shape from the normal interaction peak, and so parameters found in the fit to the interaction peak cannot be transferred to the physics peak.

Three different Gaussian distributions, all of which had $\chi^2$/NDF of less than 2, were fitted to the peak, giving a mean, a minimum and a maximum estimate. The mean value was taken for the final result and the minimum/maximum used to estimate systematic errors. The parameters used for the ELAN data sample are given in table 7.2.

| Fit | Parameter | Value |
|---|---|---|
| Minimum | Height | 2139 |
| | Centre | 0.35 |
| | Width | 2.78 |
| Mean | Height | 2144 |
| | Centre | 0.22 |
| | Width | 2.75 |
| Maximum | Height | 2093 |
| | Centre | 0.09 |
| | Width | 2.84 |

Table 7.2: *Parameters for Gaussian fits to ELAN data sample.*

**Results for 1993 losses**

The following are the losses to physics events caused by the ToF veto. They should be considered as corrections to the total cross section for these events.

| Dataset | Proportion of Global FTDC missing | Proportion of full dataset |
|---|---|---|
| ELAN | 1.83% | 1.41% ±0.07% ±0.45% |
| HADES | 1.27% | 0.99% ±0.07% ±0.38% |
| ETAG | 1.26% | 0.82% ±0.03% ±0.19% |

Table 7.3: *Losses to 1993 physics data*

## 7.3 Estimating Contamination and Loss

The offline ToF trigger FTDC data can be used to estimate the expected loss to the whole dataset for comparison with the measured value and the estimate from online data. The individual FTDC channels can be combined to give a further indication of whether an event is background or interaction.

### 7.3.1 Using Trigger FTDC data

An estimate of loss to the physics dataset can be made by combining the position of the ToF time windows (known as strobes) with the effects of the fall in efficiency at the start and end of the strobes, and the expected position and width of the 'physics' global ToF trigger FTDC distribution.

The physics peak of the ToF global trigger FTDC distribution approximates to a Gaussian peak with an additional exponential fall. Parameters were obtained by fitting a Gaussian plus an exponential decay beginning at the full width half maximum point of the fall of the Gaussian to the peak of the ToF global FTDC distribution of the ELAN sample. By fitting to the peak only, events missing because of the actual position of the ToF background strobe should not affect the results. The missing events were calculated by comparing the value measured from the fit to the data for that point.

The estimated loss to physics events with a ToF global trigger as a function of the ToF background strobe position is given in Figure 7.1. The correction for the loss of efficiency (see Section 6.4.2) at the end of strobe is included in this, with the end of the strobe defined as the 50% efficiency point of the strobe efficiency plot.

Any number calculated in this way must be multiplied by the proportion of physics data which has a ToF global trigger in order to get a final estimate of loss. For the actual position of the ToF background strobe (-5 ns), the expected loss is



~1.5%.

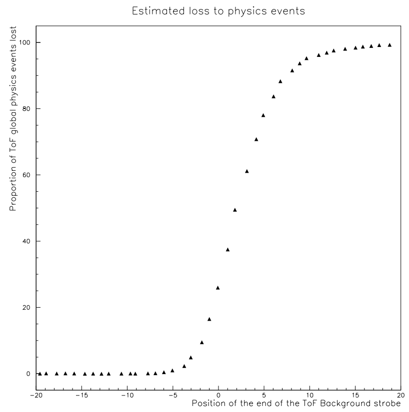


Figure 7.1: *Estimated loss to physics data which has a ToF global trigger as a function of the position of the end of the ToF background strobe.*

In order to estimate the amount of background which is not vetoed by ToF, but which passes through ToF, a function approximating the shape of the ToF global FTDC distribution was fitted to the monitor run data. Each peak was fitted separately and the proportion of each peak lying after any given strobe position could be calculated.

Several fits to the peaks were modelled before the final one was chosen: a function with a Gaussian rise which also covered the peak and a falling exponential to a fixed value describing all parts after this. The same general function form, but with different parameters was used to fit both the electron and proton peaks. The similarity in the shapes of both distributions (especially the falling exponential) indicates that the shape of both distributions is dominated by apparatus effects (light escaping from the scintillator) and not bunch structure. Figure 7.2 shows the data and the fit.

From this fitted data, the proportion of each peak lying after any particular point was calculated and the results are shown in figure 7.3.

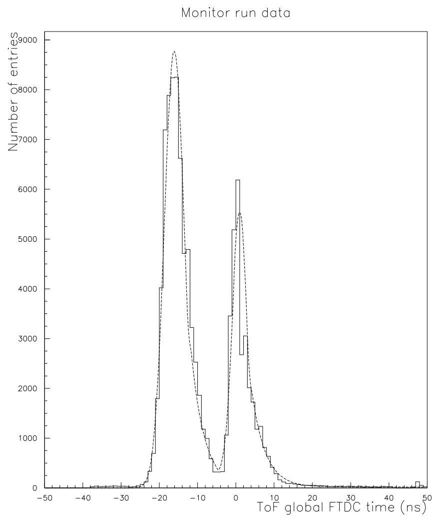


Figure 7.2: *Fit to ToF global data from monitor run.*



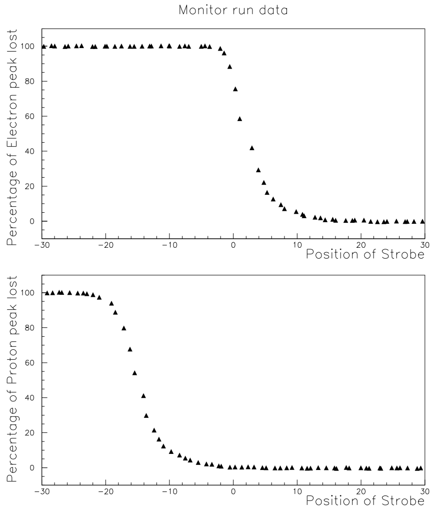


Figure 7.3: *Loss to Electron and background peak as a function of strobe position. Also gives proportion of events not vetoed (100-value from graph).*

In order to calculate the absolute proportion of data after the end of the proton strobe which comes from the proton beam, the heights of the two peaks must be compared. The heights of the proton and electron peaks which are recorded by the FTDCs will be smaller than that for the monitor run as not all ToF triggers are used to keep an event. The proton and electron currents are therefore used to calculate the expected height of the proton and electron distributions.

$$P_{height}(corr) = P_{height}(mon)\frac{P_{curr}(lumi)}{P_{curr}(mon)} \tag{7.1}$$

$P_{height}(corr)$ is the corrected height of lumi run proton peak.

$P_{height}(mon)$ is the height of the monitor run proton peak (8790).

$P_{curr}(mon)$ is the proton current from the monitor run (80.0)

$P_{curr}(lumi)$ is the proton current from the luminosity run being studied.

For the monitor run proton current and peak height this gives:

$$P_{height}(corr) = 8790.\frac{P_{curr}(lumi)}{80.0} \tag{7.2}$$

For the monitor run electron current (60.0) and peak height (4500) the equation becomes:

$$E_{height}(corr) = 4500.\frac{E_{curr}(lumi)}{60.0} \tag{7.3}$$

The shapes of the proton and electron peaks must also be taken into account, with a correction factor for the height to area ratio. The final calculation of contamination was as follows:

$$\frac{H_p \times F_b(t)}{H_p + H_e} \tag{7.4}$$

where:

$H_p$ is the corrected height of the proton distribution.

$H_e$ is the corrected height of the electron distribution.

$F_b x(t)$ is the function giving the proportion of the background peak lying after a time $t$, the end of the background strobe.



For typical currents,electron=50.0, proton=50.0 and the strobe positioned at $t = -4.0$ (proportion of BG data after strobe ~1.0%) the calculation gives:

$$\frac{5495. \times 0.01}{5495. + 3750.} = 0.6\% \tag{7.5}$$

Luminosity runs show that the shape of the FTDC distributions can sometimes be very different, with a large flat tail of events after the peak. This will change the result of the calculation for such distributions. This and other online ToF TDC data is analysed in [20].

### 7.3.2 Estimates using individual FTDC data

The ToF individual counter FTDC information was combined to give the probability of an event being related to the electron or proton beam. Initially, the shape of electron and proton pilot bunch FTDC distributions were used to find the probabilities of individual counter times being electron or proton related. These were then combined using the (negative) log likelihood method. The two probabilities for an event, for being either electron or proton related, can then be compared, and a final combined probability given.

This process was repeated using 1993 ELAN selected physics sample instead of the electron/proton pilot bunch, and a comparison made with the previous method.

#### Motivation

Each ToF trigger uses a coincidence of the earliest hits in both ToF 0 and ToF 1 because of the fear that there would be high numbers of unwanted random triggers if single wall triggering was used. This is studied in Section 4.6.7. The problem in requiring a coincidence is that many particles pass through only one wall of ToF will not cause a trigger and 'early' or 'late' single hits in one wall cause a mis-labelling of interaction events as background and vice-versa. Also, in order to minimize the loss of physics events, the ToF strobes were set early (see Appendix C.1.6) so some events which lie inside the background distribution lie outside the time of the background strobe.

Combining the FTDC times of individual ToF counters is a way of overcoming these problems. A probability is assigned to each counter for each event as to whether the data registered is associated with the proton or electron beam. Proton beam associated data is background, whereas electron associated data may not be. In this way an estimate of the contamination of proton background in any sample may be made.

In principle a cut could then be made on the data, at level 4, to prevent the filling of storage tapes and disks with background events. In practice this method was not used for such a purpose as storage space was not a problem and the saving in deadtime (the most important trigger problem during 1993 and 1994) was minimal. It is a useful extra offline measure of contamination of physics events. However, a study of the proportion of data which would have been cut has been made, and is covered in the following sections.

## 7.4 Determining probability

### 7.4.1 Initial Approach

Initially the proton and electron pilot bunches were used to calculate the relative contribution from each beam in each counter of ToF. For each counter the FTDC times for electron pilot, proton pilot and interacting bunches were compared (see Figure 7.4). The proton pilot-bunch data shows that some particles definitely associated with the proton beam are seen well into the time where electron associated particles are most common.



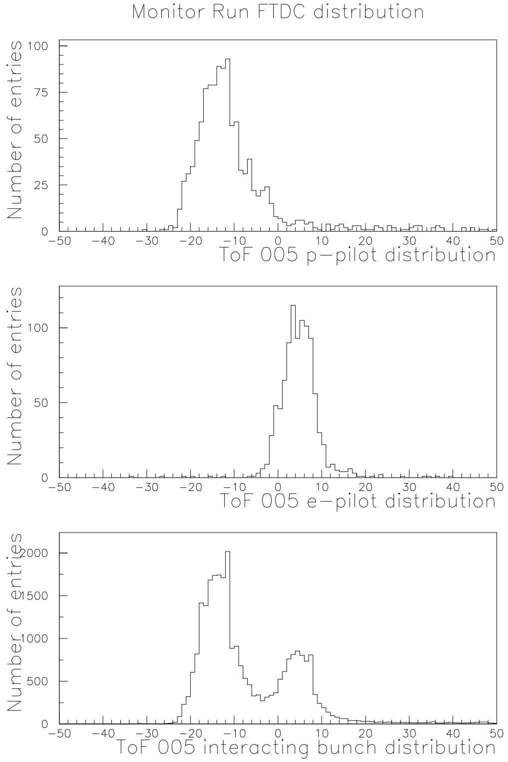


Figure 7.4: *Pilot bunches and full data FTDC distributions from the monitor run for counter ToF 005.*

The proton pilot bunch was matched to the interacting data bunch by fitting both to a Gaussian distribution and normalising the areas of the fits. The pilot bunch data was then subtracted from the interacting data and the resulting interaction peak matched to the electron pilot peak via a similar process. The normalised peaks are referred to as constructed peaks.

The mismatch between constructed and raw data distributions leads to errors in the final calculation. The maximum difference of 200 entries is actually only just outside of one standard deviation of the pilot data, as the constructed data has been multiplied up from a much smaller sample.



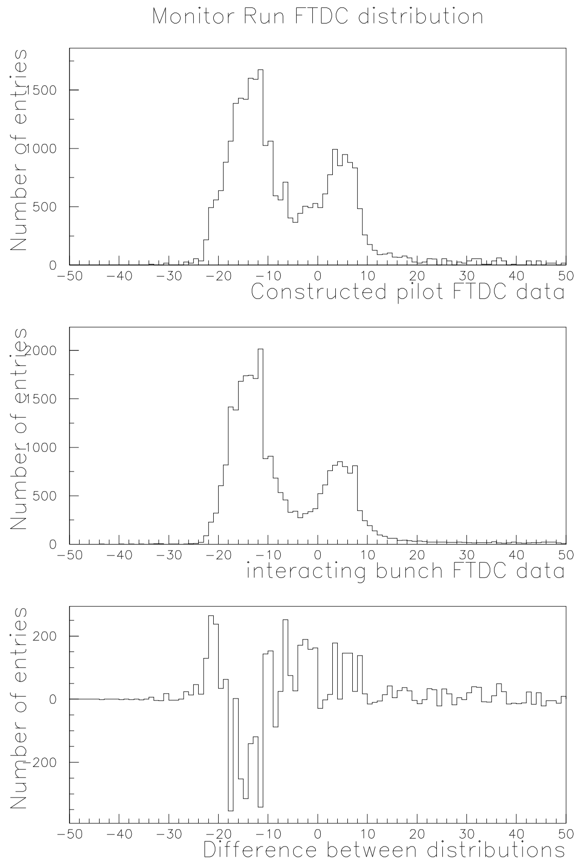


Figure 7.5: *Plot of monitor run FTDC data from a single counter. Top diagram is constructed from pilot data. Middle plot is the raw data. Bottom plot is the difference between the two plots.*

The constructed peaks were then used to calculate the probability of a hit with time t being electron associated ($P_{ea}$) or proton associated ($P_{pa}$).

$$P_{pa}(t) = (N_p(t) * QP)/((N_p(t) * QP) + (N_e(t) * QE)) \tag{7.6}$$

and similarly :

$$P_{ea}(t) = (N_e(t) * QE)/((N_e(t) * QE) + (N_p(t) * QP)) \tag{7.7}$$

$N_p(t)$ is the number of events in bin t in the constructed proton data.

$N_e(t)$ is the number of events in bin t in the constructed electron data.

QE is the electron beam current (normalized to the monitor run electron current).

QP is the proton beam current (normalized to the monitor run proton current).

The beam currents are used to find probabilities for other datasets by normalizing to the monitor run beam currents. If no data is present in a time bin, adjacent bins are summed until at least 50 data points are present and the total divided amongst by the number of bins sampled to remove any zeroes.

The time $t$ covers only the central time region (-25 ns to 25 ns) of the trigger bunch crossing. This is because the vast majority of counter hits occur within this period and events outside this window are almost certain to be from cosmic rays or other particles not associated with the electron beam. Times which lie outside the nominal event bunch crossing were ignored as they play no part in the 'trigger decision process'.

#### The Log Likelihood Calculation

Having found e- and p-probabilities for each counter in each event, the next step is to combine them.

This is done by first adding the natural logarithms of the electron probabilities of each counter which fired.

$$L_e = \Sigma_{counters} ln P_{ea}(t) \tag{7.8}$$

The same is done (separately) for the proton probabilities.

$$L_p = \Sigma_{counters} ln P_{pa}(t) \tag{7.9}$$

The difference between these numbers gives a measure of the likelihood for an event to be either electron or proton associated.



$$L_{diff} = L_e - L_p \tag{7.10}$$

Events which are very unlikely to be, say, electron associated have a large negative electron log sum and a small negative proton log sum. The difference between these is large and positive. Events which have an equal probability of being electron or proton related have electron and proton log sums of the same magnitude. Cases where probability equals 1.0 of being one and 0.0 of being the other were avoided by summing adjacent bins as described in Section 7.4. As all probabilities lie between zero and one the natural log of each probability is always negative.

A log likelihood difference of (positive) 0.5 indicates a 68% probability of being proton related, and a log likelihood difference of 3.0 indicates a >99% probability of being proton related. Errors in the calculation stage make these 'ideal' numbers less exact. Therefore a 6 sigma (rather than a more usual 3 sigma) cut is quoted below.

Events can be labelled as electron certain ($L_{diff} < -3$), electron possible ($L_{diff} < 0$), proton possible ($L_{diff} > 0$), or proton certain ($L_{diff} > +3$).

### 7.4.2 The Equal Assumption Method

The initial method did not give consistent answers when applied to physics data (see Section 7.4.3). Events selected as physics should be overwhelmingly associated with the electron beam, but Figure 7.7 shows that a large fraction are labelled as proton associated.

The problem arose because the probability distribution of hits the outer counters for the monitor run is such that even in the centre of the electron distribution the probability of an event being electron associated is less than 50%.

Another approach assumes that there is an equal *a priori* probability of a randomly selected particle in any counter being either proton or electron associated, requires only that the probability distributions follow the shapes of the distributions of the pilot bunches.This will be referred to as the 'equal *a priori* probability distribution' and the method as the equal assumption method.

This distribution was calculated by individually normalizing the e- and p-pilot bunch data in each counter to the same area . The probability was then calculated as in Section 7.4.

The 'equal *a priori* probability distribution' takes:

$$P_{pa}(t) = N_p(t)/(N_p(t) + N_e(t)) \tag{7.11}$$

and similarly :

$$P_{ea}(t) = N_e(t)/(N_e(t) + N_p(t)) \tag{7.12}$$

where the definitions remain the same as in equations 1 and 2.

#### Further Refinements

Once the method has been proved to be useful, certain refinements are possible. Instead of using the electron-pilot bunch in Section 7.4.2 to give the shape of the 'interaction' distribution, the ELAN data sample from miniDST were be used. Then a probability of being proton-related or 'physics' related can be given to each event. Also events with only one hit in ToF can be excluded, although these events tend to fall into the middle - ambiguous - region

In the future, the FTDC distribution from 'physics' data sets will be used to find the e- and p-probability distributions.

### 7.4.3 Results

The results from all three methods show the improvement the later methods give. See Figures 7.6 to 7.12. Raw data, physics data and level 4 rejected events were all studied.

#### Log likelihood

Figure 7.6 shows the log likelihood distribution of the monitor run events as calculated by the three methods. All plots show a left hand electron associated (interaction) peak and a right hand proton-associated (background) peak. The spikes in the right hand peak of the upper plot are caused by the number of counters firing in an event(e.g. $x = 10$ is from events where only two counters fire). This effect is hidden in the left hand peak where the spikes merge into a continuum.

Figure 7.7 shows the log likelihood distribution of the ELAN physics events for the three methods. Only the interaction peak of Figure 7.6 is present as all events should (in principle) be electron associated. The original method labels a significant



proportion as background related, whereas the final method labels almost all as interaction related. See table 7.4.

These results showed that the initial method was not suitable and that the refined equal assumption method was the one which should be used for further study.

Figure 7.8 shows the log likelihood distribution of the of level 4 rejected events, of which a small number are stored for later analysis. A significant proportion (c. 40%) of these events have ToF data in them. This data contains many events with log likelihoods of near zero, most of this coming from hits in a single wall of ToF. Two peaks in the data (at $L_{diff} = 5$ and $L_{diff} = -5$) can be seen if these single wall hits are excluded.

#### Combining Log Likelihood and timing

Figures 7.9 to 7.11 show the log likelihood and so-called 'India' plots for the ELAN sample.

Figure 7.9 shows the log likelihood distribution of monitor run events plotted against the Global trigger time of those events. The events lying above 0 log likelihood (background) generally have timing consistent with background events, but some lie well within the interaction time window (0 - 20 ns on the Global FTDC time).

Figure 7.10 shows a similar plot for ELAN physics events. Almost all events lie in the electron-associated (interaction) region. A small number, mostly early ($< -5$ ns) or late ($> 15$ ns) are background related (See table 7.4).

#### Comparison with the trigger data

The trigger data can be used to show the proportion of events which have an interaction or background trigger which are labelled background definite. The three methods of calculation refer to the initial method, equal assumption method and refined equal assumption method.

The table shows that the refined equal assumption method gives good agreement between the ToF background trigger and those labelled as background, while showing that the interaction trigger does contain some background events. The final physics data sample contains very few events labelled as background definite.

Unfortunately the log likelihood calculation cannot provide a level 1 veto to

| Data Sample | Method | IA trig BG definite | BG trig BG definite |
|---|---|---|---|
| Monitor | 1 | 6.2±0.1 | 99.5±0.03 |
| | 2 | 4.6±0.1 | 98.3±0.05 |
| | 3 | 3.8±0.1 | 98.3±0.05 |
| ELAN (all) | 1 | 14.3±0.2 | 22.5±7.5 |
| | 2 | 1.0±0.04 | 5.0±3.5 |
| | 3 | 0.4±0.03 | 2.5±2.5 |
| ELAN (post-cut) | 1 | 12.4±0.3 | 0 |
| | 2 | 0.2±0.03 | 0 |
| | 3 | 0.04±0.01 | 0 |

Table 7.4: *Proportion of events labelled as Background definite by the three methods.*

improve the ToF BG coincidence veto in the current triggering scheme. The individual counter data becomes available at level 4, but the ToF veto signal is required at level 1.

### 7.4.4 Effect on triggering and final data sets

This method could be used to veto additional background events which are currently labelled as interaction by the level 1 ToF trigger elements. The ToF FTDC information is available at level 4 and so a log likelihood cut could be used to remove some background events which are not labelled as such by the ToF trigger. The effect on the POT datasets and physics events is shown below.

#### Proportion of Raw data labelled as background

Those events which reach the Raw and POT tapes are mostly non-physics events. ToF FTDC data appears on 20% to 40% of all POT events (run-dependent) and therefore a quick cut which could remove those remaining unvetoed background events is useful. Figure 7.12 shows the proportion of events labelled as background as a function of the value of the log likelihood cut. A 6 sigma cut would remove 20% of the events with ToF information, removing 4% of all events.

Table 7.5 shows the proportion of raw and Level 4 rejected events, with some ToF FTDC information in, which are labelled as background definite. The data was taken from the 1993 run.



| Dataset | Method | Background definite events |
|---|---|---|
| Raw | 1 | 34.8±0.8% |
| | 2 | 13.2±0.7% |
| | 3 | 10.4±0.6% |
| L4 Reject | 1 | 53.8±1.1% |
| | 2 | 36.4±0.9% |
| | 3 | 34.0±0.9% |

Table 7.5: *Proportion of Events labelled as Background.*

#### Proportion of physics identified as background

There three physics datasets studied were those from the ELAN and HADES groups (DIS) and the $\gamma$p (photoproduction) group. The final results are given in table 7.6. Results are quoted separately for the equal assumption method with the e-pilot bunch for the calculation and the method which used the ELAN sample. Also given are estimates of the background contamination remaining in each sample.

ToF FTDC data is present on c.98% of the ELAN miniDST (mdst) data. Of these 92.5% are given a log likelihood by the refined equal probabilities method. Figure 7.12 shows the percentage of these events which have a log likelihood larger than the value on the x-axis. For the 6 sigma cut this gives a loss of 2.7% of the total ELAN mdst sample. Equivalently this is a 2.7% contamination of the ELAN sample by background events. Scanning of several events has shown that in most ($> 80\%$) cases these events really are background.

The HADES data sample includes similar events to the ELAN sample as they are both DIS candidate samples. ToF tdc data is present on 98.2% of the mdst tape. For the HADES sample, both the mdst and a final 'good' data sample were available. The second sample was obtained through further physics cuts.

The estimate of contamination is taken from the average of the number of events in each sample labelled as background by the equal assumption and refined equal assumption methods. The results show that there are few events in the final physics sample which appear to be background events from the ToF event timing. There may be late proton background in all of the samples, and an estimate of this is given in Chapter 8.

| Data | Cuts applied | Events | Percentage |
|---|---|---|---|
| ELAN | Total number events | 82420 | 100% |
| | ToF FTDC data present | 80777 | 98.0±0.3% |
| | Tagged by method | 72793 | 88.3±1.4% |
| | $L_{diff}$ gt 3 | 3007 | 3.7% |
| | Further physics cuts | 22578 | (100%) |
| | $L_{diff}$ gt 3 after physics cuts | 90 | 0.4±0.04% |
| | $L_{diff}$ gt 3 refined physics cuts | 32 | 0.14±0.03% |
| | Contamination | | 0.27±0.13±0.03% |
| HADES | Total Number of events | 32780 | 100% |
| | ToF FTDC data present | 32198 | 98.2% |
| | Tagged by method | 31677 | 96.6% |
| | $L_{diff}$ gt 3 | 701 | 21.5% |
| | Further physics cuts | 10031 | (100%) |
| | $L_{diff}$ gt 3 after physics cuts | 79 | 0.79±0.09% |
| | $L_{diff}$ gt 3 refined after cuts | 45 | 0.45±0.07% |
| | Contamination | | 0.62±0.17±0.07% |
| $\gamma$p | Total Number of events | 116329 | 100% |
| | ToF FTDC data present | 100049 | 86.0% |
| | Tagged by method | 83799 | 71.6% |
| | $L_{diff}$ gt 3 | 400 | 0.48% |
| | $L_{diff}$ gt 3 refined | 99 | 0.10% |
| | Contamination | | 0.29±0.19±0.02% |

Table 7.6: *Events labelled as background definite using log likelihood method in 1993 physics samples. Estimates of contamination given.*



### 7.4.5 Errors and Mislabelled events

There are several ways errors can occur in this method of labelling events.

- Counter timing.
- Bunch structure.
- Early interaction events

#### Counter timing

If the timing of counters relative to the calibration FTDC distributions, used to determine the probability, is out, this has serious effects on the proportion of mislabelled events. For example an error of 5 ns on each counter timing would cause the proportion of physics events labelled as background to rise from c.2.5% to c.70%. Changes in hardware can lead to differences in counter timings but changes in the shape of the beam can also affect the FTDC distribution of a ToF counter.

#### Bunch Structure

There were serious flaws in the initial method, with different timing distributions for the monitor run and for physics events. The refined equal probabilities method is optimized to the shape of the physics peak, but this also has problems. The physics peak is earlier than the interaction peak and lies in the 'valley' of the global FTDC distribution. Events early in this peak are given a positive log likelihood, as the proton peak is still dominant in this particular time bin.

The shape of the interacting proton bunch is different from the shape of the proton pilot bunch used to determine probability. The tail of the distribution is dominated by light escaping slowly from the scintillator and from beam wall events under the BEMC. This tail is most important in the 'valley' and events will be labelled as more proton-associated in this region. From scanning, 22 ±3 % of those physics events labelled as background ($L_{diff} > 3$) appear as possible physics events.

Satellite bunches affect the shape of the FTDC distribution of the proton beam. Only the effect on the tail of the distribution will affect the probability calculation causing early interaction events to be labelled as less definitely interaction.

### Early interaction events

Physics events occur early in the interaction peak and there is therefore a greater chance of mis-labelling such events. Comparison with early FToF results enable an estimation of the amount of such an error. The details are given in the next chapter.

## 7.5 Conclusion

This method of background discrimination can be used to remove those background events which appeared on the final data tapes because of the positioning of the strobes to minimize physics losses. It was also used to estimate the amount of background contamination in the physics datasets.

The loss to the final physics data sample from such a cut would be small and includes real background events which remain after all other cuts.

Care was taken to ensure the correct time distribution of ToF FTDC hits was used.

Further studies were be performed to find the optimal setting of the $L_{diff}$ to minimize the 'real' physics events wrongly labelled as background. These are given in the next chapter.

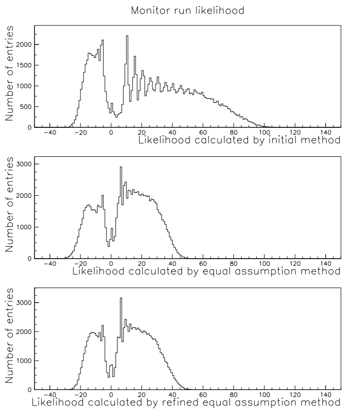


Figure 7.6: *Log likelihood of events from the monitor run as calculated by various methods. Top plot shows original method. Note spikes on right hand side - related to event multiplicity. All plots show left hand interaction peak and right hand background peak.*



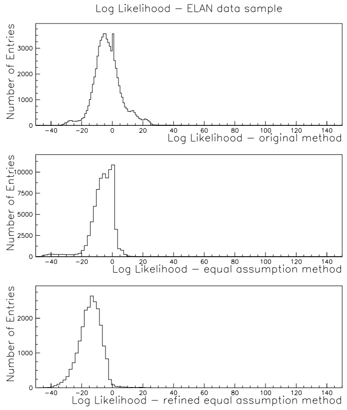


Figure 7.7: *Log likelihood of events from the ELAN (physics) dataset as calculated by the the three methods. Only one (interaction) peak is present. Upper plot (original method) has a significant proportion of these events labelled as background definite (log likelihood ¿ 3). Final method has very small proportion of events labelled as background definite.*

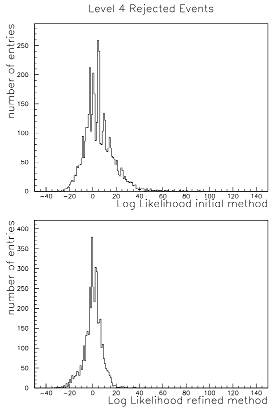


Figure 7.8: *Log likelihood distributions of the L4reject sample. The upper plot shows results calculated using the initial method. The lower plot shows the log likelihood calculated by the refined equal assumption method. The proportion of events labelled as background definite reduces from 54% to 34%. There is no separation into background and interaction peaks.*

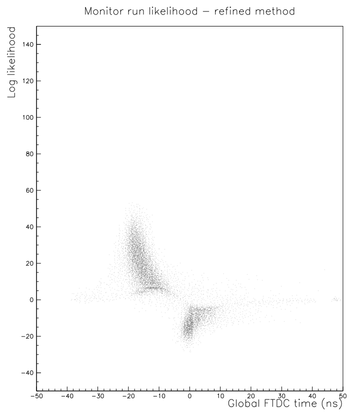


Figure 7.9: *Log likelihood of events against ToF global FTDC time as calculated by the refined equal assumption method. The data was taken from the monitor run. The upper left hand part of the distribution is the background peak, the bottom right hand part the interaction peak (of Figure 7.6).*

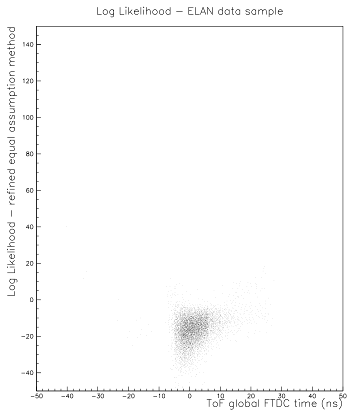


Figure 7.10: *Log likelihood vs global FTDC time of post-cut ELAN sample data using the refined equal probabilities method. Most of the events are interaction associated.*



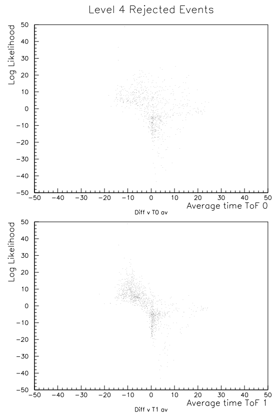


Figure 7.11: *Log likelihood distributions of the L4reject sample plotted against ToF 0 and ToF 1 average times. Similar to the global India plots these show clearly the early hits having positive likelihoods.*

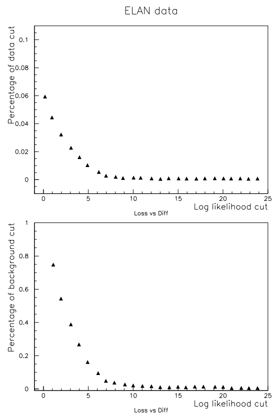


Figure 7.12: *Proportion of events removed from the ELAN data sample as a function of log likelihood. The top plot shows the total loss to the sample, the lower shows the proportion of events labelled as background removed as a function of log likelihood.*

# Chapter 8

# Forward ToF

## 8.1 The Forward time-of-Flight system (FToF)

ToF uses the time of particles passing through to distinguish background from interaction particles. The installation of a similar scintillator wall (called FToF) in the forward area allows a further separation of interaction from background. Initially, a test system was installed to find the effects of including a veto based on such a system.

FToF data can be combined with that from the ToF (or BToF - backwards time of flight) to give information on background contamination.

## 8.2 FToF hardware

The FToF is a pair of scintillators recently installed by QMW perpendicular to the beam axis between the forward muon toroid and the first forward muon $\phi$ layer ($z$=+7.0 m). Its purpose is to help identify background particles by their timing. The scintillators measure 200 $\times 600 \times 10$ mm$^3$ and are separated by 7.5mm of lead. FToF lies 50 mm from the beam axis and primarily detects secondary scattering from the proton remnant, beam gas, beam wall or an $ep$ collision.

Signals from such particles are read out by 2 standard EMI 9839B photomultiplier tubes shielded by soft iron and mu-metal cans. The data is strobed into 3 windows (similar to BToF), interaction, background and global. The interaction window covers the time when proton beam associated particles pass through FToF, $\pm 10$ ns from the peak of the proton timing distribution. The background window covers the time from +10 ns after the proton peak to the start of the electron peak (35 ns wide). The global window covers the electron peak and the proton peak.



Coincidences between the counters in each of these windows are used to form signals which are sent to the central trigger logic (CTL) as trigger elements. The global signal is also sent to an FTDC (located in the central tracker electronics) for offline determination of timing. The data is located in channel 23 of the CRPE bank, replacing the BToF ToF1 BG trigger element FTDC time which was there previously (See Appendix C.1.11). The time of this signal is reconstructed at level 4 and available for use in any level 4 trigger.

## 8.3 FToF Trigger Data

### 8.3.1 Trigger elements and subtriggers

Table 8.1 shows the FToF trigger elements and subtriggers, the veto chosen was FTOF BG and $\overline{FTOF\ IA}$ (subtrigger 103) and was not implemented until run 78674 (See section 8.8).

| Trigger name | Trigger element | Subtrigger |
|---|---|---|
| Interaction | 69 | 101 |
| Background | 70 | 102 |
| Global | 71 | |
| $\overline{FToFIA}$ & FToF BG | | 103 |
| ToF GL & FToF GL | | 47 |

Table 8.1: FToF trigger elements and subtriggers

### 8.3.2 Proportion of data affected

The proportion of data which contained an FToF trigger element/subtrigger was measured and is shown in Table 8.2.

As can be seen, the total amount of data with both ToF and FToF triggers is small, however there is a significant number of FToF background events present.

## 8.4 FToF online data

Figure 8.1 shows the timing distribution of the FToF global trigger during a run when only protons were in the HERA beam. Satellite bunches can be clearly seen. Beam conditions vary, but satellite bunches are present in every run at some level.

| Trigger | Proportion of data |
|---|---|
| Any FToF information | 10-35% |
| FToF IA trigger element | 10 - 30% |
| FToF BG trigger element | 5 - 15% |
| FToF GL trigger element | 10 - 35% |
| $\overline{FToFIA}$ & FToF BG | 5 - 10% |
| FToF GL and ToF GL | 4 - 6% |

Table 8.2: FToF trigger elements and subtriggers

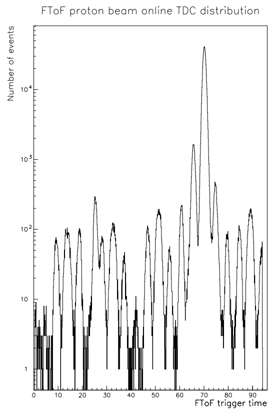


Figure 8.1: *Online timing distribution of FToF events with only proton beam present in the HERA machine. Highest peak is the main proton bunch, the outlying peaks are the satellite bunches. Note the Log scale on the Y axis.*



## 8.5 FToF FTDC data

FToF FTDC data was reconstructed using the algorithm developed for BToF FTDC data (See Chapter 6). This method gives a resolution of ±1ns. FTDC times were reconstructed for preliminary physics data from an ELAN sample of ~ 9000 events. The data quality was further improved by using low-$Q^2$ physics cuts developed by the HADES group. The loss caused by vetoing all events after a certain time was calculated.

The ELAN data sets used were:
H1KADR.H1LOWQ2.MDST01 to
H1KADR.H1LOWQ2.MDST06 inclusive.
The cuts applied were:

- Non-zero Z vertex.
- Z-Vertex within +25 cm or −35 cm of 0.
- Electron Energy >10.6GeV.
- Electron between $160^{\circ} \leq \theta \leq 172^{\circ}$.
- BEMC cluster radius less than 4cm.
- BEMC cluster centre-of-gravity more than 13cm from beam line.

## 8.6 Comparison with BToF timing

In the proposal for FToF [22], it was noted that the difference in timing between the signals in the two subdetectors would be a good way to detect and so veto background which BToF is unable to veto.

Background particles should arrive in FToF about 27 ns after those in BToF. Interaction particles should arrive in FToF about 8 ns after those in BToF. The signal arrival times and differences are summarized in Table 8.3.

| Particle | Time in FToF | Time in BToF | Difference FToF − BToF |
|---|---|---|---|
| Interaction | $t0 + i$ | $t0 + j$ | $i - j$ (~ 8 ns) |
| P Background | $t0 + i$ | $t0 - p$ | $i + p$ (~ 27 ns) |

Table 8.3: FToF and BToF relative timing

$t0$ is the event interaction time.

The flight time of a particle from the interaction point to FToF is $i$.

The flight time of a particle from BToF to the interaction point is $p$.

## 8.7 FTDC results

The numbers of events with FToF and BToF information are given in Table 8.4.

### 8.7.1 FToF alone

The FToF FTDC distribution for the whole sample is shown in Figure 8.2. The distribution of the cut data is shaded. The tail of the distribution is sharply reduced after the cuts. Note the arbitrary zero for the FToF FTDC distribution.

Only ~35% of physics events have an FToF trigger, which is low compared with the expected results from simulation of FToF [21]. There are several possible reasons for this:

- There is a class of diffractive events which have no proton remnant which escapes from the beampipe. These events would cause no hits in FToF.
- The simulation of the beampipe has been much improved since the FToF study, and the previously incomplete simulation could account for the lower FToF trigger rate.
- The Monte Carlo generators themselves differed by up to 20% indicating an incomplete understanding of the remnant jet.

This is true for both the pre-cut and post-cut sample.

### 8.7.2 Comparison of FToF and BToF data

Most low-$Q^2$ physics events, such as those in the ELAN sample, have BToF FTDC information of some sort. Approximately 80% have a BToF global trigger, and ~30% have both a BToF global and FToF trigger.

The flight time difference between them can be seen in Figures 8.3, 8.4, and 8.5.

In figure 8.3 the distribution forms two peaks. The left hand peak is made up of those events where particles from the interaction point strike both BToF and FToF. The right hand peak is composed of events from particles associated with the proton



beam which passed through BToF first and FToF later. These particles hit BToF in the BToF interaction window and so were not vetoed. Most of these events have been removed by the HADES cuts, while more of the left-hand peak survives these.

Figure 8.4 shows FToF plotted against BToF global trigger time. Here the separation into 'interaction' events and remaining (unvetoed) 'proton background' events can be seen. The background events lie in the line of events running from bottom left to top right. The interaction events are clustered around the centre of the plot. As with Figure 8.3, most background events do not survive the physics cuts. Any events with a BToF time between $-35$ ns and $-10$ ns were removed by the BToF background veto at level 1. The small cluster of events in the bottom left hand corner are from proton satellite bunches.

Figure 8.5 shows FToF minus BToF plotted against FToF trigger time. Again, the separation into interaction and background can be seen. The background events lie in a horizontal line above the interaction events. The physics cuts remove most of the background events.

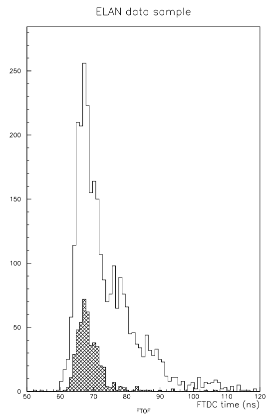


Figure 8.2: *FTDC distribution of FToF events, with an arbitrary zero. Shaded area are those events surviving the physics cuts.*

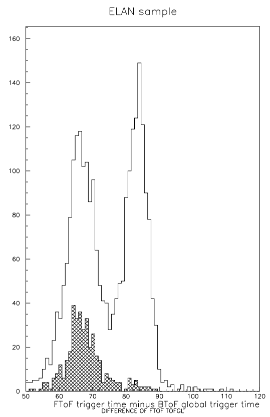


Figure 8.3: *Difference between BToF global trigger time and FToF trigger time. The shaded events are those which pass the physics cuts.*



| Quantity | Before cuts | % | After cuts | % |
|---|---|---|---|---|
| Total number of Events | 8832 | 100 | 1314 | 100 |
| Events without BToF GL or FToF | 1140 | 12.9 | 181 | 13.8 |
| Events with FToF | 2925 | 33.1 | 475 | 36.1 |
| Events with FToF and no BToF GL | 426 | 4.8 | 90 | 6.8 |
| Events with BToF GL | 7227 | 81.8 | 1043 | 79.4 |
| Events with BToF GL and no FToF | 4707 | 54.3 | 658 | 50.1 |
| Events with FToF and BToF GL | 2504 | 28.4 | 385 | 29.3 |

Table 8.4: ELAN dataset BToF and FToF information.

## 8.8 FToF and BToF timing cuts

After these initial studies were performed an FToF veto signal has been included as a trigger element at level 1 from run 77950, included in events with an FToF time between 10 ns after the proton peak and the start of the FToF electron strobe (i.e. from 77-112 ns on the plots in this paper). It was not used as a veto until run 78674. Between these two runs, studies to determine any subtrigger bias were made. See Section 8.10.1 for the effects of this setting on the physics sample.

The veto signal is formed from a combination of FToF background (FToFBG) and *not* FToF interaction ($\overline{FToFIA}$).This was to ensure that events with a hit in both the FToF interaction and FToF background window were not vetoed.

A further cut can be made using the difference between FToF and BToF global trigger time, available at level 4 at present. Background particles passing through both ToF and FToF have a different time distribution to those from real interactions.

The effect of the FToF cut can be seen in Figure 8.7, showing the right hand (background) peak of the FToF−BToF difference much reduced. The remaining background events can be removed by placing a veto on events with a FToF−BToF time difference of greater than (say) 75 ns. This would maximise the background rejection while minimizing the loss to physics events.

This data is available at level 4 and so could be included as a trigger. There is currently work being performed at Manchester University into the possibility of

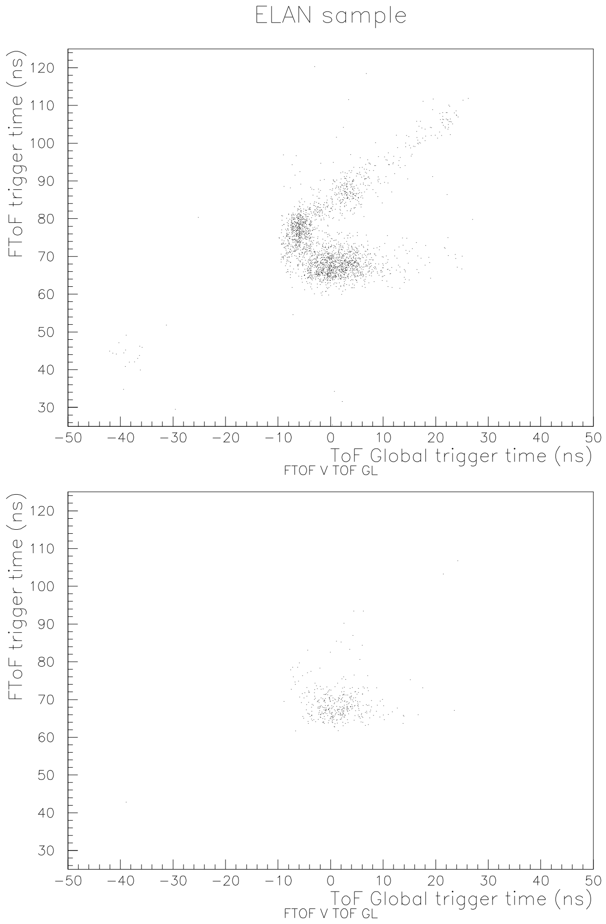


Figure 8.4: *FToF trigger time against BToF global trigger time. The straight line distribution running bottom left to top right in the upper plot is caused by proton associated hits, probably satellite bunches. It is missing in the lower plot which is the physics sample. Arbitrary zero on the y axis.*



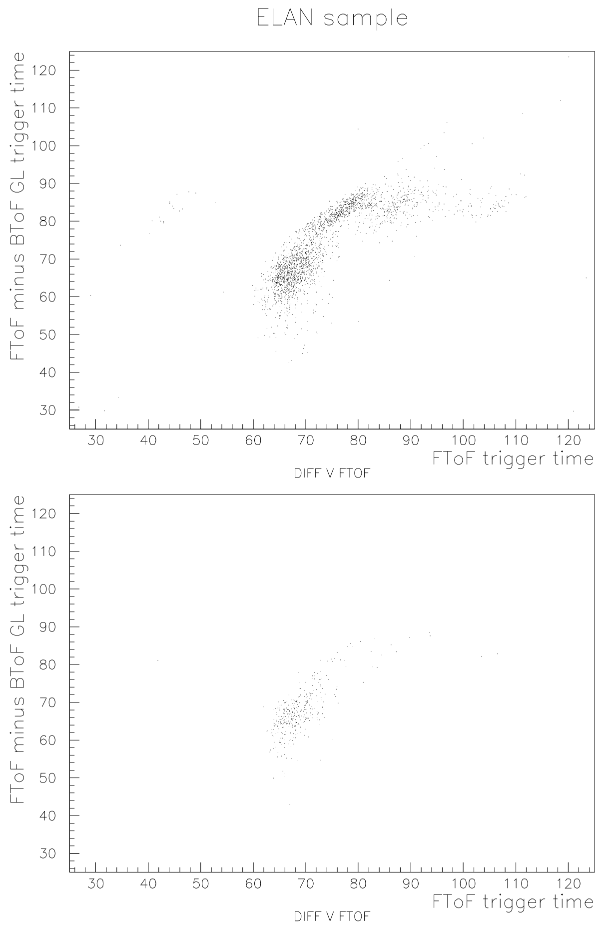


Figure 8.5: *FToF minus BToF against FToF trigger time. The upper plot shows all events, the lower plot shows those surviving the cuts. Arbitrary zero on both axes.*

hardware to allow this cut to be made at level 1.

## 8.9 Definition of background events

Background events are caused mostly by particles travelling with the proton beam. There are several indicators to this, including event size, BToF and FToF timing, and vertex quality. Figure 8.6 shows the events size and vertex quality against the FToF-BToF time of an event. Vertex quality is the number of tracks used to make the vertex, the higher the number, the higher the quality of the vertex. Background triggers with a large event size are best vetoed at level 1. This minimizes the deadtime of the apparatus.

The events fall into two distributions, the left hand one has better physics characteristics (better vertex quality), the right-hand one more background characteristics (larger event size).

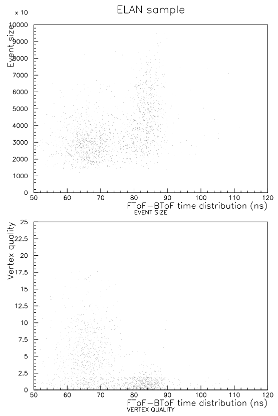


Figure 8.6: *Other signs of background in the FToF-BToF data. Events in the right hand distributions have more background characteristics.*



Offline physics cuts also select events in a more rigorous way, but may still include background events. Therefore, both the offline physics cuts and other indicators have been used in the estimate of losses to physics events.

Figure 8.7 shows that several events which *pass* the HADES physics cuts have timing consistent with being background events. Assuming that the FToF−BToF timing difference is efficient at separating background particles from interaction particles, an independent measure of the number of background and non-background particles can be calculated by fitting curves to the full FToF−BToF timing sample.

Two gaussian distributions were fitted to the FToF−BToF distribution. Those which fell into the left hand distribution were considered as 'interaction' events, those in the right hand distribution as background events. Figure 8.8 shows the fits to the full FToF sample (no FToF veto).

The loss to 'interaction' data from imposing a FToF−BToF cut can then be calculated and these results can be compared with the loss to physics events (as defined by offline cuts) to give an alternative measure of the effect of an FToF−BToF veto.

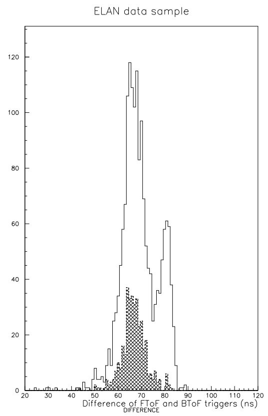


Figure 8.7: *Difference of FToF and BToF trigger times after the FToF veto has been applied. The shaded events represent those that survive the HADES physics cuts.*

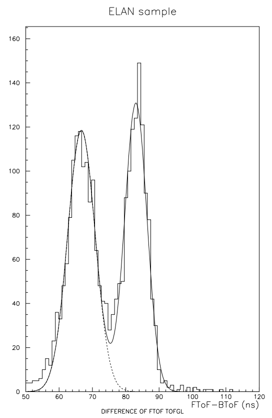


Figure 8.8: *Gaussian fits to FToF-BToF data.*



## 8.10 Effects of FToF cuts on the ELAN dataset

### 8.10.1 FToF only

The reduction of the dataset, before and after cuts, can be calculated as a function of the veto strobe position. Figure 8.9 shows the effect on the FToF events, which make up about 30% of the total data sample (see Table 8.4).

The setting of the FToF strobe at about 77 ns results in:

Physics loss from FToF events 7%

Physics loss from all events 2%

Total reduction of FToF events 42%.

Total reduction of data set 13%.

The loss to the post-cut physics data is the important quantity. The loss to the full dataset does not necessarily show the proportion of all events taken at level 1 (or even level 4) as the data is a preselected *physics* sample. Further analysis on raw and L 4reject data is being performed to calculate this quantity on a more basic sample.

### 8.10.2 FToF and BToF coincidence

The effect of the setting of an FToF−BToF trigger is shown in Figure 8.10. As with the veto on FToF alone, there is a significant reduction of background for a small loss in physics events.

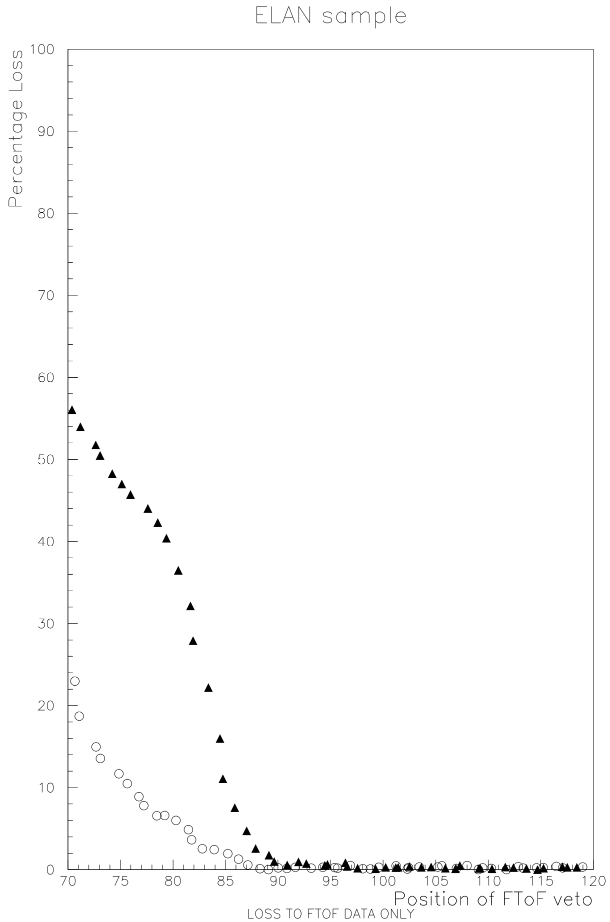


Figure 8.9: *Effect of the position of an FToF veto on the ELAN data sample. Triangles show the effect on all FToF events, circles show the effect on FToF events passing physics cuts. FToF events make up approximately 30% of the total dataset.*



## 8.11 Conclusion

Both the FToF cut and the FToF−BToF cut can remove background. Further work is continuing on the effect of FToF on the level 1 trigger.

The loss to physics data depends on the setting of the FToF strobe, but is small compared to the amount of background vetoed. With the strobe set as it is now, the total loss to physics is 2%. Further studies on the data sample show that some of the events which pass the HADES cuts seem, in fact, to be background, and so the calculated loss is an upper limit on the physics loss.

An independent analysis by R. Maracek on FToF trigger elements agrees with these figures. He finds a 3.5% loss to events passing physics cuts, and 9% reduction in the dataset. Scanning the 'physics' events which were cut by the FToF veto showed that almost all were, in fact, background events.

The FToF−BToF cut is useful in removing further background events over and above those cut by the FToF veto. Currently this cut would be achieved at level 4, but a hardware solution would allow a level 1 trigger element to be created. An initial setting (for test purposes) of any level 4 FToF−BToF cut should be $\sim 78$ ns (as defined by the plots in this paper).

The additional loss to physics is small, and the proportion of data removed needs to be studied using raw and level 4 rejected events. The physics sample is preselected and data-reduction calculations cannot be safely based on this.

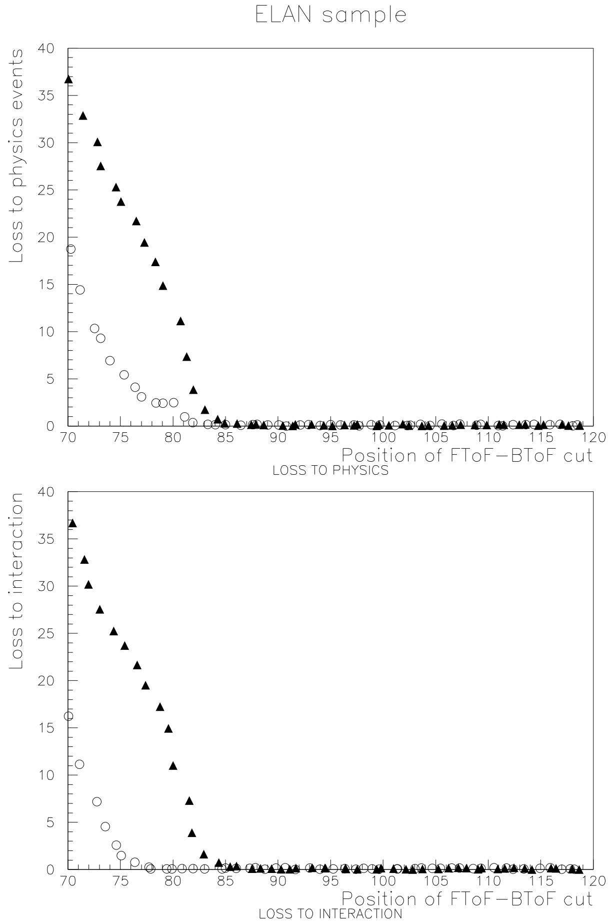


Figure 8.10: *Effect of the position of an FToF-BToF veto on the ELAN data sample after the proposed FToF veto has been applied. Triangles show the effect on all FToF-BToF events, circles show the effect on FToF-BToF events classed as physics. The upper plot has physics events defined by HADES cuts, the lower plot has physics events defined as being in the interaction peak of the FToF-BToF timing distribution.*



# Chapter 9

# Conclusion

ToF was required to enable the H1 level 1 trigger to veto the large numbers of background events expected from the proton beam. ToF vetoed 99% of triggers, and therefore the proportion of real physics removed by the ToF veto was a vital number to find out.

The initial testing of ToF components and description of their operating characteristics is given in Chapter 4.

After installation in H1, and the photomultipliers were successfully plateaued, analysis of the ToF readout for the 1992 run allowed fine tuning of the ToF logic and revealed the need for TDC data to improve background resolution.

The software for offline monitoring of ToF was developed along with the code to reconstruct the ToF FTDC information. Analysis of the trigger and timing data from ToF, once successfully reconstructed, was achieved. Timing distributions were found and compared with online distributions, to show that the offline data was of good quality. This made further work possible, and the timing data was analysed to provide the calculation of losses to physics data sets: $\sim$2.5% for the 1992 run, falling to less than 1.0% for the 1993 and 1994 runs. The peak separation discrepancy of 3 ns was shown to come from backscattered events and the hit-multiplicity timing dependence of events in ToF.

The timing information from individual ToF counters was combined using a log likelihood method and a further separation of background was possible offline. This last method also allowed a measure of background contamination to be estimated. Analysis of the FTDC data allowed a measurement of the inefficiencies of ToF. Only 0.5% to 1.0% of the physics events accepted by the experiment were background which ToF did not veto.

The Forward Time-of-Flight (FToF), a simple but similar device placed on the opposite side of the experiment, was installed, and a further level of background rejection was available at level one. Studies were made of FToF trigger data using software cuts to determine its effect on the physics sample, and the effect of combining the ToF and FToF trigger timing on proton background rejection was studied.



# Appendix A

## A.1 Glossary of terms

### A.1.1 Abbreviations

ADC Analog to Digital Converter

BEMC Backward Electromagnetic Calorimeter - one of the subdetectors on H1.

bc or BC Bunch crossing

BPC Backward proportional chamber - one of the subdetectors on H1.

BToF Backward Time of flight counter - one of the subdetectors on H1, and the subject of this thesis.

Bunch crossing. 96 ns i.e. the separation of bunches when the accelerator is filled with 210 bunches.

Barn (also mB and $\mu$B). A measurement of cross section. Usually expressed as a luminosity ($\mu B^{-1}$.

CAMAC Not an acronym. A hardware system for computer control of analog and digital input and output.

CIP Central Inner Proportional chamber - one of the subdetectors on H1, part of the central tracker.

CIZ Central Inner Z-chamber - one of the subdetectors on H1, part of the central tracker.

CJC Central Jet Chamber - one of the subdetectors on H1, part of the central tracker.

COP Central Outer Proportional chamber - one of the subdetectors on H1, part of the central tracker

COZ Central Outer Z-chamber - one of the subdetectors on H1, part of the central tracker

CTD Central Tracking Detector - one of the subdetectors on H1.

DCA Distance of Closest Approach

DIS Deep Inelastic Scattering. A strong interaction process where the quarks inside the proton can be discerned.

FADC Flash Analog to Digital Converter, a hardware device for measuring accumulated charge.

FEC Forward end cap. Part of the forward muon system.

FTD Forward Tracking Detector - one of the subdetectors on H1.

FTDC Flash Time to Digital Converter - Converts analog input signal to a digitised time.

FToF Forward time of flight - a recently installed subdetector on H1.

FWPC Forward proportional chambers - one of the subdetectors on H1.

LAr Liquid ARgon calorimeter - one of the subdetectors on H1.

L1 Level 1 trigger.

MWPC Multiwire proportional chambers - one of the subdetectors on H1.

NIM Nuclear Instruments Module.

PM or pm Photomultiplier tube.

Radiation Length ($X_0$) - Average distance an electromagnetic particle will travel inside a material before undergoing an interaction.

$T0$ the measured time of an event.

TDC Time to Digital Converter.

ToF Time-of-Flight (The Time-of-Flight device for H1) - one of the subdetectors on H1, and the subject of this thesis.

$z$ Distance along the beam line. Positive $z$ is in the forward direction.

## A.2 Physics Quantities

The description of the physics which interests scientists at HERA uses many terms and abbreviations for various quantities.

$Q^2$ Square of the (negative) four momentum transfer in DIS

$s$ square of the centre of mass energy of the collision

$x$ the fraction of the proton's energy carried by the struck parton also Bjorken scaling variable.

$y$ fraction of (maximum) energy transfer



## A.3 Useful Quantities

$$s = (e + p)^2 = 4E_e E_p \tag{A.1}$$

$$q^2 = (e - e')^2 = -2E_e E'_e(1 + cos\theta_{e'}) = -Q^2 \tag{A.2}$$

$$x = Q^2/(2q.p) = Q^2/(2m_p\nu) = Q^2/(ys) \tag{A.3}$$

$$y_e = 1 - (E_{e'}/E_e)(1 - cos\theta_{e'})/2 \tag{A.4}$$

$$\nu = q.p/m_p \tag{A.5}$$

$$\nu_{max} = s(2m_p) \tag{A.6}$$

### A.3.1 Technical terms

Bunch crossing, 96 ns = 1/220th of the time it takes 1 bunch to orbit HERA once. when all 220 bunches are in the machine, each is 96ns from its neighbour.

Crate. A rack which provides power to electronic units placed within it. Certain systems also provide command signals to each box within the crate.

NIM unit. A box containing electronic logic. Incoming signals are processed and other signals are outputted.

Strobe. A (short) period of time defined relative to each bunch crossing and produced in electronic logic.

# Appendix B

## B.1 Triggers at H1

The actual subtriggers used to take data changed continually from run to run, as more was learned about the system, and according to beam conditions. Table B.1 gives the classes of triggers available to H1. Full details are available in [23]

| Trigger number | Description | Trigger number | Description |
|---|---|---|---|
| 0 to 11 | BEMC triggers | 80 to 95 | etag triggers |
| 14 to 30 | Muon triggers | 96 to 98 | ToF triggers |
| 32 to 42 | Vertex triggers | 99 to 117 | Monitor triggers |
| 64 to 68 | LAr Triggers | 120 | Pilot bunch trigger |
| 72 to 77 | LAr Triggers | 124-127 | empty bunch triggers |

Table B.1: *Subtriggers used in the H1 central trigger*



# Appendix C

## C.1 ToF information

### C.1.1 Trigger Elements

The location of the ToF trigger elements in the TEL1 bank are:

| ToF trigger element | All Runs |
|---|---|
| ToF Interaction | 64 |
| ToF Background | 65 |
| ToF Global | 66 |
| ToF1 Background OR | 67 |
| ToF1 BG1 | 68 |
| ToF1 Global OR | 71 |

### C.1.2 Subtriggers

The following subtriggers had a ToF trigger element present.

### C.1.3 Trigger changes

There were eight channels provided for ToF input into the level1 trigger. Later use of three more channels was provided for extra input. The three most important trigger elements were background, interaction and global and were always provided to CTL. The other channels provided various signals as defined below:

A definition of each trigger element is given below, each signal has a length of one bunch crossing except the ToF BG trigger.

- ToF IA - coincidence of the OR of each wall in the IA strobe.
- ToF BG - coincidence of the OR of each wall in the BG strobe used for vetoing and of run-dependent length.

| Subtrigger Name | Number | From Run | Until Run |
|---|---|---|---|
| ToF Background | 33 | 21000 | 35175 |
| ToF Background | 88 | 35176 | 36206 |
| ToF Background | 97 | 50673 | end of 94 |
| ToF Interaction | 32 | 21000 | 35175 |
| ToF Interaction | 89 | 35176 | 36206 |
| ToF Interaction | 96 | 50673 | end of 94 |
| ToF Global | 98 | 50673 | end of 94 |
| ToF IA & ZVTX-sig1 | 83 | 21000 | 35175 |
| ToF IA & ZVTX-sig1 | 90 | 35176 | 36206 |
| ToF GL & Veto Inner GL | 29 | 21000 | 35175 |
| ToF GL & Veto Inner GL | 91 | 35176 | 36206 |
| eTAG & ToF IA | 1 | 21000 | 35175 |
| eTAG & ToF IA | 81 | 35176 | 61332 |
| eTAG & ToF IA & LAr IF>0 | 81 | 61333 | end of 94 |
| eTAG & ToF IA & LAr EPlug>0 | 85 | 62575 | end of 94 |
| BPC & CIP2 & ToF IA | 56 | 35176 | 36206 |
| ToF 1 & CIP2 | 23 | 21000 | 35175 |
| ToF 1 & CIP2 | 53 | 35176 | 36206 |
| BPC & ToF 1 | 24 | 21000 | 35175 |
| BPC & ToF 1 | 52 | 35176 | 36206 |
| DC-RPHI-THR-0 & ToF IA | 44 | 35176 | 36206 |
| BSET-Etot & ToF IA | 4 | 21000 | 35175 |
| BSET-Etot & ToF IA | 2 | 35176 | 36206 |
| BSET-CL1 & ToF IA | 12 | 35176 | 36206 |
| BSET-CL3 & ToF BG | 9 | 50673 | 52235 |
| BSET-CL3 & BSET EQ1 & ToF BG & BEMC LONG CLUS < 31 | 9 | 52236 | end of 93 |
| ToF 1 BG OR | 103 | 50673 | end of 93 |
| ToF 1 any IA & ToF 1 bg lt IA | 102 | 50673 | end of 93 |
| Mu FEC & ToF BG | 31 | 56620 | end of 93 |
| ToF1 BG GT IA | 101 | 56620 | end of 93 |

Table C.1: *ToF subtriggers*



| Name of trigger | Runs valid for | trigger element |
|---|---|---|
| ToF IA | up to 25695 | C0 |
| ToF BG | up to 25695 | C1 |
| ToF GL | up to 25695 | C2 |
| ToF1 GL OR | up to 25695 | C7 |
| ToF IA | 25695 - 66609 | 64 |
| ToF BG | 25695 - 66609 | 65 |
| ToF GL | 25695 - 66609 | 66 |
| ToF1 GL OR | 25695 - 66609 | 71 |
| ToF1 BG OR | 28483 - 66609 | 67 |
| ToF BG1 | 28483 - 66609 | 68 |
| ToF1 any IA | 50673 - 66609 | 53 |
| ToF1 BG LE IA | 50673 - 62574 | 54 |
| ToF1 no BG | 50673 - 62574 | 55 |
| ToF1 BG M1P1 | 50673 - 66609 | 69 |
| ToF1 BG GT IA | 62574 - 66609 | 54 |
| ToF1 BG | 62574 - 66609 | 55 |

Table C.2: *Changes to ToF trigger elements*

- ToF GL - coincidence of the OR of each wall in the GL strobe.
- ToF1 GL OR - OR of all the counters in ToF1 within the GL strobe.
- ToF1 BG OR - OR of all the counters in ToF1 within the BG strobe.
- ToF1 BG1 - as ToF BG but only 1 bunch crossing long.
- ToF1 any IA - OR of all the counters in ToF1 within the IA strobe.
- ToF1 BG LE IA - Only provide a signal if the sum of ToF1 counters with hits within BG window is less than sum of ToF1 counters in IA window.
- ToF1 no BG - Logical Negative of ToF1 BG OR signal.
- ToF1 BG M1 P1 - One and only one hit in ToF1 in BG window.
- ToF1 BG GT IA - Logical Negative of ToF1 BG LE IA

Certain ToF trigger elements were used in different vetoing levels, applied to certain triggers in the 1993 run. The vetoing conditions and the subtriggers they affected are given in table C.3 below.

| Veto condition | Subtriggers affected |
|---|---|
| No ToF BG trigger | 0,4,6,7,8,11,22,23 |
| No ToF BG trigger | 28,38,39,40,64-68,72,73 |
| No ToF BG trigger | 75-77,80-85,87-89,64-68 |
| No ToF BG trigger | 91-92,116,120 |
| No Tof BG & no CIP backward | 14,16-19,24-27,29 |
| No Tof BG & no CIP backward | 32-37,41-42 |
| No ToF BG & ToF 1 BG $\leq$ IA | 2,3 |
| No ToF BG & ToF 1 any IA & ToF 1 BG $\leq$ IA | 1,5 |
| No ToF 1 BG OR | 125 |

Table C.3: Different vetoing schemes

### C.1.4 ToF trigger signal length

The length of the ToF BG trigger signal sent to the L1 trigger was changed to allow out of time triggers from other subdetectors to be vetoed.

The length of the BG trigger signal was as follows:

| Run numbers | Number and relative position of bunch crossings vetoed |
|---|---|
| Up to 32992 | 3 NmBC NmBC-1 NmBC+1 |
| 32993-33092 | 1 NmBC-1 * |
| 33093-33241 | 3 NmBC NmBC-1 NmBC+1 |
| 33242-36226 | 2 NmBC NmBC+1 |
| 50673-66609 | 6 NmBC NmBC-1 NmBC+1 NmBC+2 NmBC+3 NmBC+4 |

* For runs 32993 to 33092 only the bunch crossing before the nominal one was vetoed. This was a mistake which was rapidly rectified.

$NmBC$ is the nominal bunch crossing (bc).

$NmBC - 1$ is one bunch crossing before the nominal bc.

$NmBC + n$ is $n$ bunch crossings after the nominal bc.

For the 1993 running 6 bunch crossings were vetoed each time a veto signal was sent to the CTL. This led to a deadtime of 0.35% which is negligible compared to other sources of deadtime.

### C.1.5 ToF photomultiplier numbers

### C.1.6 Changes to ToF strobes

The position of the ToF trigger strobes greatly affects the efficiency of vetoing background and hence the deadtime of the experiment. During early running the strobes



| Location | Number | Location | Number |
|---|---|---|---|
| ToF 000 | AM 988 | ToF 104 | AM 612 |
| ToF 001 | AM 996 | ToF 105 | AM 614 |
| ToF 002 | AM 1003 | ToF 106 | AM 615 |
| ToF 003 | AM 1004 | ToF 107 | AM 616 |
| ToF 004 | AM 1005 | ToF 108 | AM 617 |
| ToF 005 | AM 1009 | ToF 109 | AM 618 |
| ToF 006 | AM 1017 | ToF 110 | AM 626 |
| ToF 007 | AM 1018 | ToF 111 | AM 628 |
| ToF 100 | AM 598 | ToF 112 | AM 630 |
| ToF 101 | AM 601 | ToF 113 | AM 631 |
| ToF 102 | AM 603 | ToF 114 | AM 635 |
| ToF 103 | AM 605 | ToF 115 | AM 636 |
| Spare | AM 613 | Spare | AM 633 |

Table C.4: *ToF photomultiplier ID numbers*

had yet to be optimized, and were changed several times for reasons explained below.

During early running the interaction (IA) strobe was set a few ns after the background (BG) strobe. The width was small (6-8ns) initially, but once it became clear that the ToF interaction trigger element was present in a large fraction of low-$Q^2$ data, the IA strobe was widened. Information from the FTDCs showed that the low-$Q^2$ data struck ToF (especially ToF1) earlier than the vast majority of ToF interaction triggers. The IA strobe was brought closer to the end of the BG strobe for this reason.

The BG strobe itself was initially set wide to catch very early background events. It was later decided that only the time region of the proton beam's passage through ToF should be vetoed.

The start time of each strobe is given relative to the start time of the global strobe. The widths all three strobes: background (BG), interaction (IA) and global (GL) strobes.

| Date of change or run number | BG start | BG width | IA start | IA width | Global width |
|---|---|---|---|---|---|
| 22/05/92 | 7.3 | 8.6 | 32.4 | 18.0 | 93.0 |
| 25/05/92 | 11.8 | 8.6 | 25.4 | 15.0 | 93.0 |
| 26/05/92 | 11.8 | 8.6 | 25.4 | 6.0 * | 93.0 |
| 28/05/92 | 20.0 | 19.6 | 39.0 | 6.0 * | 93.0 |
| 01/06/92 | 20.0 | 17.0 | 39.0 | 6.0 * | 93.0 |
| 05/06/92 | 0. | 37.0 | 39.0 | 6.0 * | 93.0 |
| 29/06/92 | 0. | 37.0 | 39.0 | 6.0 * | 93.0 |
| 11/07/92 | 0. | 37.0 | 38-39.0 | 6.0 * | 93.0 ** |
| 09/09/92 | 0. | 36.2 | 38-39.0 | 6.0 * | 93.0 |
| 23/09/92 | 0. | 36.2 | 38-39.0 | 8.6 | 93.0 |
| 01/10/92 | 0. | 36.2 | 38-39.0 | 10.0 | 93.0 |
| 02/10/92 | 13.7 | 35.0 | 51.7-53.0 | 10.0 | 92.4 *** |
| 07/10/92 | 13.7 | 35.0 | 50.2-51.5 | 11.5 | 92.4 |
| 08/10/92 | 13.7 | 35.0 | 48.7-50.0 | 11.5 | 92.4 |
| 09/10/92 | 23.7 | 25.0 | 48.7-50.0 | 11.5 | 90.0 |
| 11/10/92 | 22.7 | 25.0 | 48.7-50.0 | 11.5 | 90.0 |
| 13/10/92 | 21.2 | 25.0 | 46.7 | 11.5 | 90.0 |
| 21/10/92 | 21.2 | 24.0 | 46.7 | 11.5 | 90.0 |
| 39550 | 18.2-20.2 | 24.0 | 43.7-45.7 | 17.0-19.0 | 90.0**** |

* Strobe was set to 8.6ns but overlap from logic gave only 6.0ns

** ToF1 IA set 1ns earlier than ToF0 IA

*** ToF1 IA set 1.3ns earlier than ToF0 IA

**** Major change. ToF1 BG strobe 3ns earlier (18.2) ToF1 IA strobe 3ns earlier (43.7) ToF0 BG strobe 1ns earlier (20.2) ToF0 IA strobe 1ns earlier (45.7) IA strobe width 17.0 ToF1 IA OR 19.0 width.

### C.1.7 BRTE bank

The BRTE bank is a BOS table [16] and contains ToF data for each channel in each of several bc's. The banks are numbered from 0 to 31, with 31 being the earliest beam crossing and 0 the latest. If any ToF data is present in a bc, then a BRTE bank with the number of that bc is present.

For runs up to 30000 all 32 bc's were read out and bunch crossing 21 and 22 contained the ToF counter data. For runs after 30000 10 bc's were read out, numbered 1 to 10. ToF counter data is usually in bc 7 with the trigger data being in bc 6.

The data is stored as follows:

Each 32 bit word contains the channel number and data for that channel. The first (most significant) 16 bits are the channel number and the second 16 (least significant) the data.



Channels are numbered as follows:

| Channel number | ToF data |
|---|---|
| 000 $\rightarrow$007 | ToF 0 counter 00 $\rightarrow$ 07 |
| 100 $\rightarrow$115 | ToF 1 counter 00 $\rightarrow$ 15 |
| 200 | ToF trigger data |

### C.1.8 Defining the bunch crossing of an event

In the code which analyses the BRTE data, the algorithm used is one which finds the earliest ToF data and ORs each counter with any data in the next bc. The trigger data from these and the bc following are OR'ed and this is labelled as the first data (see Section 5.7.1). This has been done because for early runs the ToF readout was not fully synchronized with the hera clock and data appeared in more than one bunch crossing. The trigger data appears up to one bunch crossing later because of hardware constraints in forming the trigger.

This process avoids contamination from reflections occurring 1 bc after the first hit of the event registered in ToF.

### C.1.9 HV settings

The main magnetic field of H1 causes pm tubes to operate at a reduced gain ($\sim$100 times lower). Therefore two standard HV settings were kept for each tube, one for running with the field (field-on) and one for running without the field (field-off).

These were constantly monitored and updated by plateauing using cosmic rays (See Chapter 4.5.2). The actual HV values are shown in Figures 4.5,4.4, and 4.6. Table C.5 shows the values used for the 1994 run.

### C.1.10 TDC parameters

TDC parameters were updated constantly. The later parameters were automatically included into the TOFREC reconstruction code. The earlier parameters are given below:

| ToF counter | Field off voltage | Field on voltage |
|---|---|---|
| 000 | 1429 | 2258 |
| 001 | 1370 | 2216 |
| 002 | 1399 | 2203 |
| 003 | 1427 | 2400 |
| 004 | 1416 | 2329 |
| 005 | 1533 | 2400 |
| 006 | 1482 | 2400 |
| 007 | 1472 | 2400 |
| 100 | 1237 | 1972 |
| 101 | 1368 | 2400 |
| 102 | 1236 | 2324 |
| 103 | 1480 | 2400 |
| 104 | 1303 | 2400 |
| 105 | 1244 | 2369 |
| 106 | 1250 | 1984 |
| 107 | 1308 | 2045 |
| 108 | 1326 | 2204 |
| 109 | 1257 | 2004 |
| 110 | 1220 | 1936 |
| 111 | 1440 | 2269 |
| 112 | 1170 | 1888 |
| 113 | 1348 | 2118 |
| 114 | 1292 | 2057 |
| 115 | 1310 | 2021 |

Table C.5: *ToF High Voltage settings for 1994 run.*

| FTDC channel | $\tau$ value | A value | Run range |
|---|---|---|---|
| Interaction | 17.0 | 206.5 | 31718-32645 |
| Background | 13.2 | 173.5 | 31718-32645 |
| Global | 14.1 | 181.0 | 31718-32645 |
| ToF 0 global OR | 12.4 | 280.0 | 31718-32645 |
| ToF 1 global OR | 15.0 | 318.0 | 31718-32645 |
| Interaction | 12.7 | 183.0 | 32646-36206 |
| Background | 13.4 | 169.5 | 32646-36206 |
| Global | 14.6 | 183.0 | 32646-36206 |
| ToF0 GL OR | 15.2 | 199.5 | 32646-36206 |
| ToF1 GL OR | 14.6 | 185.0 | 32646-36206 |



### C.1.11 Location of ToF FTDC channels

The TDC situation was continually changing before 32646. Several channels were not read out for many of the early runs, and some of those which were, did not work. Tables C.6 and C.7 show the available information. The offline data storage locations are shown in table C.8.

| Bank (raw) and channel (hex) | Bank (recon- -structed) | Data | Run range |
|---|---|---|---|
| CRZD F002 | CRTE | Global trigger time | up to 28718 |
| F02A | | ToF0 Global OR | |
| F02B | | ToF1 Global OR | |
| F000 | | electron pick up | |
| F001 | | proton pick up | |
| CRJD F007 | CRTD | Global trigger time | 28718-30000 |
| F02A | | ToF0 Global OR | |
| F02B | | ToF1 Global OR | |
| F000 | | electron pick up | |
| F001 | | proton pick up | |
| F010 | CRTD | Interaction trigger time | 30001-30450 |
| F011 | | Background trigger time | |
| F012 | | Global trigger time | |
| F013 | | ToF0 Global OR | |
| F014 | | ToF1 Global OR | |
| F018 to | | ToF0 Channel 0 to | |
| F01F | | ToF0 Channel 7 | |
| F020 to | | ToF1 Channel 1 to | |
| F02E | | ToF1 Channel 15 | |
| F02F | | ToF1 Channel 0 | |
| F000 | | electron pick up | |
| F001 | | proton pick up | |

Table C.6: *Location of ToF FTDC data*

* There was no FTDC information available between runs 31415 and 31716.

For period 92 - 4, the raw data bank (CRTD) was missing. The data for the first three periods was adequately reconstructed , but an unsuitable Qt algorithm led to unsatisfactory results for period five.

| Bank (raw) and channel (hex) | Bank (recon- -structed) | Data | Run range |
|---|---|---|---|
| CRZD F010 | CRTD | Interaction trigger | 30451-32012* |
| F011 | | Background trigger | |
| F012 | | Global trigger | |
| F013 | | ToF0 Global OR | |
| F014 | | ToF1 Global OR | |
| F018 to | | ToF0 Channel 0 to | |
| F01F | | ToF0 Channel 7 | |
| F020 to | | ToF1 Channel 0 to | |
| F02F | | ToF1 Channel 15 | |
| F000 | | electron pick up | |
| F001 | | proton pick up | |
| CRJD F010 | CRTD | Interaction trigger | 32021-32646 |
| F011 | | Background trigger | |
| F012 | | Global trigger time | |
| F013 | | ToF0 Global OR | |
| F014 | | ToF1 Global OR | |
| F018 to | | ToF0 Channel 0 to | |
| F01F | | ToF0 Channel 7 | |
| F020 to | | ToF1 Channel 0 to | |
| F02F | | ToF1 Channel 16 | |
| F000 | | electron pick up | |
| F001 | | proton pick up | |
| CRPD F010 | CRPE | Interaction trigger | 32646-36026 |
| F011 | | Background trigger | |
| F012 | | Global trigger | |
| F013 | | ToF 0 Global OR | |
| F014 | | ToF 1 Global OR | |
| F015 | | ToF 0 IA OR | |
| F016 | | ToF 1 BG OR | |
| F017 | | ToF 1 IA OR | |
| F018 to | | ToF0 Channel 0 to | |
| F01F | | ToF0 Channel 7 | |
| F020 to | | ToF1 Channel 0 to | |
| F02F | | ToF1 Channel 15 | |
| F000 | | electron pick up | |
| F001 | | proton pick up | |

Table C.7: *Location of ToF FTDC data*



| Run period | Run range | Raw Data | Reconstructed data |
|---|---|---|---|
| 92 - 0 | up to 28718 | CRZD | CRTE |
| 92 - 1 | 28718 to 30000 | CRJD | CRTD |
| 92 - 2 | 30000 to 30450 | CRZD | CRTD |
| 92 - 3 | 30451 to 31414 | CRZD | CRTD |
| 92 - 4 | 31414 to 31717 | None | None |
| 92 - 5 | 31718 to 32645 | CRZD | CRTD |
| 92 - 6 | 32646 to 39999 | CRPD | CRPE |
| 93 - 0 | 40000 to 49999 | CRPE | TOFT |
| 93 - 1 | 50000 to 52750 | CRPE | TOFT |
| 93 - 2 | 52751 to 54750 | CRPE | TOFT |
| 93 - 3 | 54751 to 57886 | CRPE | TOFT |
| 93 - 4 | 57887 to 59404 | CRPE | TOFT |
| 93 - 5 | 59405 to 59480 | CRPE | TOFT |
| 93 - 6 | 59481 to 60710 | CRPE | TOFT |
| 93 - 7 | 60711 to 61126 | CRPE | TOFT |
| 93 - 8 | 61127 to 61362 | CRPE | TOFT |
| 93 - 9 | 61363 to 61457 | CRPE | TOFT |
| 93 - 10 | 61457 to 61925 | CRPE | TOFT |
| 93 - 11 | 61926 to 69999 | CRPE | TOFT |
| 94 - 0 | 70000 to present | CRPE | TOFT |

Table C.8: Changes to the location ToF FADC offline data storage

# Appendix D

## D.1 Offline physics software cuts

Offline software cuts were developed by the ELAN and HADES groups to select DIS candidates from the DST event tapes. Several times I used these cuts to improve my data sample. The HADES cuts were:

| Cut | Minimum value | Maximum Value |
|---|---|---|
| Vertex | non 0 | non 0 |
| Energy of scattered electron | 10.6 GeV | none |
| Angle of scattered electron $\theta$ | $160^{o}$ | $172.5\ ^{o}$ |
| BPC hit from cog BEMC hit | none | 4 cm |
| Distance from centre of beampipe to hit in BEMC | 13cm | none |

Table D.1: *HADES cuts*

The ELAN cuts are detailed in [17]



# Bibliography


[1] Physical Review D particles and fields part 2 June 1992

[2] Fermilab-PUB-94 Evidence for Top Quark Production in $\overline{p}\,p$ collisions at $\sqrt{s} =$ 1.8 TeV *F. Abe et Al*

[3] Quarks and Leptons *F. Halzen & A. Martin*

[4] 1969 Callan-Gross relation Phys Rev Lett 22, 156 *Callan & Gross.*

[5] 1977 Nuclear Physics 126 297 *Altarelli G. and Parisi G.*

[6] Z Phys. C, 29 (1987) 561 *J. Kwiecinski.*

[7] 1987 DESY 87-140 *Ingleman and Ruckl*

[8] DESY-93-029, March 1993. Nuc.Phys.B396:3-26, 1993. A search for leptoquarks, leptogluons and excited leptons in H1 at HERA. *H1 collaboration*

[9] 1976 Soviet Journal of Nuclear Physics 23 338 *Lipatov L N*

[10] 1991 DESY-91-064 *Kim V. T. & Ryskin M. G.*

[11] Nuc Phys B439 1995. A measurement of the Proton structure function F2($x$,$Q^2$). *T. Ahmed et Al*

[12] DESY 93-103 *DESY Collaboration.*

[13] 1991 Physics Letters B269 p458 *Abramowicz et Al*

[14] Diploma Thesis: Pulshoehe und Zeitaufloesung der Szintillatorplatten fuer die inneren Waende des HERA H1-Detektors *Ch. Pichler*

*[15] Fpack event classification* H. Hufnagel

[16] *The BOS system. DESY internal report R1-88-01*V. Blobel

[17] *H1 note H1-04/93-284. ELAN miniDST selection used for DIS analysis of H1 1992 data* J.-F. Laporte.

[18] *Electricity and Magnetism 3rd Edition* Duffin

[19] *Private correspondence with P. Steffen.*

[20] *Forthcoming Thesis* T. Mavroidis

[21] *Forthcoming H1 note Some Results of Simulations of the Forward Time of Flight.* P. Biddulph

[22] *Proposal for a forward Time of Flight system.* G. Thompson, P.Biddulph and G. Lopez

[23] *H1TRIG H1 subtrigger information, from the DESY IBM.* U. Goerlach